Available online at www.sciencedirect.com

ScienceDirect

Geochimica et Cosmochimica Acta 320 (2022) 238–278

Geochimica et Cosmochimica Acta

www.elsevier.com/locate/gca

Early global mantle chemical and isotope heterogeneity revealed by the komatiite-basalt record: The Western Australia connection

I.S. Puchtel [a,*], R.W. Nicklas [a,1], J. Slagle [a,2], M. Horan [b], R.J. Walker [a], E.G. Nisbet [c], M. Locmelis [d]

[a] Department of Geology, University of Maryland, College Park, MD 20742, USA
[b] Earth and Planets Laboratory, Carnegie Institution for Science, Washington, D.C. 20015, USA
[c] Department of Earth Sciences, Royal Holloway, University of London, Egham TW20 0EX, UK
[d] Department of Geosciences and Geological and Petroleum Engineering, Missouri University of Science and Technology, Rolla, MO 65409, USA

Received 2 July 2021; accepted in revised form 26 November 2021; Available online 3 December 2021

Abstract

Although the heterogeneous nature of the chemical composition of Earth's mantle is now well established, the origin and longevity of the heterogeneities continue to be debated. In order to further study early-Earth heterogeneities, we present a set of Sm-Nd, Lu-Hf, Re-Os, and Hf-W isotope and lithophile and siderophile element abundance data for komatiites and basalts from the ~3.53 Ga Coonterunah, ~3.34 Ga Kelly, and ~3.18 Ga Ruth Well and Regal systems of the Pilbara Craton in Western Australia. The Sm-Nd, Lu-Hf, and Re-Os isotope data yield isochrons consistent with the accepted emplacement ages of the respective komatiite-basalt lavas. The mantle sources evolved with long-term $^{147}Sm/^{144}Nd = 0.200$ to 0.214 and $^{176}Lu/^{177}Hf = 0.0355$ to 0.0395, spanning the entire range of the time-integrated Sm/Nd and Lu/Hf measured in the Archean and Proterozoic komatiite-basalt systems to-date. Unlike with the other early Archean komatiites and basalts, the coupled ^{143}Nd-^{176}Hf isotope systematics of the Pilbara lavas provide no evidence for the involvement of early magma ocean processes in the evolution of their mantle sources. Episodes of variable degrees of partial mantle melting and melt extraction can account for the observed large variations in the time-integrated Sm/Nd and Lu/Hf ratios in the early Archean mantle domains.

In contrast to the highly variable Nd-Hf systematics, the initial $\gamma^{187}Os$ values vary within a narrow range from +0.9 to −0.4 indicating that the Pilbara mantle sources evolved with chondritic time-integrated Re/Os. The apparent discrepancy between the depletions in incompatible lithophile trace elements and near-chondritic Re/Os observed globally is reconciled via a model whereby early low-degree mantle melting events fractionated Sm from Nd and Lu from Hf, but had little effect on the Re/Os ratio. This in turn would imply early formation and long-term isolation of a basaltic crust highly enriched in incompatible lithophile trace elements.

The calculated total HSE abundances in the komatiite mantle sources range from ~30% in the Coonterunah to ~70% in the Regal system, of those in the estimates for the modern BSE, indicative of a 2.4× increase in HSE abundances from 3.53 to 3.18 Ga.

* Corresponding author.
E-mail address: ipuchtel@umd.edu (I.S. Puchtel).
[1] Scripps Institution of Oceanography, University of California San Diego, La Jolla, CA 92093, USA.
[2] Plexus Scientific, 5510 Cherokee Avenue, Alexandria, VA 22312, USA.

https://doi.org/10.1016/j.gca.2021.11.030

All four komatiite-basalt systems exhibit positive ^{182}W anomalies ranging between +11.4 and +7.7 ppm. The $^{182}W/^{184}W$ compositions and calculated HSE abundances in the Pilbara komatiite-basalt sources are inversely correlated and are most consistent with grainy late accretion of large differentiated planetesimals. Regression of the combined ^{182}W-HSE data for the komatiite systems allows an estimate of the W isotopic composition of the pre-late accretion BSE of +17 ± 7. This estimate is similar to that of the Moon of +25 ± 5 and lends further support to the notion regarding an initially common W isotopic composition in the Earth-Moon system.

Regression of the available HSE abundance data for komatiite mantle sources worldwide provides an estimate for the time of complete homogenization of late accreted materials within the mantle by 2.5 ± 0.2 Ga. Calculations indicate an average survival time of late accreted planetesimals in the Earth's mantle of 1.9 ± 0.2 Ga, which constrains the average mantle stirring rates for the HSE in the Hadean and Archean.

Keywords: Pilbara komatiites and basalts; Grainy late accretion; Sm-Nd; Lu-Hf; Re-Os; and Hf-W isotopic systematics; early mantle HSE abundances; Nd-Hf-Os paradox

1. INTRODUCTION

The chemically and isotopically heterogeneous nature of the terrestrial mantle has long been established as a result of numerous pioneering studies of the Earth's rock record (*e.g.,* Hart and Brooks, 1977; Zindler et al., 1982; Hofmann, 1984; Hart and Zindler, 1986; Zindler and Hart, 1986; Jacobsen, 1988; Galer and Goldstein, 1991). Some of the heterogeneities have been argued to be primordial, reflecting initial planetary accretion/differentiation and magma ocean crystallization processes (Goldstein and Galer, 1992; Albarède et al., 2000; Drake, 2000; Boyet and Carlson, 2005; Frost et al., 2008; Caro, 2011; Touboul et al., 2012; Carlson et al., 2015; Jacobsen and Yu, 2015; Puchtel et al., 2016a; Rizo et al., 2016; Boyet et al., 2021). Others were likely created as a result of a protracted terrestrial accretion history (e.g., Maier et al., 2009; Fiorentini et al., 2011; Willbold et al., 2011, 2015; Dale et al., 2017; Puchtel et al., 2018, 2020; Archer et al., 2019) or later processes associated with the dynamic regime of the planet, especially crustal recycling (*e.g.,* DePaolo, 1980; Armstrong, 1981; Hofmann and White, 1982; Patchett et al., 1984; Shirey and Hanson, 1986; Chase and Patchett, 1988; Galer et al., 1989; Bowring and Housh, 1995; Bennett et al., 1996; Salters and White, 1998).

Despite these long-term research efforts, limited insight into the terrestrial mantle mixing history implies that the nature, origin, scale, and longevity of early mantle heterogeneities in terms of different elements and isotopic systems remain contentious. This study is intended to fill some of the existing gaps in our understanding of these fundamental issues by applying a comprehensive set of state-of-the-art analytical tools to investigate a collection of early Archean samples of komatiites and basalts from the Pilbara Craton in Western Australia. This combination is especially advantageous to help elucidate the processes that occurred within the first 2 billion years of Earth's history.

2. GEOLOGICAL BACKGROUND AND SAMPLES

Rocks from Western Australia contain a record of very early events in Earth's history, such as 4.4 Ga old zircon from Jack Hills that imply the existence of mature continental crust in the Hadean (e.g., Wilde et al., 2001). This study focuses on komatiites and basalts from the Pilbara Craton in Western Australia (Fig. 1). The craton hosts abundant Archean komatiitic and basaltic lavas that represent a well-preserved ~500 Ma record of mantle-related magmatic activity (e.g., Nisbet and Chinner, 1981; Barley and Bickle, 1982; Arndt et al., 2001; Smithies et al., 2007; Nebel et al., 2014; Sossi et al., 2016).

The Pilbara Craton is composed largely of ovoid, multicomponent intrusive complexes of tonalite-trondhjemite-granodiorite (TTG) domes and surrounding steeply-dipping, keel-shaped volcanic-sedimentary sequences of cuspate greenstone belts of various ages. The craton is divided into the 3.53–3.17 Ga East Pilbara Terrane (EPT), the 3.27–3.11 Ga West Pilbara Superterrane (WPS), and the ≥3.18 Ga Kurrana Terrane (Smithies et al., 2007; Van Kranendonk et al., 2010).

The EPT is the ancient nucleus of the craton. It consists of the up to 20 km thick Pilbara Supergroup that is interpreted to have erupted on a >3.5 Ga proto-continental basement made of a heterogeneous mix of mafic and felsic lavas and TTG with a common tholeiitic parental magmatic source (Smithies et al., 2007). The Pilbara Supergroup includes four volcano-sedimentary groups (Fig. 2) deposited between 3.53 and 3.17 Ga (Van Kranendonk et al., 2006). The stratigraphically lowest Warrawoona Group is up to 12 km thick and is comprised mostly of basalts and komatiitic basalts with subordinate amounts of komatiites erupted in pulses during several ~15 Ma long volcanic cycles (Hickman and Van Kranendonk, 2012). The Warrawoona Group is subdivivded into four subgroups (from base to top): the 3.53–3.50 Ga Coonterunah subgroup, the 3.49–3.48 Ga Talga-Talga subgroup, the 3.47–3.46 Ga Coongan subgroup, and the 3.46–3.43 Ga Salgash subgroup. The Warrawoona Group is unconformably overlain by the Kelly Group erupted between 3.35 and 3.33 Ga (Van Kranendonk et al., 2006, 2010). The Kelly Group includes a ~1.5 km-thick basal unit of komatiites overlain by an up to 5 km-thick sequence of interbedded komatiitic and tholeiitic basalts. The Sulphur Springs Group unconformably overlies the Kelly Group and is a suite of ultramafic through rhyolitic volcanic rocks deposited between 3.27 and 3.24 Ga (Buick et al., 2002). The Sulphur Springs

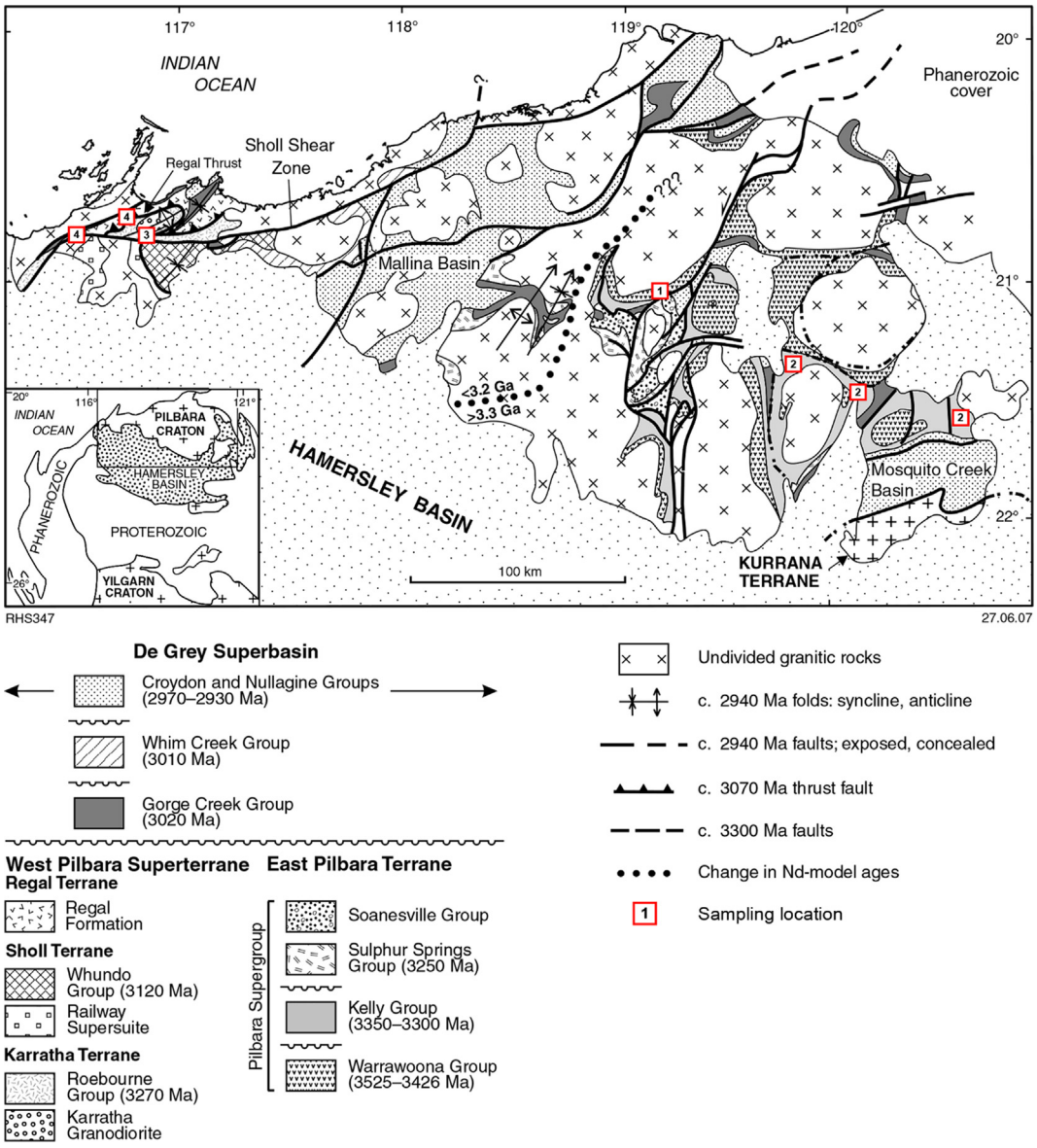

Fig. 1. Sketch geological map of the northern Pilbara Craton, Western Australia, showing location of the East Pilbara Terrane, West Pilbara Superterrane, and sedimentary basins of the De Grey Supergroup (modified after Smithies et al., 2007). Numbered red squares show the location of sampling areas of the (1) Coonterunah Subgroup of the Warrawoona Group; (2) Euro Basalt of the Kelly Group; (3) Ruth Well Formation of the Roebourne Group; (4) Regal Formation of the Regal Terrane. Detailed GPS coordinates, when available during the time of original sampling, are presented in Supplementary Table A1.

Group, in turn, is unconformably overlain by banded iron formation, sandstone, and shale of the Soanesville Group (Van Kranendonk et al., 2006). The Warrawoona, Kelly, and Sulphur Springs Groups are thought to have been emplaced during distinct mantle plume events similar to those that formed modern oceanic and continental plateaus (e.g., Arndt et al., 2001; Van Kranendonk et al., 2006; Hickman and Van Kranendonk, 2012).

The WPS (Fig. 1) represents a collage of three fault-bounded tectono-stratigraphic terranes that accreted together and collided with the EPT at ~3.10 Ga (Van Kranendonk et al., 2010). These include the ~3.27–3.25 Ga Karratha Terrane, the ~3.20 Ga Regal Terrane, which is juxtaposed against the Karratha Terrane across the Regal Thrust, and the 3.13–3.11 Ga Sholl Terrane, which is juxtaposed against the other two terranes across the Sholl Shear Zone. The Karratha Terrane is comprised of the Roebourne Group of ultramafic to felsic volcanic and sedimentary rocks and subvolcanic intrusions of the Ruth Well Formation. The Regal Terrane consists mainly of komatiitic and basaltic lavas of the Regal Formation (Figs. 1 and 2).

Samples for this study are from the Coonterunah Subgroup of the Warrawoona Group and the Kelly Group (both in the EPT), the Ruth Well Formation of the Roebourne Group and Regal Formation of the Regal Terrane

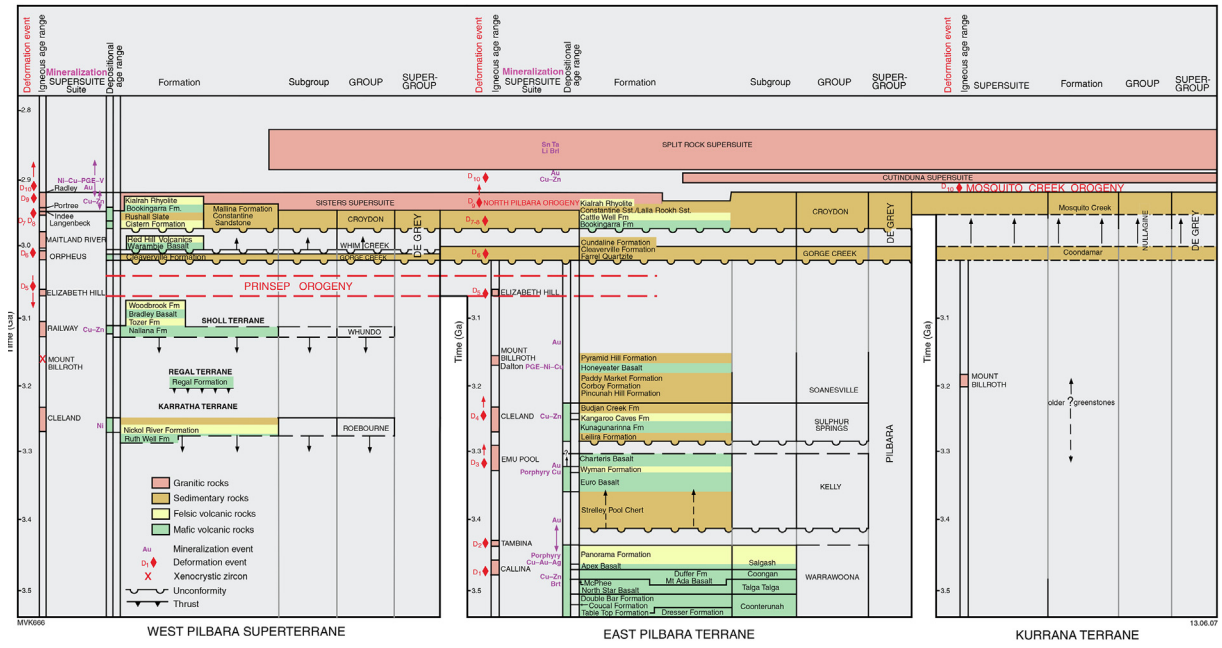

Fig. 2. Stratigraphy and geochronology in the East Pilbara Terrane, West Pilbara Terrane, and the De Grey Supergroup (after Smithies et al., 2007).

(both in the WPS). The GPS coordinates of the location of sample collection sites, where available, rock types, and their lithologies are provided in Supplementary Table A1.

2.1. The Coonterunah Subgroup of the Warrawoona Group

The Coonterunah Subgroup of the Warrawoona Group contains the oldest recognizable komatiites in the Pilbara craton (i.e., ~3.5 Ga; Green et al., 2000). Four drill core chilled margin (179751), spinifex-textured (179755) and olivine cumulate (179756 and 179757) komatiite samples and two spinifex-textured komatiitic basalt (179752 and 179812) samples were supplied for this study by the Geological Survey of Western Australia (GSWA). These samples came from the stratigraphically lowest Table Top Formation of the Coonterunah Subgroup within the East Strelley greenstone belt. All samples were collected from several 1–5 meter thick differentiated lava flows. The rocks were subjected to upper greenschist – lower amphibolite facies metamorphism. As a result, primary olivine and clinopyroxene have been replaced by serpentine and actinolite, and the interstitial matrix by actinolite-tremolite and chlorite. However, original spinifex and cumulate textures are well preserved.

2.2. The Kelly Group

The Kelly Group komatiite and komatiitic basalt drill core samples are from the Euro Basalt Formation, the most voluminous mafic unit of the Pilbara Supergroup (Van Kranendonk et al., 2006). A total of nine komatiitic basalt and three komatiite samples were analyzed in this study. Five komatiitic basalt samples (179881 through 179885) are from the Sandy Creek section of the Kelly greenstone belt, whereas two samples (179827 and 179828) are from its Camel Creek section. The remaining two komatiitic basalt samples (180220 and 180221) are from the Eastern Creek section of the Mt. Elsie greenstone belt. Most komatiitic basalt samples are characterized by well-developed pyroxene spinifex textures. Two olivine cumulate komatiite samples (179815 and 179816) are from the Camel Creek section of the Kelly greenstone belt. One olivine spinifex-textured sample (176773) is from the Kitty's Gap section of the Marble Bar greenstone belt.

2.3. The Ruth Well Formation of the Roebourne Group

The Ruth Well samples for this study are archived in the collection of the Sedgwick Museum of Earth Sciences, University of Cambridge, UK. The drill core was recovered during a Ni-Cu sulfide prospecting campaign in the Ruth Well area in the 1970s and sampled in 1979 by E.G. Nisbet, from the on-site core stack near 20°51′S 116°52′E, with permission from the Whim Creek Mining company. All drill core samples were from depths well below modern-day weathering. A total of eleven komatiite and one komatiitic basalt drill core samples were selected for this study.

Additional six komatiitic basalt samples were collected in local surface outcrops near the drilling site (Nisbet and Chinner, 1981). The komatiites are represented almost exclusively by olivine spinifex-textured rocks, whereas the komatiitic basalts are massive or pillow-textured lavas. The rocks have been metamorphosed under the upper greenschist to lower amphibolite facies conditions (Nisbet and Chinner, 1981) and, as a result, the primary mineralogy has been almost completely obliterated. The komatiites have been transformed into tremolite-chlorite-antigorite rocks, whereas the komatiitic basalts have been

transformed into amphibolites. However, rocks are little deformed, with the spinifex and cumulate textures (komatiites) and pillow textures (komatiitic basalts) being well preserved.

2.4. The Regal Formation of the Regal Terrane

The Regal Formation of the Regal Terrane was sampled in drill core by the Geological Survey of Western Australia, GSWA (Smithies et al., 2007). Six komatiite samples (176720–176725) were collected near the Dampier Railway section at the base of the stratigraphic sequence composed of thick differentiated komatiite lava flows and, except for one spinifex-textured sample (176723), are represented by olivine cumulates. One basaltic sample (176736) was collected higher in the sequence, near the Preston section. All sampled rocks have been metamorphosed under lower amphibolite facies conditions, which resulted in near-complete obliteration of the primary mineralogy, although the original olivine spinifex- and cumulate textures are well preserved.

3. ANALYTICAL TECHNIQUES

3.1. Sample preparation and mineral separation

The procedures for sample preparation closely followed those described in detail by Puchtel et al. (2020). Hand specimens 0.5–1.0 kg in weight collected from surface outcrops (Ruth Well) or fragments of drill core 10–20 cm in length (Coonterunah, Kelly, Ruth Well, and Regal) were cut into 1–2 cm thick slabs using a diamond saw. Millimeter-thick slices were cut off the slabs for thin sectioning that was performed at the Institute of Geology of Ore Deposits, Petrology, Mineralogy and Geochemistry, Russian Academy of Sciences (IGEM) in Moscow. The slabs were abraded on all sides using SiC sandpaper to remove saw and drill bit marks, rinsed in de-ionized water, dried, and crushed in a jaw crusher with alumina-faced jaws. A 200-g aliquot of crushed sample was pre-ground in a shatter box equipped with alumina grinding container and puck, then re-ground to a flour-grade powder in an alumina-faced disk mill; the resultant powder aliquots were used for all geochemical analyses.

The pure clinopyroxene, plagioclase, and chromite separates were obtained at IGEM using the combination of heavy liquid and magnetic separation techniques followed by handpicking.

3.2. Analysis of major, minor, and lithophile trace elements

Major and minor element analyses were carried out at Franklin and Marshall College on fused glass discs using a Phillips 2404 XRF vacuum spectrometer following the protocol of Mertzman (2000). Typical accuracy of the analyses was ~2% relative for major elements present in concentrations greater than 0.5% and ~5% relative for the rest of the major and the minor elements, as determined *via* analysis of the USGS Geochemical Reference Materials (GRM) BIR-1, BCR-1, and BHVO-2 as unknowns (Puchtel et al., 2018, 2020).

Lithophile trace element and transition metal abundances were determined at the *Plasma Laboratory (PL)*, University of Maryland College Park, using the standard addition solution inductively-coupled plasma mass-spectrometry technique (SA-ICP-MS) following the protocol outlined in Puchtel et al. (2016b, 2018) and Nicklas et al. (2016, 2018).

3.3. Re-Os isotopic compositions and HSE abundances

To obtain the Re-Os isotopic and HSE abundance data, the analytical protocols detailed in Puchtel et al. (2018, 2020) were followed. Approximately 1.5 g of whole-rock sample powder or 5.0–50 mg of chromite separates, 6 mL of triple-distilled concentrated HNO_3, 3 mL of triple-distilled concentrated HCl, and appropriate amounts of mixed ^{185}Re-^{190}Os and HSE (^{99}Ru, ^{105}Pd, ^{191}Ir, ^{194}Pt) spikes were sealed in double internally-cleaned, chilled 25 mL Pyrex™ borosilicate Carius tubes and heated to 270 °C for 96 hours. Osmium was extracted from the acid solution by CCl_4 solvent extraction (Cohen and Waters, 1996), back-extracted into conc. HBr, and purified via microdistillation (Birck et al., 1997). Ruthenium, Pd, Re, Ir, and Pt were separated and purified using anion-exchange chromatography following a protocol modified after Rehkämper and Halliday (1997).

Osmium isotopic measurements were done via negative thermal ionization mass spectrometry (N-TIMS: Creaser et al., 1991). All samples were analyzed using a secondary electron multiplier (SEM) detector of a *ThermoFisher Triton* mass spectrometer at the *Isotope Geochemistry Laboratory (IGL)*, University of Maryland College Park. The in-run precision of measured $^{187}Os/^{188}Os$ ratios for all samples was between 0.03% and 0.06% relative. The $^{187}Os/^{188}Os$ ratio of 300–500 pg loads of the in-house *Johnson-Matthey* Os standard measured during the two-year period leading up to the current analytical sessions averaged 0.11377 ± 10 (2SD, $N = 64$). This average $^{187}Os/^{188}Os$ value is within the uncertainty of the average $^{187}Os/^{188}Os = 0.1137950 \pm 18$ measured for the *Johnson-Matthey* Os standard on the Faraday cups of the *IGL Triton* (Puchtel et al., 2020); as such, no instrumental mass-bias corrections were made. The 2SD uncertainty obtained characterizes the external precision of the isotopic analyses (0.09%), which was used to estimate the true uncertainty on the measured $^{187}Os/^{188}Os$ ratio for each individual sample in this study.

The measurements of Ru, Pd, Re, Ir, and Pt were performed at the *PL* on Faraday cups of a *ThermoFisher Neptune Plus* ICP-MS in static mode using 10^{13} Ω amplifiers for all masses of interest. Instrumental isotopic mass fractionation was monitored and corrected for by interspersing samples and standards. The external precision of the analyses was estimated, on the basis of standard measurements performed during the period of the analytical campaign, to be $^{185}Re/^{187}Re = 0.3\%$, $^{99}Ru/^{101}Ru = 0.3\%$, $^{191}Ir/^{193}Ir = 0.2\%$, $^{194}Pt/^{196}Pt = 0.10\%$, and $^{105}Pd/^{106}Pd = 0.10\%$ relative (2SD). The accuracy of the

data was assessed by comparing the results for the reference materials IAG MUH-1 (Austrian harzburgite), IAG OKUM (ultramafic komatiite), and NRC TDB-1 (Diabase PGE Rock Material), obtained at the *IGL,* with the reference values. Concentrations of all HSE and Os isotopic compositions obtained at the *IGL* are within the uncertainties of the certified reference values for these materials (Puchtel et al., 2020).

The average total analytical blank (TAB) measured during the present analytical campaign was (in pg): Ru 6.0, Pd 17, Re 0.53, Os 0.42, Ir 1.2, and Pt 174 ($N = 9$). The average TAB constituted less than 0.2% for Os, Ir, and Pd, less than 0.3% for Ru, and less than 2% for Pt of the total amount of element analyzed. The average TAB for Re constituted between 0.1 and 10% of the total element analyzed. We therefore cite ±0.2% as the uncertainty on the concentrations of Os, Ir, and Pd, ±0.3% as the uncertainty on the concentrations of Ru, and between 0.3 and 8.5% on the concentrations of Re, of the total amount of element analyzed. The calculated uncertainty on the Re/Os ratio was propagated for each sample by combining the estimated uncertainties on the Re and Os abundances for each sample. These uncertainties vary between 0.30 and 8.5% relative.

3.4. Tungsten isotopic compositions and abundances

The W isotope analyses were carried out at the *IGL*. For each sample, between 5 and 50 grams of powder were processed to obtain at least 1 μg of W necessary for high-precision W isotope measurements. Each sample was digested in up to four 360 mL Savillex Teflon screw-cap vials using a 5:1 mixture of double-distilled concentrated HF + HNO_3 on a hot plate at 150 °C for one week. Sample solutions were evaporated to dryness and treated with concentrated HNO_3 on the hotplate overnight to break down the fluorides. Following dry-down, the residues were converted into the chloride form by repeated dissolutions in double-distilled 8 *M* HCl and subsequent dry-downs. The residues were finally re-dissolved in 30 mL of a mixture of 0.4*M* HCl + 0.5*M* HF on the hotplate overnight. The sample solutions were centrifuged and the W in the supernatant separated and purified using the two-stage anion-exchange chromatography protocol of Nagai and Yokoyama (2014), with some modifications. According to the Nagai and Yokoyama (2014) protocol, up to 1 g of sample can be loaded on a primary column per 1 mL of anion exchange resin (page 4861, last paragraph). We modified their protocol by using primary columns with 10 mL of anion exchange resin, and loaded up to 10 grams of sample per column, with up to 6 columns per sample used. The amounts of reagents used were scaled up accordingly (i.e., increased 10-fold). In addition, since separation of Mo was not intended for this study, during the primary column separation, W was collected in a mixture of 9*M* HCl + 3*M* HF, not 9*M* HCl + 1*M* HF, which afforded higher chemistry yields for W. Tungsten recovery in our modified procedure was better than 90%.

Tungsten isotopic compositions were measured by N-TIMS on a *ThermoFisher Triton* mass spectrometer at the *IGL* using a 2-line multi-static acquisition protocol and following a slightly modified technique of Archer et al. (2017). Isotope ratios $^{186}W^{16}O_2^{18}O$ and $^{187}Re^{16}O_2^{18}O$ were measured on every line of the acquisition protocol using 10^{12} Ω amplifiers, thus, allowing per-integration oxide interference corrections. The rest of the isotope ratios were measured using 10^{11} Ω amplifiers. The effects of instrumental mass-fractionation were corrected for using $^{186}W/^{183}W = 0.92767$ or $^{186}W/^{184}W = 1.98594$ (Archer et al., 2017).

All data are reported as $\mu^{182}W$ and $\mu^{183}W$, which are the part per million (ppm) deviations of $^{182}W/^{184}W$ and $^{183}W/^{184}W$, respectively, in a given sample from those of the in-house *Alfa Aesar* laboratory W standard. Uncertainties on $\mu^{182}W$, based on the 2SD uncertainty of the *Alfa Aesar* laboratory W standard run during each analytical session, were between ±2.2 and ±4.3 ppm, with an average value of ±3.3 ppm. The long-term 2SD uncertainty on $\mu^{182}W$ of the *Alfa Aesar* laboratory standard run during the entire 2.5-year analytical campaign was ±6.6 ppm ($N = 47$).

Several studies reported nuclear field shift (NFS) effects on isotope ^{183}W during measurements (e.g., Tappe et al., 2020), which can create analytical artifacts when correcting for instrumental mass-bias using the $^{186}W/^{183}W$ ratio. The analytical protocol of Archer et al. (2017) ensures that NFS effects on ^{182}W are minor and within the analytical uncertainty. For instance, in our study, the mass bias-corrected $\mu^{182}W$ values are identical, within uncertainties, when normalized to $^{186}W/^{183}W$ (6/3) or $^{186}W/^{184}W$ (6/4). Additionally, in all samples, the measured $^{183}W/^{184}W$ ratios were identical, within uncertainties (average ± 4 $\mu^{183}W$ units, 2SD), to the average $^{183}W/^{184}W$ ratios measured in the *Alfa Aesar* laboratory W standard.

Tungsten abundances were determined by isotope dilution ICP-MS. Approximately 100 mg of sample powder and a ^{182}W-enriched spike were equilibrated in 15 mL screw-cap *Savillex* Teflon vials using a 5:1 mixture of double-distilled concentrated HF + HNO_3 at 180 °C for 3–4 days, followed by dry down of the solutions. Residues were treated with double-distilled concentrated HNO_3 and traces of H_2O_2 at 120 °C. After evaporation to dryness, residues were converted into the chloride form by dissolutions in 6*M* HCl, followed by dry downs. Residues were re-dissolved in 2 mL of a 0.4*M* HCl + 0.5*M* HF mixture, and W purified using the previously established anion-exchange chromatography protocol (*e.g.,* Kleine et al., 2004a). Concentrations were measured using the *ThermoFisher Neptune Plus* ICP-MS at the *PL*. Typical uncertainties were ~0.5% relative.

3.5. Sm-Nd isotopic compositions and abundances

The Sm-Nd isotopic data were collected at the *IGL* following the protocol of Puchtel et al. (2020). Between 200 and 500 mg of whole-rock komatiite or basalt sample powder, 150 mg of pure clinopyroxene and 50 mg of pure plagioclase separates, were sealed in 15 mL screw-cap *Savillex* Teflon vials with 7 mL double-distilled concentrated HF, 1.5 mL HNO_3, and appropriate amounts of mixed

^{149}Sm-^{150}Nd spike and digested on a hotplate at 180 °C for 96 hours. The REE were separated from the silicate matrix using the standard cation-exchange chromatography. Neodymium and Sm were further separated from the other REE and each other using HDEHP column extraction, or reversed-phase partition, chromatography. The resultant Nd and Sm cuts were used for the measurements of the Nd and Sm isotopic compositions.

Measurements of the Nd isotopic compositions were performed on Faraday cups of the *ThermoFisher Neptune Plus* ICP-MS at the *PL* in static mode using 10^{11} Ω amplifiers on all masses except for ^{147}Sm, on which a 10^{13} Ω amplifier was used. The measurements were followed by off-line correction for spike contributions. For each sample, 100–200 ratios were collected with 8 *s* integration times in blocks of 100 ratios each. For every block of data collected, the peaks were centered, and a 60 s baseline measurement was performed for each Faraday cup/amplifier pair without beam deflection, and this baseline was then automatically subtracted from the sample beam. The effects of instrumental mass fractionation were corrected for relative to ^{146}Nd/^{144}Nd = 0.7219 using the exponential law. A total of six to ten 60 ppb AMES Nd standard solutions were run during each analytical session, with 100 to 200 ratios collected during each measurement. The in-run precision of the measured ^{143}Nd/^{144}Nd ratio for both the samples and standards was between 5 and 7 ppm (2SE). During the course of the present analytical campaign, the external precision of the 60 ppb AMES Nd standard solution measurements for ^{143}Nd/^{144}Nd was ±10 ppm (2SD). The average ^{143}Nd/^{144}Nd measured for the AMES Nd standard during each analytical session was used to calculate the instrumental mass-bias coefficient for correction of the measured ^{143}Nd/^{144}Nd in the samples using the long-term average ^{143}Nd/^{144}Nd value measured precisely for the AMES Nd standard on the *IGL ThermoFisher Triton* (0.512152 ± 2; Puchtel et al., 2018).

In order to assess the accuracy of the analyses, several separate powder aliquots of USGS GRM BIR-1 and BCR-1 were processed and analyzed using the same analytical protocol (Supplementary Table A2). The measured ^{143}Nd/^{144}Nd ratios for both GRM are identical, within their respective uncertainties, to the GeoRem preferred values, as well as to the average high-precision value for BCR-1 obtained using the *IGL ThermoFisher Triton* (0.512645 ± 1; Puchtel et al., 2018).

Measurements of the spiked Sm isotopic compositions were also performed on the Faraday cups of the *ThermoFisher Neptune Plus* ICP-MS at the *PL* in static mode using 10^{11} Ω amplifiers on all masses except for ^{155}Gd, on which a 10^{13} Ω amplifier was used. For each sample, 20-40 ratios were collected with 8 sec integration times in blocks of 20 ratios each. Before each sample measurement, a 60 s baseline measurement was performed for each Faraday cup/amplifier pair without beam deflection, and this baseline was then automatically subtracted from the sample beam. The effects of instrumental mass fractionation were corrected for relative to ^{147}Sm/^{152}Sm = 0.56081 using the exponential law. The uncertainty on the Sm/Nd ratio in the samples analyzed was estimated on the basis of replicate analyses of the USGS GRM BCR-1 (^{147}Sm/^{144}Nd = 0.13941 ± 0.00014) to be 0.10% relative (2SD).

3.6. Lu-Hf isotopic compositions and abundances

The Hf isotopic compositions and Lu and Hf concentrations were determined at the *IGL* and the *Earth and Planets Laboratory* (*EPL*), Carnegie Institution for Science, following the protocol described in Puchtel et al. (2020). At the *IGL*, approximately 500 mg of the whole-rock sample powder were weighted out in 25 mL Teflon inserts of Parr bombs with 7 mL double-distilled concentrated HF, 1.5 mL HNO_3, and an appropriate amount of mixed ^{176}Lu-^{178}Hf spike, sealed in stainless steel jackets and digested in an oven at 170 °C for one week. The inserts were then removed from the steel jackets, opened, the solutions transferred into 15 mL screw-cap Teflon vials, dried down, 0.7 mL of concentrated *SeaStar* $HClO_4$ added to the residue, the vials sealed and kept on a hotplate at 160 °C for 24 hours. The solutions were then dried down at ~230 °C, and the residues converted into the chloride form using 6*M* HCl. This step was repeated several times until clear solutions were obtained, and then dried down.

At the *EPL*, the residue was re-dissolved in 5 mL of 1*M* HCl – 0.1*M* HF mixture, and loaded onto a 0.6 × 20 cm column filled with AG50W-X8 200–400 mesh cation-exchange resin. High field strength elements, including Hf, were eluted in the loading solution and an additional 5 mL of 1*M* HCl – 0.1*M* HF. After eluting 44 mL of 2.5*M* HCl, heavy REE, including Lu, were eluted in 12 mL of 4*M* HCl. Hafnium was purified on a 0.6 × 10 cm column of Eichrom LN resin (100–150 μm bead size) by loading the sample in 5 mL of 2.5*M* HCl, followed by washes of 10 mL 2.5*M* HCl, 10 mL 6*M* HCl, 4 mL H_2O, 40 mL of a mixture consisting of 0.09*M* Citric acid – 0.45*M* HNO_3 – 1% H_2O_2, 5 mL of the same solution without H_2O_2, and, finally, 20 mL of 6*M* HCl – 0.06*M* HF. Hafnium was then eluted in 8 mL of 6*M* HCl – 0.4*M* HF. Lutetium was purified using Eichrom LN resin (50–100 μm bead size) on a 0.4 × 7 cm column. The HREE fraction from the first column was loaded in 2.5*M* HCl, followed by a wash of 30 mL 2.5*M* HCl to remove much of the other HREE, then Lu was collected in 10 mL of 6*M* HCl. The resultant Hf and Lu cuts were used for the measurements of the Hf and Lu isotopic compositions.

Measurements of the Hf isotopic compositions were performed on the Faraday cups of the *ThermoFisher Neptune Plus* ICP-MS at the *PL* in static mode, using 10^{11} Ω amplifiers on all Hf masses and on the ^{181}Ta mass, whereas ^{173}Yb, ^{175}Lu, and ^{183}W masses were measured using 10^{13} Ω amplifiers. The measurements were followed by off-line corrections for spike contributions. For each sample, 200–300 ratios were collected with 8 *s* integration time in blocks of 100 ratios each. Before each sample measurement, a 60 s baseline measurement was performed for each Faraday cup/amplifier pair without beam deflection, and this baseline was then automatically subtracted from the sample beam. Instrumental mass fractionation was corrected for relative to ^{179}Hf/^{177}Hf = 0.7325 using the exponential law. The Yb, Lu, Ta, and W isobaric interferences were

Table 1
Major and minor element data for the Pilbara Craton komatiites and basalts.

Locality	Coonterunah						Kelly											
Lithology	Komatiite				Basalt		Komatiite			Basalt								
Sample No.	179751	179755	179756	179757	179752	179812	176773	179815	179816	179827	179828	179881	179882	179883	179884	179885	180220	180221
SiO_2	47.4	48.1	46.2	45.3	47.4	46.0	48.1	44.7	45.3	49.3	47.9	50.3	53.4	51.5	52.6	52.8	53.1	50.1
TiO_2	0.340	0.310	0.282	0.222	0.651	0.901	0.341	0.203	0.271	1.16	1.20	0.359	0.310	0.370	0.540	0.451	0.660	0.559
Al_2O_3	8.09	7.38	6.42	5.50	10.1	16.3	7.64	4.61	5.74	7.73	8.35	13.4	11.2	13.3	11.5	8.70	9.54	12.1
Fe_2O_3	12.4	10.8	11.1	11.6	13.1	16.1	12.9	11.1	12.0	15.0	17.4	11.2	10.7	11.3	11.8	11.5	11.1	11.5
MnO	0.184	0.182	0.169	0.190	0.206	0.100	0.346	0.181	0.186	0.217	0.261	0.203	0.172	0.199	0.176	0.218	0.162	0.157
MgO	23.3	24.1	28.9	32.8	14.6	17.7	22.0	33.2	29.7	10.6	11.4	13.0	15.2	11.6	10.6	14.0	14.1	13.4
CaO	7.39	8.35	6.08	3.38	12.0	2.34	7.07	4.96	6.06	13.6	11.5	8.84	8.63	10.8	9.13	11.0	7.72	9.15
Na_2O	0.219	0.155	0.104	0.022	1.25	0.017	0.355	0.222	0.152	2.01	1.41	2.04	0.17	0.56	3.02	1.06	3.35	2.23
K_2O	0.023	0.0091	0.019	0.0001	0.237	0.047	0.702	0.057	0.017	0.177	0.191	0.349	0.040	0.013	0.361	0.066	0.037	0.473
P_2O_5	0.031	0.023	0.021	0.018	0.058	0.061	0.022	0.014	0.020	0.079	0.093	0.030	0.027	0.029	0.038	0.028	0.073	0.056
LOI	5.29	5.04	7.63	8.84	1.54	9.54	8.59	6.07	5.51	2.83	5.48	3.73	4.48	3.69	2.56	7.30	3.75	3.14
Cr	3215	3016	4029	4904	1697	1084	2408	2341	2381	668	1148	982	1314	734	563	1138	698	1271
Al_2O_3/TiO_2	23.8	23.8	22.8	24.8	15.6	18.1	22.4	22.8	21.2	6.66	6.96	37.4	36.1	36.1	21.3	19.3	14.5	21.6

Locality	Ruth Well																
Lithology	Komatiite											Basalt					
Sample No.	138308	138239	140258	158691a	158691b	158692a	158692b	158692c	158693	158694	137638	140259	137307	137308	137309	137314	137636	137644
SiO_2	47.1	46.8	44.4	46.2	45.6	45.1	46.1	45.7	46.2	45.8	46.8	51.5	53.0	50.2	49.2	48.0	50.3	50.5
TiO_2	0.394	0.351	0.351	0.360	0.351	0.300	0.359	0.340	0.343	0.360	0.353	0.605	1.02	0.976	1.01	1.02	0.982	0.883
Al_2O_3	4.34	4.01	3.80	3.99	3.80	3.43	3.88	3.64	3.78	4.00	3.91	6.55	11.1	9.95	10.4	10.1	9.88	8.82
Fe_2O_3	12.5	11.9	14.1	13.7	13.8	12.4	11.9	13.0	12.6	13.1	11.9	13.5	12.0	14.1	15.0	17.3	14.3	12.9
MnO	0.140	0.200	0.220	0.150	0.180	0.210	0.170	0.180	0.170	0.190	0.288	0.231	0.195	0.280	0.294	0.309	0.319	0.283
MgO	26.6	28.8	29.9	28.7	30.1	32.5	29.1	31.0	29.8	28.4	29.5	14.2	8.40	8.43	7.98	9.19	9.17	9.22
CaO	7.91	6.86	6.44	5.95	5.14	5.10	7.42	5.21	6.33	7.02	6.19	11.2	10.5	13.2	13.3	11.7	11.6	14.5
Na_2O	0.270	0.301	0.110	0.290	0.290	0.270	0.359	0.310	0.379	0.450	0.178	1.46	3.25	1.80	1.94	1.70	1.80	2.03
K_2O	0.038	0.099	0.148	0.167	0.124	0.058	0.076	0.065	0.079	0.114	0.088	0.404	0.326	0.784	0.748	0.561	1.29	0.574
P_2O_5	0.027	0.026	0.027	0.031	0.028	0.035	0.027	0.027	0.022	0.026	0.028	0.055	0.100	0.099	0.088	0.097	0.118	0.092
LOI	7.26	6.97	6.93	5.94	7.31	8.57	10.70	7.22	6.79	7.22	7.47	1.09	1.01	1.20	1.12	0.63	1.83	0.97
Cr	2498	2419	2274	2268	2285	2079	2334	2325	2202	2277	2247	1282	342	360	296	299	419	573
Al_2O_3/TiO_2	11.0	11.4	10.8	11.1	10.8	11.4	10.8	10.7	11.0	11.1	11.1	10.8	10.9	10.2	10.3	9.87	10.1	10.0

Locality	Regal						
Lithology	Komatiite						Basalt
Sample No.	176720	176721	176722	176723	176724	176725	176736
SiO_2	45.5	45.6	44.1	46.3	46.4	44.5	50.1
TiO_2	0.244	0.165	0.170	0.300	0.244	0.261	1.38
Al_2O_3	2.67	1.98	2.11	3.54	2.77	3.14	13.5
Fe_2O_3	12.1	9.60	11.6	11.8	11.0	12.3	14.8
MnO	0.183	0.156	0.167	0.211	0.164	0.158	0.240
MgO	36.6	41.3	40.8	32.0	36.3	34.7	4.81
CaO	1.69	0.431	0.340	5.20	2.38	4.21	11.1
Na_2O	0.028	0.056	0.018	0.039	0.038	0.149	3.54
K_2O	0.0010	0.036	0.0010	0.0030	0.0001	0.015	0.306
P_2O_5	0.018	0.017	0.011	0.011	0.024	0.020	0.118
LOI	10.09	11.81	11.64	13.90	9.99	9.96	0.82
Cr	4712	1642	1677	2082	1909	2100	208
Al_2O_3/TiO_2	11.0	11.9	12.4	11.8	11.4	12.0	9.77

Analyses are recalculated on an anhydrous basis.
Major element concentrations in wt.%, Cr – in ppm.

corrected for using $^{173}Yb/^{176}Yb = 1.256$, $^{175}Lu/^{176}Lu = 37.70$, $^{181}Ta/^{180}Ta = 8129$, and $^{183}W/^{180}W = 109.0$. A total of six 30 ppb JMC-475 Hf standard solutions were run at the beginning and end of the analytical session, with 200 ratios collected during each measurement. During the measurements, the signal intensities for both the standard and the samples were kept at constant levels, between 1.8 and 2.6 V on the ^{178}Hf mass; the in-run precision of the measured $^{176}Hf/^{177}Hf$ ratio for both samples and standards was 11–13 ppm (2SE). During the course of the present analytical campaign, the external reproducibility of the 30 ppb JMC-475 Hf standard solution measurements for $^{176}Hf/^{177}Hf$ was ±14 ppm (2SD); this value was used to estimate the true uncertainty on the measured $^{176}Hf/^{177}Hf$ in the samples. The average $^{176}Hf/^{177}Hf$ ratio measured for the JMC-475 Hf standard solution during the analytical session was used to calculate the instrumental mass bias coefficient for correction of the measured $^{176}Hf/^{177}Hf$ ratio in the samples using the true value of $^{176}Hf/^{177}Hf = 0.282\,163 \pm 0.000009$, as determined by a multiple dynamic analysis protocol (Blichert-Toft et al., 1997).

In order to assess the accuracy of the analyses, an aliquot of USGS GRM BCR-1 was processed and analyzed together with the samples using the same protocol. The measured $^{176}Hf/^{177}Hf$ ratio and the calculated Hf concentration of BCR-1 are identical, within the uncertainties, to the GeoRem preferred values.

Measurements of the Lu isotopic compositions to determine Lu concentrations were also performed on the Faraday cups of the *ThermoFisher Neptune Plus* ICP-MS at the *PL* in static mode using 10^{11} Ω amplifiers for all masses except for ^{172}Yb, ^{173}Yb, ^{176}Lu, and ^{177}Hf, for which 10^{13} Ω amplifiers were employed. The measurements were followed by off-line corrections for spike contributions. For each sample, 40 ratios were collected with 4 *s* integration time in blocks of 20 ratios each. Before each sample measurement, a 60 s baseline measurement was performed for each Faraday cup/amplifier pair without beam deflection, and this baseline was then automatically subtracted from the sample beam. Instrumental mass fractionation was corrected for by analyzing a 10 ppb Lu standard solution before and after every 4 samples. The Yb and Hf isobaric interferences were corrected for on-line using $^{176}Yb/^{173}Yb = 0.7962$ and $^{176}Hf/^{177}Hf = 0.2822$. The Lu concentration obtained for the USGS GRM BCR-1 in this study was identical, within the uncertainty, to the GeoRem recommended value. The propagated uncertainty on the Lu/Hf ratio in the samples analyzed is estimated to be 0.5%. The total analytical blanks were 70 pg for Hf and 2 pg for Lu.

For the isochron calculations, *Isoplot 3.00* (Ludwig, 2003) and the ^{176}Lu decay constant of 1.867×10^{-11} year^{-1} (Scherer et al., 2001; Söderlund et al., 2004) were used. The $\varepsilon^{176}Hf$ values were calculated as parts per 10,000 deviation of the measured sample $^{176}Hf/^{177}Hf$ at the time of the komatiite lava emplacement from the chondritic reference defined as $^{176}Lu/^{177}Hf = 0.0336$ and $^{176}Hf/^{177}Hf = 0.282785$ (Bouvier et al., 2008).

4. RESULTS

4.1. Major, minor, and lithophile trace element abundance data

The major, minor, and lithophile trace element abundance data for the whole-rock komatiite and basalt samples of the Pilbara Craton, re-calculated on an anhydrous basis, are listed in Tables 1 and 2 and plotted in Figs. 3 and 4.

4.1.1. Komatiites

The MgO abundances in the komatiites studied here vary between 23.3–32.8 wt.% in the Coonterunah lavas, 22.0–33.2 wt.% in the Kelly lavas, 26.6–32.5 wt.% in the Ruth Well lavas, and 32.0–41.3 wt.% in the Regal lavas. As illustrated in Fig. 3, most elements analyzed for the four Pilbara komatiite systems follow trends generally consistent with the olivine-controlled liquid lines of descent, or the so-called olivine control lines (e.g., Arndt, 1986, 1994), indicating immobile behavior during post-magmatic processes, such as syn- and post-eruptive seafloor alteration, later metamorphism, and weathering. Exceptions are U and W, which plot with significant scatter. This is further illustrated in Fig. 4 of Bulk Silicate Earth (BSE)-normalized concentrations, which form near-parallel patterns for all trace elements, except for U and W. It is noted that a similar scatter is also observed for Ca and alkalis (not shown in Fig. 3).

Figs. 3 and 4 reveal significant differences between the four Pilbara komatiite systems. The Coonterunah and Kelly komatiites belong to the Al-undepleted, or Munro-type lavas of Nesbitt et al. (1979), as evidenced by their relatively high absolute Al_2O_3 contents, BSE-like Al_2O_3/TiO_2 ratios, and unfractionated BSE-normalized heavy REE patterns ($Al_2O_3/TiO_2 = 23.8 \pm 1.7$ and 22.1 ± 1.7 vs. 22.4 in BSE, $Gd/Yb_N = 0.96 \pm 0.03$ and 0.91 ± 0.04, respectively, 2SD). Conversely, the Ruth Well and Regal komatiites are depleted in Al and heavy REE ($Al_2O_3/TiO_2 = 11.0 \pm 0.5$ and 11.9 ± 0.8, $Gd/Yb_N = 1.32 \pm 0.04$ and 1.31 ± 0.12, respectively, 2SD). Except for sample 176720 from the Regal Formation ($La/Sm_N = 1.3$), all sample from the four komatiite systems show variable depletions in light REE ($La/Sm_N = 0.80 \pm 0.04$ in Coonterunah, 0.65 ± 0.02 in Kelly, 0.77 ± 0.09 in Ruth Well, and 0.83 ± 0.11 in Regal, ±2SD).

The Coonterunah and Kelly komatiites have similar and significantly lower highly incompatible lithophile trace element abundances, such as LREE and Th, compared to the Ruth Well and Regal komatiites. The latter exhibit similar enrichments in Th and La over Nb and, thus, have negative Nb abundance anomalies ($Nb/Nb^* = 0.51 \pm 0.05$ and 0.55 ± 0.09, respectively, where $Nb/Nb^* = Nb_N/\sqrt{(Th_N \times La_N)}$), whereas no Nb anomalies are observed in the Coonterunah and Kelly komatiites ($Nb/Nb^* = 1.08 \pm 0.02$ and 1.03 ± 0.04, respectively, 2SD).

In this study, because of the relative mobility of W, following Willbold et al. (2015), Liu et al. (2016), and Tusch et al. (2021), we use the ratio of W over the

Table 2
Trace element data (ppm) for the Pilbara Craton komatiites and basalts.

Locality	Coonterunah								Kelly												
Lithology	Komatiite						Basalt		Komatiite				Basalt								
Sample	179751	179755	Replica	179756	179757	Replica	179752	179812	176773	179815	Replica	179816	179827	179828	179881	179882	179883	179884	179885	180220	180221
Sc	24.1	23.3	23.4	21.3	20.1	20.7	30.2	23.6	24.6	20.5	20.4	21.3	34.2	31.5	40.2	41.2	39.9	41.3	49.4	30.3	34.7
V	137	137	136	119	106	108	207	135	143	105	106	120	245	245	220	212	227	237	228	175	194
Ni	1033	1078	1097	1486	1832	1797			1005	1775	1827	1591									387
Cu	191	54.4	47.5	7.36	13.8	13.0	37.5	1.89	3.46	16.9	18.7	33.6	231	180	70.2	53.8	64.9	120	65.7	97.4	1.27
Ga	7.14	6.73	6.88	5.67	4.95	4.80	13.6	14.8	7.39	4.70	4.69	5.55	10.3	13.0	11.2	9.65	11.5	10.6	8.65	9.92	10.6
Y	6.70	6.46	6.53	5.48	4.45	4.48	13.5	14.2	7.08	4.76	4.91	5.76	18.0	19.0	11.6	9.25	11.0	12.3	10.41	21.8	14.8
Zr	16.9	16.4	16.3	14.5	11.6	12.1	48.9	42.3	17.9	11.6	11.3	13.8	68.7	82.1	19.3	17.4	17.9	27.2	21.6	82.4	36.4
Nb	0.805	0.765	0.757	0.636	0.514	0.503	4.45	3.66	0.616	0.365	0.370	0.440	5.86	4.56	0.642	0.477	0.573	1.25	0.884	4.74	1.93
La	0.876	0.847	0.854	0.694	0.554	0.549	5.67	4.87	0.682	0.410	0.403	0.497	9.29	6.24	0.815	0.637	0.738	1.51	1.08	5.51	2.67
Ce	2.64	2.53	2.53	2.06	1.60	1.61	13.5	11.1	2.04	1.23	1.20	1.46	20.6	16.6	2.24	1.61	1.89	4.61	3.25	14.0	6.69
Pr	0.408	0.393	0.396	0.328	0.266	0.258	1.80	1.52	0.346	0.205	0.200	0.246	3.20	2.41	0.335	0.264	0.303	0.702	0.515	1.95	1.15
Nd	2.12	2.06	2.04	1.67	1.36	1.36	7.99	6.97	1.88	1.10	1.09	1.39	14.8	11.8	1.80	1.42	1.67	3.77	2.82	9.50	5.58
Sm	0.680	0.652	0.647	0.562	0.442	0.435	1.96	1.82	0.651	0.405	0.397	0.480	3.55	3.25	0.702	0.553	0.656	1.27	0.988	2.72	1.66
Eu	0.295	0.254	0.245	0.136	0.0963	0.0974	0.891	0.640	0.256	0.167	0.160	0.226	1.13	0.972	0.293	0.244	0.259	0.506	0.349	0.795	0.465
Gd	0.915	0.894	0.881	0.740	0.599	0.594	2.35	2.33	0.906	0.570	0.564	0.684	3.90	3.59	1.17	0.919	1.08	1.72	1.40	3.33	2.08
Tb	0.161	0.157	0.157	0.132	0.107	0.106	0.376	0.387	0.166	0.108	0.106	0.125	0.567	0.571	0.236	0.189	0.225	0.300	0.257	0.561	0.364
Dy	1.13	1.09	1.07	0.912	0.745	0.725	2.40	2.56	1.16	0.757	0.752	0.863	3.34	3.46	1.74	1.43	1.66	2.01	1.74	3.65	2.47
Ho	0.241	0.234	0.232	0.192	0.162	0.160	0.487	0.539	0.252	0.167	0.165	0.192	0.653	0.676	0.398	0.327	0.380	0.426	0.372	0.762	0.525
Er	0.751	0.725	0.718	0.616	0.490	0.482	1.41	1.55	0.773	0.505	0.503	0.592	1.79	1.89	1.22	1.02	1.21	1.27	1.10	2.27	1.56
Tm	0.116	0.112	0.111	0.0954	0.0746	0.0733	0.205	0.229	0.121	0.0756	0.0752	0.0912	0.249	0.268	0.193	0.158	0.184	0.189	0.161	0.336	0.231
Yb	0.767	0.742	0.734	0.639	0.519	0.502	1.36	1.50	0.789	0.513	0.512	0.597	1.62	1.71	1.29	1.10	1.23	1.26	1.06	2.27	1.54
Lu	0.119	0.116	0.114	0.0962	0.0788	0.0777	0.207	0.222	0.124	0.0785	0.0779	0.0932	0.236	0.248	0.198	0.170	0.185	0.186	0.159	0.342	0.226
Hf	0.487	0.468	0.462	0.392	0.328	0.326	1.33	1.17	0.502	0.315	0.316	0.377	1.85	2.13	0.581	0.514	0.574	0.790	0.636	2.10	1.09
Th	0.0808	0.0772	0.0770	0.0662	0.0521	0.0510	0.437	0.340	0.0659	0.0409	0.0401	0.0495	0.659	0.670	0.0817	0.0644	0.0803	0.124	0.0871	0.679	0.238
U	0.0602	0.0166	0.0164	0.0193	0.0146	0.0146	0.134	0.0679	0.0443	0.00923	0.00713	0.0154	0.145	0.162	0.0215	0.0156	0.0193	0.0327	0.0240	0.161	0.0619
W	0.0854	0.0403		0.0823	0.0431		0.0845	0.0630	0.0770	0.0194		0.0395	0.0705	0.142	0.00898	0.0230	0.108	0.0402	0.0199	0.144	0.212
$(La/Sm)_N$	0.810	0.818	0.831	0.778	0.789	0.794	1.82	1.68	0.659	0.638	0.639	0.652	1.65	1.21	0.731	0.724	0.709	0.746	0.685	1.27	1.01
$(Gd/Yb)_N$	0.964	0.974	0.969	0.936	0.933	0.957	1.40	1.25	0.927	0.898	0.891	0.925	1.94	1.70	0.735	0.672	0.713	1.10	1.07	1.19	1.09
Nb/Nb*	1.10	1.08	1.07	1.07	1.09	1.09	1.02	1.03	1.05	1.02	1.05	1.02	0.857	0.808	0.901	0.852	0.851	1.05	1.04	0.886	0.875
W/Th	1.06	0.522		1.24	0.828		0.193	0.185	1.17	0.474		0.799	0.107	0.212	0.110	0.357	1.35	0.325	0.229	0.212	0.889
ΔW, %	82.0	63.6		84.7	77.1		1.78	−2.53	83.7	59.9		76.2	−77.8	10.2	−73.0	46.8	85.9	41.6	17.0	10.3	78.6

Locality	Ruth Well																		
Lithology	Komatiite											Basalt							
Sample	138308	138239	140258	158691a	158691b	158692a	158692b	158692c	158693	158694	137638	140259	137307	137308	137309	137314	137636	137644
Sc	19.9	18.2	17.8	18.0	17.6	16.1	18.4	17.1	17.3	18.7	18.6	35.4	37.4	34.3	33.6	32.0	29.9	39.1
V	132	121	118	125	113	102	122	110	115	124	119	204	259	239	240	254	226	236
Ni	1282	1505	1577	1509	1671	1913	1570	1679	1612	1513	1578	256	122	118	138	187	105	166
Cu	8.72	52.7	7.95	64.2	77.3	33.3	59.9	45.1	49.2	24.2	10.7	35.6	89.5	14.5	6.95	0.878	0.634	9.62
Ga	6.37	5.72	5.63	5.86	5.40	4.91	5.79	5.32	5.52	5.81	5.70	9.36	11.9	12.3	13.1	13.9	12.3	11.1
Y	8.36	7.48	7.15	7.67	7.04	6.49	7.38	6.89	7.34	7.64	7.40	14.2	22.2	19.9	20.5	20.7	20.1	19.2
Zr	25.3	22.6	20.9	22.9	21.4	19.0	22.5	20.0	22.2	23.4	22.7	47.2	70.6	64.6	69.2	67.4	67.0	60.4
Nb	0.637	0.583	0.561	0.617	0.549	0.506	0.626	0.527	0.558	0.594	0.581	2.08	3.22	2.65	2.88	3.05	3.06	2.81
La	1.22	1.06	0.98	1.09	0.969	0.927	1.05	1.13	1.15	1.15	1.12	3.01	5.02	5.28	5.66	5.71	5.71	5.15
Ce	3.03	2.71	2.51	2.71	2.62	2.18	2.85	2.41	2.70	2.90	2.80	7.15	14.3	14.3	15.3	15.5	13.9	11.9
Pr	0.505	0.426	0.424	0.435	0.434	0.380	0.457	0.431	0.428	0.459	0.443	1.24	2.05	2.07	2.14	2.17	1.98	1.83
Nd	2.70	2.36	2.26	2.45	2.38	2.05	2.48	2.28	2.31	2.50	2.33	6.26	10.4	10.1	10.8	10.6	9.97	9.15
Sm	0.984	0.884	0.841	0.889	0.871	0.750	0.921	0.840	0.844	0.927	0.902	2.02	3.15	2.92	3.11	3.08	2.87	2.78
Eu	0.306	0.333	0.263	0.324	0.241	0.331	0.346	0.346	0.336	0.346	0.236	0.739	1.17	1.24	1.28	1.24	1.17	0.975
Gd	1.33	1.18	1.14	1.22	1.16	1.01	1.18	1.13	1.17	1.26	1.17	2.47	3.73	3.54	3.69	3.69	3.51	3.37
Tb	0.236	0.214	0.203	0.218	0.202	0.182	0.213	0.195	0.203	0.220	0.212	0.413	0.613	0.577	0.596	0.576	0.582	0.545
Dy	1.53	1.38	1.33	1.40	1.33	1.18	1.41	1.28	1.33	1.41	1.36	2.62	3.84	3.62	3.79	3.75	3.63	3.43
Ho	0.306	0.272	0.263	0.276	0.260	0.233	0.278	0.259	0.273	0.279	0.275	0.529	0.772	0.724	0.770	0.773	0.758	0.680
Er	0.867	0.793	0.758	0.783	0.753	0.675	0.796	0.730	0.784	0.796	0.756	1.51	2.26	2.06	2.20	2.14	2.07	1.94
Tm	0.128	0.115	0.108	0.118	0.111	0.0951	0.116	0.105	0.111	0.119	0.115	0.218	0.316	0.294	0.311	0.311	0.291	0.277
Yb	0.814	0.728	0.707	0.735	0.696	0.630	0.737	0.681	0.721	0.753	0.737	1.43	2.07	1.98	2.04	2.02	1.99	1.81
Lu	0.118	0.105	0.100	0.106	0.100	0.0884	0.105	0.0943	0.103	0.108	0.105	0.207	0.303	0.289	0.295	0.291	0.287	0.268
Hf	0.692	0.656	0.574	0.639	0.567	0.530	0.655	0.591	0.599	0.655	0.605	1.33	2.04	1.93	1.96	1.98	1.93	1.70
Th	0.174	0.162	0.150	0.163	0.150	0.139	0.164	0.154	0.148	0.161	0.156	0.535	0.869	0.830	0.806	0.871	0.835	0.710
U	0.0714	0.0652	0.0407	0.0418	0.0393	0.0778	0.0649	0.0761	0.0753	0.0494	0.0703	0.135	0.226	0.225	0.212	0.238	0.240	0.176

W	0.538	0.686	0.187	0.607	0.562	0.703	0.579	0.629	0.565	0.537	0.208	0.276	0.225	0.377	0.384	0.285	0.450	0.278
$(La/Sm)_N$	0.781	0.753	0.735	0.775	0.700	0.778	0.721	0.849	0.855	0.778	0.784	0.938	1.00	1.14	1.14	1.17	1.25	1.17
$(Gd/Yb)_N$	1.32	1.31	1.31	1.35	1.34	1.30	1.30	1.33	1.31	1.35	1.28	1.39	1.46	1.45	1.46	1.48	1.43	1.50
Nb/Nb*	0.500	0.510	0.529	0.529	0.522	0.509	0.546	0.457	0.490	0.500	0.502	0.592	0.559	0.458	0.487	0.495	0.507	0.532
W/Th	3.09	4.24	1.25	3.73	3.76	5.05	3.54	4.09	3.82	3.33	1.33	0.515	0.259	0.455	0.477	0.327	0.539	0.391
ΔW, %	93.8	95.5	84.8	94.9	94.9	96.2	94.6	95.3	95.0	94.3	85.7	63.1	26.5	58.2	60.1	41.9	64.8	51.5

Locality	**Regal**									
Lithology	**Komatiite**									**Basalt**
Sample	**176720**	**176721**	**176722**	**Replica**	**176723**	**Replica**	**176724**	**Replica**	**176725**	**176736**
Sc	13.7	11.1	12.4	12.2	16.0	16.0	16.2	16.3	14.5	37.6
V	110	55.9	65.8	63.7	102	99.5	83.2	81.9	84.5	357
Ni	2298	2743	2648	2712	1816	1857	2309	2211	2070	101
Cu	3.72	2.96	3.90	4.21	4.56	5.11	2.75	2.70	2.17	142
Ga	5.25	2.76	2.89	2.99	4.78	4.85	3.80	3.81	4.24	17.2
Y	5.81	3.30	3.50	3.34	6.63	6.51	4.99	5.35	5.61	30.6
Zr	17.5	10.3	9.41	9.17	18.2	18.2	14.6	14.5	15.8	90.8
Nb	0.701	0.283	0.305	0.290	0.526	0.508	0.442	0.439	0.432	3.95
La	1.44	0.566	0.472	0.472	0.945	0.970	0.783	0.776	0.838	5.32
Ce	2.93	1.16	1.21	1.26	2.27	2.31	1.86	1.94	1.86	12.7
Pr	0.448	0.224	0.187	0.183	0.368	0.364	0.278	0.277	0.302	2.22
Nd	2.18	1.22	1.06	1.10	1.96	1.95	1.45	1.45	1.59	11.2
Sm	0.723	0.442	0.379	0.384	0.739	0.747	0.537	0.541	0.608	3.46
Eu	0.233	0.171	0.132	0.139	0.178	0.177	0.171	0.172	0.165	1.07
Gd	0.961	0.589	0.496	0.509	1.03	1.04	0.749	0.764	0.865	4.46
Tb	0.165	0.101	0.0910	0.0925	0.185	0.190	0.136	0.139	0.153	0.778
Dy	1.04	0.641	0.597	0.618	1.26	1.26	0.907	0.917	1.05	5.29
Ho	0.212	0.127	0.123	0.125	0.245	0.247	0.187	0.187	0.203	1.13
Er	0.601	0.353	0.336	0.346	0.705	0.710	0.531	0.534	0.575	3.30
Tm	0.0866	0.0496	0.0475	0.0483	0.101	0.102	0.0755	0.0760	0.0868	0.480
Yb	0.560	0.332	0.308	0.318	0.656	0.664	0.488	0.491	0.537	3.24
Lu	0.0802	0.0462	0.0455	0.0467	0.0937	0.0956	0.0697	0.0702	0.0766	0.479
Hf	0.478	0.273	0.264	0.266	0.496	0.492	0.377	0.373	0.414	2.61
Th	0.144	0.0680	0.0654	0.0661	0.138	0.139	0.102	0.108	0.117	0.614
U	0.0544	0.0202	0.0326	0.0342	0.0251	0.0269	0.0338	0.0351	0.0250	0.150
W	0.315	0.365	0.328	0.328	0.337	0.317	0.357	0.357	0.308	0.396
$(La/Sm)_N$	1.26	0.806	0.784	0.774	0.804	0.818	0.917	0.903	0.868	0.968
$(Gd/Yb)_N$	1.39	1.44	1.30	1.30	1.27	1.27	1.24	1.26	1.30	1.11
Nb/Nb*	0.556	0.523	0.629	0.594	0.527	0.501	0.567	0.549	0.498	0.790
W/Th	2.18	5.37	5.02	4.97	2.44	2.29	3.50	3.30	2.63	0.645
ΔW, %	91.3	96.5	96.2	96.2	92.2	91.7	94.6	94.2	92.8	70.6

Note. Analyses were recalculated on an anhydrous basis using the LOI values from Table 1.
N-normalized to the BSE values of Hofmann (1988).

fluid-immobile element Th that has a similar incompatibility during mantle melting (e.g., Arevalo and McDonough, 2008) to quantify the degree of enrichment/depletion in W abundances relative to those that would be expected on the basis of its magmatic behavior by comparing it with the W/Th = 0.19 in the BSE (McDonough and Sun, 1995). The degree of enrichment/depletion is expressed in per cent (Table 2) and calculated using Eq. (1) from Liu et al. (2016):

$$\Delta W_{enrichment}\ (\%) = 100 \times [(W/Th)_{sample} - (W/Th)_{BSE})]/(W/Th)_{sample}$$

All komatiite samples analyzed are enriched in W over Th relative to $W/Th_{BSE} = 0.19$, with W/Th ratios ranging between 0.52–1.1, 0.47–1.2, 1.3–5.1, and 2.2–5.4 in the Coonterunah, Kelly, Ruth Well, and Regal lavas, respectively (Table 2). Consequently, the komatiites exhibit positive W abundance anomalies in the BSE-normalized trace element abundance plots in Fig. 4. The largest relative enrichments are observed in the Ruth Well and Regal komatiite systems, while the Coonterunah and Kelly lavas show a factor of 2–5× smaller enrichments.

4.1.2. Basalts

In the basalts, the MgO contents range from 14.6 to 17.7, 10.6 to 15.2, and 7.98 to 14.2 wt.% in the Coonterunah, Kelly, and Ruth Well lavas, respectively. The only analyzed basaltic sample from the Regal Formation (176736) has 4.81 wt.% MgO (Table 1). Apart from the Regal Formation basalt sample, the majority of the basalts analyzed contain >9.0 wt.% MgO and, therefore, are classified as komatiitic basalts (Arndt and Nisbet, 1982).

In the MgO variation diagrams in Fig. 3, the data for all basalts, except for some Kelly lavas, do not plot on the same olivine control lines as the respective komatiites, likely indicating that most rocks within the four komatiite-basalt assemblages cannot be linked by simple fractionation of olivine from a common komatiitic magma, but, in addition to olivine, require extensive fractionation of clinopyroxene.

The two Coonterunah komatiitic basalts studied are enriched in LREE ($La/Sm_N = 1.7–1.8$), depleted in HREE ($Gd/Yb_N = 1.3–1.4$), and, similarly to the komatiites, show no Nb abundance anomalies (Nb/Nb* = 1.02–1.03). The W/Th values in the two samples range between 0.185 and 0.193 and are, thus, similar to the BSE value.

The nine Kelly komatiitic basalts analyzed exhibit a large range of absolute and relative lithophile trace element abundances and can be subdivided into three groups: HREE-depleted (179827, 179828: $Gd/Yb_N = 1.7–1.9$), HREE-enriched (179881, 179882, 179883: $Gd/Yb_N = 0.67–0.74$), and those that have near-chondritic HREE patterns (179884, 179885, 180220, 180221: $Gd/Yb_N = 1.1–1.2$). The HREE depleted basalts are also LREE-enriched ($La/Sm_N = 1.2–1.6$), whereas the HREE-enriched lavas are uniformly LREE-depleted ($La/Sm_N = 0.71–0.73$), and the lavas with the flat BSE-normalized HREE patterns have La/Sm_N ranging from 1.3 to 0.69. Despite the large range in the BSE-normalized LREE and HREE patterns, all Kelly komatiitic basalts have Nb/Nb* ratios that are close to unity (0.81–1.1). The W/Th ratios range from 0.11 to 1.4, i.e., they exhibit both relative depletions and enrichments in W (Table 2).

The seven Ruth Well komatiitic basalts analyzed in this study exhibit generally flat BSE-normalized LREE patterns ($La/Sm_N = 0.94–1.3$) and show uniform depletions in HREE ($Gd/Yb_N = 1.45 \pm 0.07$, 2SD). They also display negative Nb abundance anomalies that are identical in magnitude to those of the Ruth Well komatiites (Nb/Nb* = 0.52 ± 0.09, 2SD), but have significantly lower W/Th ratios compared to the Ruth Well komatiites (W/Th = 0.23–0.45).

The single analyzed basalt sample (176736) from the Regal Formation has a flat BSE-normalized REE pattern ($La/Sm_N = 0.97$, $Gd/Yb_N = 1.1$), exhibits a small negative Nb-anomaly (Nb/Nb* = 0.79) and a W/Th ratio of 0.65, which is also much closer to the BSE value than those of the Regal komatiites.

4.2. ^{147}Sm-^{143}Nd and ^{176}Lu-^{176}Hf isotope systematics

The Nd isotopic compositions and Sm and Nd abundances for the four Pilbara komatiite-basalt systems obtained in this study are presented in Table 3 and plotted on conventional Sm-Nd isochron diagrams in Fig. 5a–d. The Hf isotopic compositions and Lu and Hf abundances are presented in Table 4 and plotted on conventional Lu-Hf isochron diagrams in Fig. 6a–d.

4.2.1. Coonterunah

The six Coonterunah komatiite and komatiitic basalt samples and four replicates analyzed in this study (Table 3) yield an *Isoplot* (Ludwig, 2003) Model 1 solution isochron (MSWD = 1.3) with a slope corresponding to an age of 3530 ± 56 Ma (Fig. 5a) and an initial $^{143}Nd/^{144}Nd = 0.508169 \pm 69$ ($\varepsilon^{143}Nd(3530\ Ma) = +2.5 \pm 1.4$). This age agrees well with the accepted age of the Table Top Formation (Smithies et al., 2007). Averaging the initial $^{143}Nd/^{144}Nd$ ratios calculated for individual samples and assuming an emplacement age of 3530 Ma yields a more precise $\varepsilon^{143}Nd(3530\ Ma) = +2.4 \pm 0.5$ (2SD).

Hasenstab et al. (2021) presented Sm-Nd data for komatiite samples 176756 and 176757 that were also analyzed in this study. Their sample 179756 plots on the 3530 Ma isochron ($\varepsilon^{143}Nd(3530\ Ma) = +3.0$), whereas sample 179757 plots above the isochron ($\varepsilon^{143}Nd(3530\ Ma) = +5.6$, Fig. 5a). The source of the discrepancy for sample 179757 between the two studies is unclear; one possibility, as with many other Pilbara samples analyzed in previous studies for various isotopic systems, is that it was caused by LREE heterogeneity on a scale of drill core specimens, for example, related to the presence/absence of alteration veins, as we prepared powders for this study using new drill core material for all Pilbara samples.

The Lu-Hf isotopic data for the three Coonterunah komatiite samples analyzed in this study define an *Isoplot* Model 1 solution isochron (MSWD = 3.1) with an age of 3483 ± 87 Ma (Fig. 6a) and an $\varepsilon^{176}Hf(3483\ Ma) = +4.3 \pm 1.4$. This age agrees well with the Sm-Nd isochron

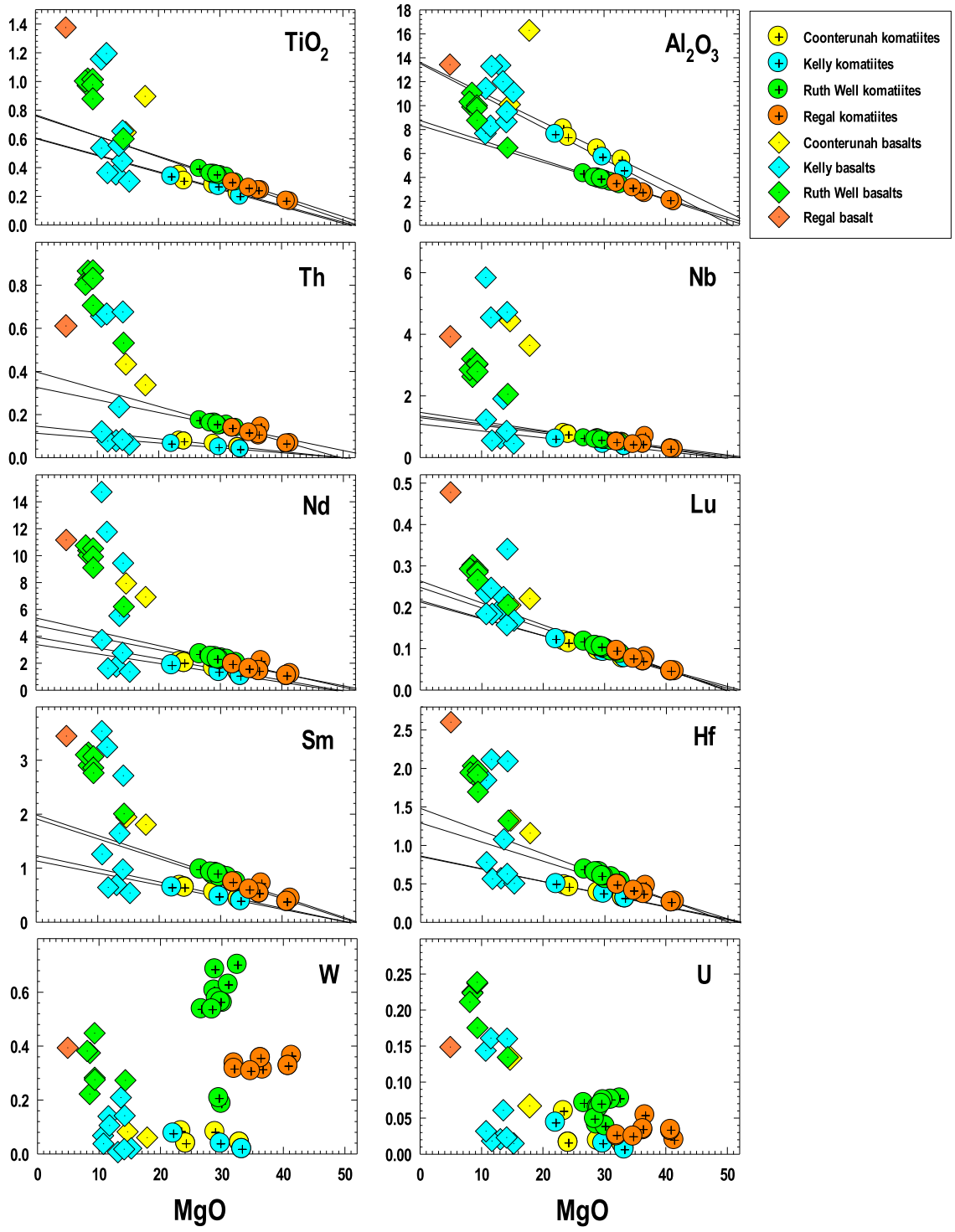

Fig. 3. Abundances of selected major- (wt.%) and lithophile trace elements and W (ppm) obtained in this study plotted against MgO contents (wt.%) in the four Pilbara komatiite-basalt systems. The regression lines were drawn through the data for the komatiites only. The W and U abundances plot with significant scatter and do not reveal any significant correlations. See text for additional details.

age for the Coonterunah komatiites obtained in this study. Averaging the initial $^{176}Hf/^{177}Hf$ values calculated for the individual samples, assuming the emplacement age of 3530 Ma and using the measured $^{176}Hf/^{177}Hf$ and $^{176}Lu/^{177}Hf$ ratios, yields a more precise $\varepsilon^{176}Hf(3530\ Ma) = +4.4 \pm 0.3$ (2SD).

Two of the komatiite samples analyzed in this study (179756 and 179757) were also analyzed by Nebel et al.

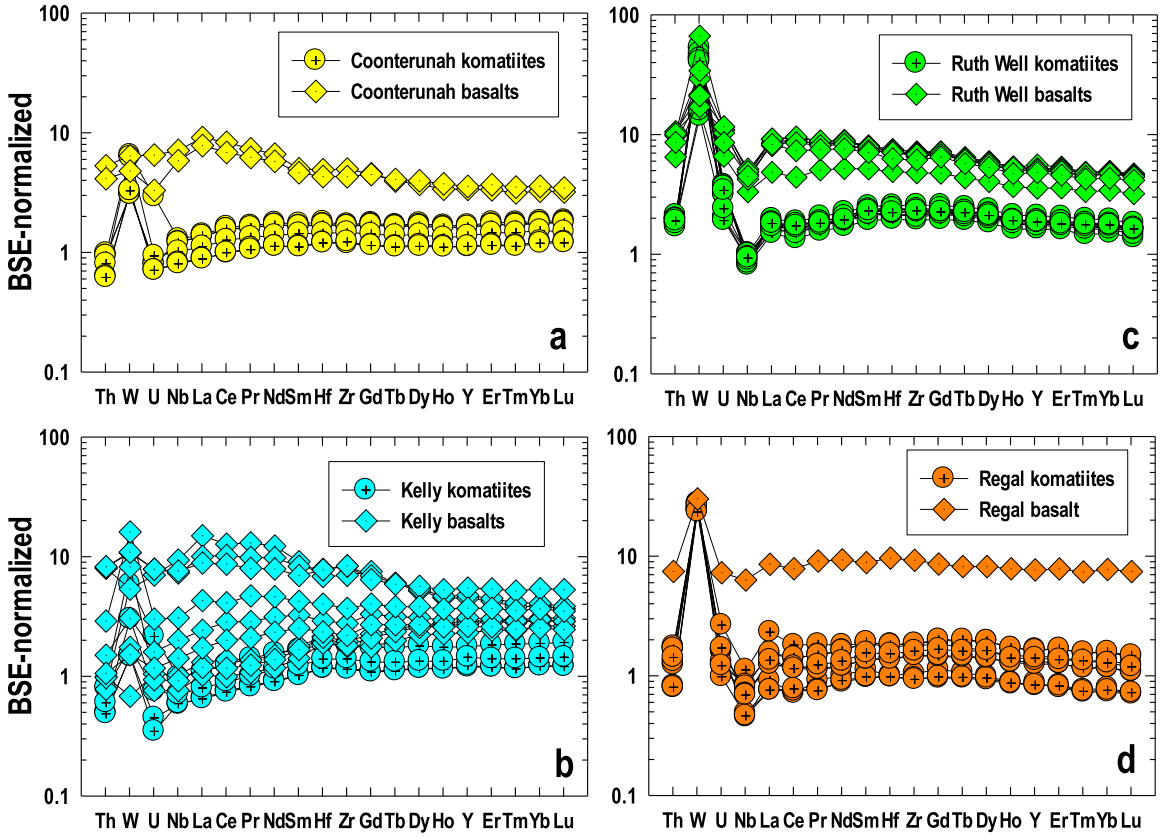

Fig. 4. BSE-normalized abundances of lithophile trace elements and W in the Pilbara komatiites and basalts plotted in the order of decreasing incompatibility during mantle melting. The normalizing values for W are from Arevalo and McDonough (2008) and for the rest of the elements, from Hofmann (1988).

(2014) and Hasenstab et al. (2021) for Lu-Hf isotope systematics. Although the data of Nebel et al. (2014) are nearly identical to our results and plot on the 3483 Ma isochron, the Hasenstab et al. (2021) data plot above the 3483 Ma isochron, possibly reflecting sample heterogeneity similar to sample 179757 described above (Fig. 6a). Nebel et al. (2014) also analyzed komatiitic basalt samples 179752 and 179812, which plot on or slightly below the 3483 Ma isochron (Fig. 6a). The average ε^{176}Hf(3530 Ma) = +4.7 ± 2.9 (2SD) for the two komatiite and two basalt samples analyzed by Nebel et al. (2014) is identical to the average ε^{176}Hf(3530 Ma) = +4.4 ± 0.3 (2SD) for the komatiites obtained in this study.

4.2.2. Kelly

Isoplot regression of the entire Sm-Nd data set for the twelve Kelly komatiite and komatiitic basalt samples analyzed in this study (Table 3) yields a Model 3 solution (MSWD = 2.2) isochron age of 3335 ± 53 Ma (Fig. 5b) and an ε^{143}Nd(3335 Ma) = +0.5 ± 1.4. This age is consistent with the accepted age of the Kelly Group (Smithies et al., 2007). Averaging the initial ε^{143}Nd values calculated for the individual samples using 3335 Ma as an emplacement age yields a more precise ε^{143}Nd(3335 Ma) = +0.5 ± 0.6 (2SD).

Hasenstab et al. (2021) analyzed seven samples from the Kelly Group, including a peridotite, two gabbros, one dolerite, two basalts, as well as one komatiite sample (179816) from this study. Their data, although plotting around the 3335 Ma isochron, show a significant amount of scatter (Fig. 5b); nonetheless, the average ε^{143}Nd (3335 Ma) of +0.9 ± 1.4 (2SD) calculated for all samples from the Hasenstab et al. (2021) study is similar to the average ε^{143}Nd(3335 Ma) = +0.5 ± 0.6 (2SD) obtained here.

The Lu-Hf isotopic data for the three Kelly komatiite samples analyzed in this study define an *Isoplot* Model 1 solution (MSWD = 2.2) isochron with an age of 3309 ± 45 Ma (Fig. 6b) and an ε^{176}Hf(3309 Ma) = +1.7 ± 1.0. This age agrees well with the Sm-Nd isochron age obtained in this study. Averaging the initial ε^{176}Hf values calculated for the individual samples using 3335 Ma as an emplacement age of the lavas yields a more precise ε^{176}Hf (3335 Ma) = +1.7 ± 0.6 (2SD).

Nebel et al. (2014) analyzed five samples of Kelly komatiitic basalts, which were not analyzed in this study, for the Lu-Hf systematics (Fig. 6b); their data plot on or slightly above the 3309 Ma isochron, with an average ε^{176}Hf(3335 Ma) = +5.0 ± 3.8 (2SD).

More recently, Hasenstab et al. (2021) published Lu-Hf isotope data for eight samples of Kelly komatiites, basalts,

Table 3
Sm-Nd isotopic compositions of the Pilbara komatiites and basalts.

Sample	Sm, ppm	Nd, ppm	$^{147}Sm/^{144}Nd$	$^{143}Nd/^{144}Nd$	$\varepsilon^{143}Nd(T)$
Coonterunah					
179751	0.6880	2.184	0.1905	0.512610 ± 4	+2.3
Replicate	0.6815	2.177	0.1893	0.512583 ± 4	+2.3
179755	0.6564	2.056	0.1930	0.512689 ± 5	+2.7
Replicate	0.6796	2.131	0.1929	0.512693 ± 4	+2.9
179756	0.5444	1.677	0.1963	0.512740 ± 4	+2.2
Replicate	0.5472	1.682	0.1967	0.512742 ± 4	+2.1
179757	0.4496	1.392	0.1953	0.512740 ± 4	+2.7
Replicate	0.4732	1.443	0.1982	0.512795 ± 4	+2.4
179752	1.970	7.973	0.1493	0.511652 ± 4	+2.4
179812	1.826	6.896	0.1601	0.511911 ± 4	+2.5
Kelly					
176773	0.6722	1.945	0.2090	0.512952 ± 4	+0.83
179815	0.3997	1.071	0.2256	0.513305 ± 5	+0.56
179816	0.4871	1.379	0.2135	0.513039 ± 5	+0.62
179827	3.597	14.86	0.1463	0.511561 ± 5	+0.68
179828	3.228	11.38	0.1715	0.512123 ± 4	+0.80
179881	0.7456	1.890	0.2385	0.513562 ± 4	+0.05
179882	0.5708	1.433	0.2408	0.513645 ± 6	+0.68
179883	0.6755	1.680	0.2431	0.513683 ± 4	+0.42
179884	1.309	3.853	0.2054	0.512865 ± 4	+0.69
179885	1.015	2.858	0.2147	0.513080 ± 3	+0.89
180220	2.778	9.555	0.1757	0.512178 ± 6	+0.05
180221	1.677	5.573	0.1819	0.512316 ± 4	+0.08
Ruth Well					
137638	0.8900	2.543	0.2116	0.513032 ± 4	+1.6
138239	0.8514	2.277	0.2261	0.513275 ± 3	+0.39
140258	0.8622	2.207	0.2362	0.513485 ± 3	+0.38
Replicate	0.8687	2.218	0.2368	0.513497 ± 5	+0.36
158691a	0.8990	2.404	0.2261	0.513275 ± 4	+0.42
158692b	0.9353	2.505	0.2258	0.513276 ± 3	+0.56
158693	0.8610	2.336	0.2228	0.513207 ± 4	+0.43
158694	0.9181	2.455	0.2261	0.513283 ± 4	+0.58
137314	3.138	10.76	0.1764	0.512250 ± 3	+0.74
137636	2.953	9.906	0.1802	0.512316 ± 4	+0.46
137644	2.822	9.150	0.1864	0.512425 ± 4	+0.03
137644 Cpx	0.8363	2.700	0.1872	0.512478 ± 4	+0.74
137644 Pl	0.1845	0.8665	0.1343	0.511354 ± 11	+0.47
140259	2.075	6.448	0.1945	0.512624 ± 3	+0.61
Replicate	2.074	6.446	0.1946	0.512626 ± 5	+0.65
Regal					
176720	0.7366	2.264	0.1967	0.512696 ± 4	+1.1
176721	0.4345	1.190	0.2208	0.513205 ± 4	+1.2
176722	0.3914	1.032	0.2292	0.513374 ± 4	+1.0
Replicate	0.3908	1.028	0.2298	0.513390 ± 4	+1.1
176723	0.7006	1.882	0.2251	0.513276 ± 3	+0.82
Replicate	0.7031	1.890	0.2249	0.513280 ± 4	+0.97
176724	0.5223	1.435	0.2201	0.513200 ± 4	+1.4
176725	0.5885	1.580	0.2252	0.513293 ± 4	+1.1
Replicate	0.5849	1.569	0.2255	0.513293 ± 4	+1.0
176736	3.440	10.73	0.1939	0.512630 ± 4	+1.0
USGS GRM BCR-1					
This study_1	6.620	28.70	0.13947	0.512648 ± 3	
This study_2	6.689	29.00	0.13944	0.512650 ± 3	
This study_3	6.621	28.71	0.13942	0.512654 ± 3	
This study_4	6.619	28.69	0.13948	0.512646 ± 4	
This study_5	6.608	28.67	0.13937	0.512654 ± 3	
This study_6	6.620	28.73	0.13929	0.512650 ± 4	
Average	6.630 ± 0.024	28.75 ± 0.10	0.1394 ± 0.0001	0.512650 ± 3	

GeoRem	6.603 ± 0.022	28.68 ± 0.10	0.1392 ± 0.0009	0.51262 ± 0.00012
USGS GRM BIR-1				
This study	1.099	2.360	0.2815	0.513100 ± 4
GeoRem	1.113 ± 0.018	2.397 ± 0.043	0.2807 ± 0.0007	0.513091 ± 14

Initial ε^{143}Nd values were calculated for the emplacement ages of T = 3530 Ma (Coonterunah), 3335 Ma (Kelly), 3171 Ma (Ruth Well), and 3176 Ma (Regal) defined by the respective Sm-Nd isochrons. The Sm and Nd concentrations were recalculated on an anhydrous basis using the LOI values from Table 1.

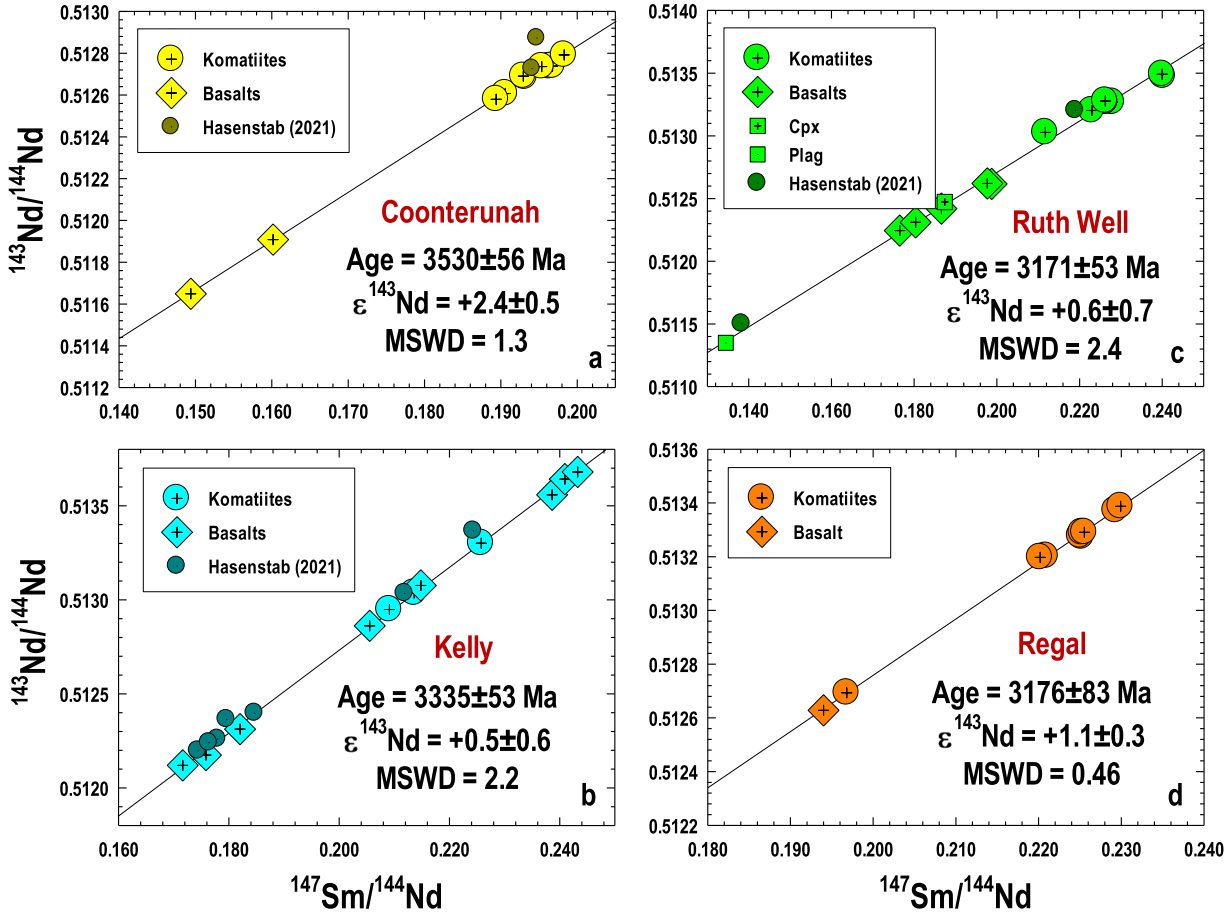

Fig. 5. Sm-Nd isochron diagrams for the four Pilbara komatiite-basalt systems. The data from the Hasenstab et al. (2021) study for the respective komatiite-basalt systems are plotted for comparison.

gabbros, a peridotite, and a dolerite. Those data essentially straddle the 3309 Ma isochron obtained in this study (Fig. 6b); the average ε^{176}Hf(3335 Ma) for their samples is +3.5 ± 4.2 (2SD).

4.2.3. Ruth Well

A total of fifteen samples, including seven komatiites (plus one replicate), four komatiitic basalts (plus one replicate) and clinopyroxene and plagioclase separates from the basaltic sample 137644 were analyzed in this study. Regression of the data using *Isoplot* (Ludwig, 2003) yields a Model 3 solution (MSWD = 2.4) isochron with an age of 3171 ± 53 Ma (Fig. 5c) and an ε^{143}Nd(3171 Ma) = +0.6 ± 1.4. This isochron age is consistent, within the uncertainty, with the accepted age of the Ruth Well Formation (Smithies et al., 2007). Averaging the initial ε^{143}Nd values calculated for the individual samples yields a more precise ε^{143}Nd(3171 Ma) of +0.6 ± 0.7 (2SD).

Arndt et al. (2001) reported Sm-Nd data for one Ruth Well komatiite and one basalt sample (neither of which were analyzed in this study), which plot on the 3171 Ma isochron, having the initial ε^{143}Nd values of +0.8 and +0.5; these values are identical to the average ε^{143}Nd(3171 Ma) value obtained in this study. Two other Ruth Well komatiite samples analyzed by Hasenstab et al. (2021), which were also not analyzed in this study, plot above the 3171 Ma isochron (Fig. 5c; ε^{143}Nd(3171 Ma) = +1.9 and +2.1).

Table 4
Lu-Hf isotopic compositions of the Pilbara komatiites and basalts.

Sample	Lu, ppm	Hf, ppm	$^{176}Lu/^{177}Hf$	$^{176}Hf/^{177}Hf$	$\varepsilon^{176}Hf(T)$
Coonterunah					
179751	0.1165	0.5748	0.02872	0.282576 ± 3	+4.4
179756	0.1023	0.4366	0.03320	0.282875 ± 4	+4.2
179757	0.07957	0.3547	0.03180	0.282788 ± 4	+4.5
Kelly					
176773	0.1025	0.4993	0.02911	0.282546 ± 4	+1.8
179815	0.08247	0.2626	0.04452	0.283524 ± 13	+1.4
179816	0.1011	0.4079	0.03512	0.282937 ± 9	+1.9
Ruth Well					
138239	0.1012	0.6168	0.02326	0.282204 ± 3	+1.8
140258	0.09975	0.6433	0.02198	0.282130 ± 3	+1.9
158692b	0.1122	0.6535	0.02433	0.282267 ± 4	+1.7
137314	0.3008	1.9146	0.02227	0.282139 ± 3	+1.6
137636	0.2952	1.8522	0.02259	0.282158 ± 3	+1.6
137644	0.2657	1.6443	0.02290	0.282182 ± 3	+1.7
Regal					
176720	0.08360	0.4802	0.02468	0.282354 ± 4	+4.1
176724	0.07121	0.3611	0.02795	0.282552 ± 7	+4.0
176736	0.4879	2.580	0.02680	0.282493 ± 3	+4.4
USGS GRM BCR-1					
This study	0.4980	4.949	0.01426	0.282872 ± 4	
GeoRem	0.499 ± 0.005	4.92 ± 0.06		0.282867 ± 15	

Initial $\varepsilon^{176}Hf$ values were calculated for the emplacement ages of $T = 3530$ Ma (Coonterunah), 3335 Ma (Kelly), 3171 Ma (Ruth Well), and 3176 Ma (Regal) defined by the respective Sm-Nd isochrons. The Lu and Hf concentrations were recalculated on an anhydrous basis using the LOI values from Table 1.

The Lu-Hf isotopic data for the three komatiite and three komatiitic basalt samples analyzed in this study yield an *Isoplot* Model 1 solution (MSWD = 0.79) isochron age of 3142 ± 210 Ma (Fig. 6c) and an $\varepsilon^{176}Hf(3142\ Ma) = +1.5 \pm 3.5$. This age is in agreement with the Sm-Nd isochron age of 3171 ± 53 Ma obtained in this study. The large uncertainties on the Lu-Hf age and the initial $\varepsilon^{176}Hf$ value are due to a very limited spread in the Lu/Hf ratio among the samples analyzed. Averaging the initial $^{176}Hf/^{177}Hf$ values calculated for the individual samples assuming the emplacement age of 3171 Ma and using the measured $^{176}Hf/^{177}Hf$ and $^{176}Lu/^{177}Hf$ ratios yields a more precise $\varepsilon^{176}Hf(3171\ Ma) = +1.7 \pm 0.2$ (2SD).

Nebel et al. (2014) presented Lu-Hf data for one Ruth Well basaltic sample; the single datum plots on the 3142 Ma isochron obtained in this study (Fig. 6c). Hasenstab et al. (2021) analyzed three komatiite samples (Fig. 6c); none of these samples were analyzed in this study. While the datum for one komatiite sample plots on the 3142 Ma isochron, the data for the other two samples do not. Their calculated average $\varepsilon^{176}Hf(3171\ Ma) = +4.0 \pm 2.4$ (2SD), however, is similar, within uncertainties, to the average $\varepsilon^{176}Hf(3171\ Ma) = +1.7 \pm 0.2$ (2SD) obtained in this study.

4.2.4. Regal

A total of nine komatiite samples (including 3 replicates) and one basalt sample (Table 3) have been analyzed for the Sm-Nd systematics (Fig. 5d). Regression of the data using *Isoplot* yielded a Model 1 solution (MSWD = 0.46) isochron with an age of 3176 ± 83 Ma and an $\varepsilon^{143}Nd(3176\ Ma) = +1.0 \pm 2.4$. This isochron age is consistent, within the uncertainty, with the accepted age of the Regal Formation (Smithies et al., 2007). Averaging the initial $\varepsilon^{143}Nd$ values calculated for the individual samples yields a more precise $\varepsilon^{143}Nd(3176\ Ma) = +1.1 \pm 0.3$ (2SD).

The Lu-Hf isotopic data for the two komatiite and one basalt samples define an *Isoplot* Model 1 solution (MSWD = 2.8) isochron with an age of 3213 ± 200 Ma (Fig. 6d) and an $\varepsilon^{176}Hf(3213\ Ma) = +4.4 \pm 3.6$. This age is in agreement with the Sm-Nd isochron age of 3176 ± 83 Ma, as well as with the accepted age of the Regal Formation. As with the other three komatiite-basalt systems, the large uncertainty on the age and the initial $\varepsilon^{176}Hf$ are due to the limited spread in the Lu/Hf ratios of the samples analyzed. Averaging the initial $^{176}Hf/^{177}Hf$ values calculated for the three individual samples and using the measured $^{176}Hf/^{177}Hf$ and $^{176}Lu/^{177}Hf$ ratios yields a more precise $\varepsilon^{176}Hf(3176\ Ma) = +4.1 \pm 0.4$ (2SD).

Nebel et al. (2014) published Lu-Hf data for four Regal komatiite samples, including one sample that was also analyzed in this study (176720). Their data plot on or close to the 3213 Ma isochron from this study (Fig. 6d); the average $\varepsilon^{176}Hf(3176\ Ma) = +4.6 \pm 2.1$ (2SD) calculated for their four data points is identical to the average $\varepsilon^{176}Hf(3176\ Ma) = +4.1 \pm 0.4$ (2SD) from this study.

4.3. $^{187}Os/^{188}Os$ isotopic systematics and HSE abundances

The Re-Os isotopic and HSE abundance data for the Pilbara komatiites and basalts are listed in Table 5. The data are also plotted on Re-Os isochron diagrams in Fig. 7a–d, in MgO versus HSE variation diagrams in Fig. 8, and as BSE-normalized abundances in Fig. 9a–d.

The Re-Os isotopic data for the four Coonterunah komatiite (plus four replicates) and two komatiitic basalt samples (not shown) plot with a significant scatter in the Re-Os diagram (Fig. 7a) and do not exhibit an isochronous relationship. The calculated $\gamma^{187}Os$(3530 Ma) values range between +5 and +103 for the komatiites and +163 and +214 for the basalts. This type of irregular behavior is most likely due to the variable loss of Re, typical of altered mafic–ultramafic lavas (e.g., Dale et al., 2007) that occurred several hundred Ma after lava emplacement, possibly during one of the late Archean tectono-metamorphic events that affected this area (Smithies et al., 2007). Therefore, no useful information regarding the initial Os isotopic composition of the source of the lavas can be gleaned from these data.

The Re-Os isotopic data for the three samples of the Kelly komatiites (plus three replicates) yield an *Isoplot* Model 3 solution (MSWD = 5.1) isochron with an age of 3387 ± 210 Ma and a $\gamma^{187}Os$(3387 Ma) = +1.1 ± 0.5 (Fig. 7b). This age is in agreement with the Sm-Nd and Lu-Hf ages obtained for the Kelly komatiites and basalts in this study. The large uncertainty on the age is attributed to the very limited variation in the $^{187}Re/^{188}Os$ ratios (0.034–0.20) among the komatiite samples. Averaging the initial Os isotopic compositions for the individual samples recalculated for the time of the Kelly lavas formation defined by the Sm-Nd isochron (3335 Ma) results in a slightly more precise $\gamma^{187}Os$(3335 Ma) = +0.8 ± 0.4 (2SD). The three Kelly komatiitic basalt samples analyzed (not shown in Fig. 7b) have high $^{187}Re/^{188}Os$ ratios (26.1–30.2) and highly variable calculated $\gamma^{187}Os$(3335 Ma) ranging from –102 to +770, likely due to open system behavior that resulted in addition/removal of Re several hundred Ma after the lava emplacement.

The Re-Os isotopic data for the eleven Ruth Well komatiite samples and two chromite separates plot with a significant scatter and define a regression line with a slope corresponding to a Model 3 solution (MSWD = 101) age of 3049 ± 110 Ma and a $\gamma^{187}Os$(3049 Ma) = –1.1 ± 1.4 (Fig. 7c). This Re-Os age, although 120 Ma younger, is within the uncertainty of the Sm-Nd age obtained for the Ruth Well system in this study. Four komatiitic basalt samples and one replicate analyzed plot off the regression line,

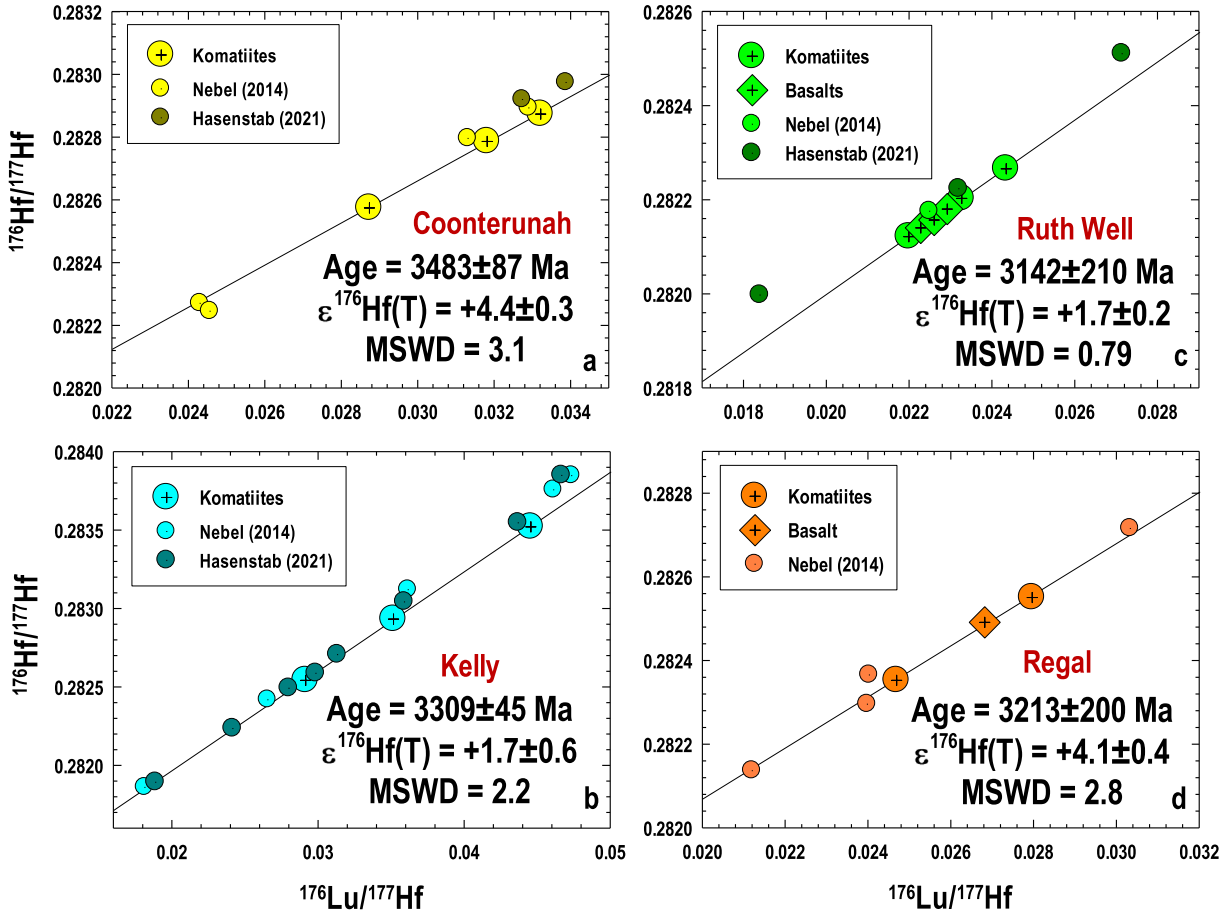

Fig. 6. Lu-Hf isochron diagrams for the four Pilbara komatiite-basalt systems. The data from the Nebel et al. (2014) and Hasenstab et al. (2021) studies for the respective komatiite-basalt systems are plotted for comparison.

Table 5
Highly siderophile element abundances (in ppb) and Re-Os isotopic data for the Pilbara komatiites and basalts.

Sample No.	Re	Os	Ir	Ru	Pt	Pd	$^{187}Re/^{188}Os$	$^{187}Os/^{188}Os$	$\gamma^{187}Os(T)$
Coonterunah									
179751	0.0518	1.480	1.03	3.01	4.53	4.48	0.1705 ± 0.0025	0.21657 ± 10	+101
Replicate	0.0433	1.450	1.01	2.87	4.07	4.77	0.1456 ± 0.0026	0.21689 ± 10	+103
179755	0.0281	0.9828	1.09	2.84	4.15	4.38	0.1387 ± 0.0039	0.16832 ± 07	+56
Replicate	0.0260	0.8532	0.858	2.82	3.78	4.49	0.1475 ± 0.0043	0.17893 ± 08	+66
179756	0.0119	1.511	1.32	4.05	3.48	3.75	0.0379 ± 0.0026	0.11013 ± 06	+5.0
Replicate	0.00943	3.320	1.86	4.11	3.41	3.66	0.0137 ± 0.0011	0.11735 ± 06	+13
179757	0.0118	1.319	1.08	4.69	3.07	2.99	0.0429 ± 0.0028	0.11819 ± 06	+13
Replicate	0.00766	1.264	1.22	4.61	2.90	3.08	0.0292 ± 0.0029	0.11893 ± 05	+14
179752	0.0313	0.4029	0.490	1.48	5.60	6.17	0.3823 ± 0.0084	0.29330 ± 17	+163
179812	0.0594	0.06939	0.0635	0.327	5.02	5.65	4.369 ± 0.065	0.58689 ± 37	+214
Kelly									
176773	0.0373	1.204	1.13	2.74	5.96	5.85	0.1492 ± 0.0030	0.11370 ± 07	+1.1
Replicate	0.0379	1.194	1.11	2.73	5.74	5.64	0.1526 ± 0.0036	0.11365 ± 06	+0.84
179815	0.0327	1.527	1.29	3.34	3.87	3.58	0.1028 ± 0.0024	0.11086 ± 06	+0.89
Replicate	0.0971	2.310	1.19	3.25	3.71	3.36	0.2023 ± 0.0017	0.11635 ± 05	+0.71
179816	0.0104	1.469	1.14	3.10	4.57	4.57	0.0341 ± 0.0023	0.10685 ± 06	+0.81
Replicate	0.0120	1.322	1.06	3.01	4.30	4.45	0.0436 ± 0.0026	0.10709 ± 04	+0.53
179881	0.713	0.1564	0.260	0.644	10.9	12.5	26.05 ± 0.16	1.5594 ± 09	–32
179882	0.337	0.07300	0.170	0.235	10.9	11.5	29.28 ± 0.18	2.5779 ± 22	+770
180221	1.58	0.3054	0.342	1.57	7.24	7.44	30.20 ± 0.18	1.7233 ± 09	–102
Ruth Well									
137638	0.240	2.209	2.12	4.50	6.76	5.74	0.5242 ± 0.0031	0.13394 ± 06	+0.28
138239	0.221	2.073	1.91	4.10	6.98	5.96	0.5137 ± 0.0031	0.13059 ± 08	–2.4
138308	0.0445	1.843	1.79	4.98	7.78	6.64	0.1161 ± 0.0023	0.11172 ± 05	+0.20
140258	0.300	2.300	2.04	4.43	6.83	5.76	0.6287 ± 0.0038	0.13508 ± 07	–4.0
158691a	0.539	2.080	1.93	4.41	7.26	5.95	1.256 ± 0.007	0.17080 ± 07	–2.4
158691b	0.570	1.995	1.83	4.46	6.64	5.81	1.385 ± 0.008	0.17671 ± 07	–3.5
158692a	0.277	1.775	1.70	4.17	5.97	4.95	0.7535 ± 0.0045	0.14604 ± 08	–0.05
158692b	0.404	2.236	2.10	4.62	7.25	6.06	0.8721 ± 0.0052	0.15024 ± 10	–2.2
158692c	0.318	2.109	1.90	4.48	6.43	5.47	0.7282 ± 0.0044	0.14309 ± 02	–1.6
158693	0.391	2.347	2.16	4.63	6.99	5.87	0.8038 ± 0.0048	0.14654 ± 01	–2.2
158694	0.205	2.247	2.12	4.32	7.31	6.26	0.4397 ± 0.0026	0.12781 ± 02	–1.2
137314	0.0810	0.07366	0.268	0.600	6.96	6.98	5.704 ± 0.064	0.71360 ± 46	+284
137636	0.141	0.08278	0.231	0.522	5.36	6.81	8.821 ± 0.067	0.72358 ± 48	+133
137644	0.122	0.1197	0.222	0.645	4.69	5.10	5.057 ± 0.040	0.35090 ± 25	–27
Replicate	0.0988	0.1400	0.263	0.702	4.93	6.18	3.479 ± 0.030	0.30458 ± 19	+10
140259	0.343	0.1530	0.255	0.848	3.64	4.82	11.61 ± 0.07	0.69987 ± 42	–33
138239 Chr	0.577	42.59					0.0651 ± 0.0025	0.10835 ± 05	–0.38
137644 Chr	2.51	1.823					6.93 ± 0.82	0.48059 ± 55	–0.27
Regal									
176720	0.0800	1.322	1.62	6.90	6.18	4.94	0.2921 ± 0.0018	0.13879 ± 08	+17
176721	0.0136	5.162	4.24	3.47	4.30	3.43	0.0127 ± 0.0008	0.10695 ± 04	+1.0
Replicate	0.0135	5.044	4.04	3.50	4.20	3.39	0.0129 ± 0.0007	0.10712 ± 01	+1.2
176722	0.0239	6.139	5.31	4.78	4.58	3.70	0.0187 ± 0.0006	0.10726 ± 05	+1.0
Replicate	0.0195	6.216	5.64	4.78	4.69	3.79	0.0151 ± 0.0007	0.10717 ± 02	+1.1
176723	0.204	3.105	2.47	3.61	8.06	6.33	0.3166 ± 0.0013	0.12327 ± 05	+0.84
Replicate	0.203	3.132	3.14	3.73	7.87	6.44	0.3120 ± 0.0014	0.12310 ± 01	+0.92
176724	0.0980	4.366	3.63	4.77	6.44	5.25	0.1079 ± 0.0009	0.11189 ± 05	+0.80
Replicate	0.163	5.624	3.87	4.88	6.50	5.38	0.1397 ± 0.0008	0.11356 ± 01	+0.76
176725	0.0123	2.547	2.40	4.62	6.86	5.76	0.0232 ± 0.0015	0.10734 ± 05	+0.86
Replicate	0.0131	2.682	2.50	4.57	6.79	5.55	0.0235 ± 0.0016	0.10732 ± 01	+0.82

HSE abundances recalculated on an anhydrous basis. The initial $\gamma^{187}Os$ values were calculated for the emplacement ages $T = 3530$ Ma (Coonterunah), 3335 Ma (Kelly), 3171 Ma (Ruth Well), and 3176 Ma (Regal) defined by the respective Sm-Nd isochrons. *Replicate* – replicate digestion and analysis of the same sample.

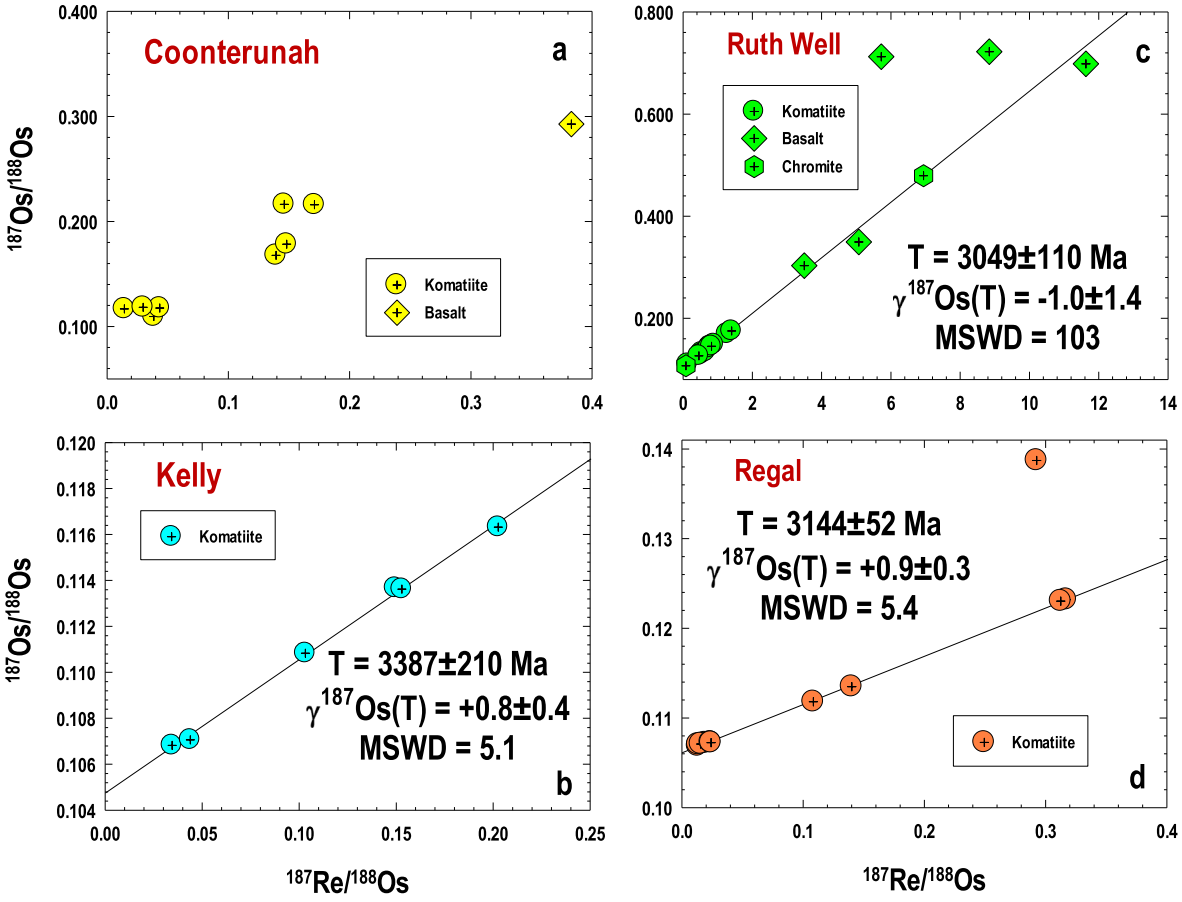

Fig. 7. Re-Os diagrams for the four Pilbara komatiite-basalt systems. The Coonterunah data (a) plot with a scatter and do not define any isochronous relationships. For the Ruth Well komatiite system (c), the komatiite data, for which (and the chromite separates) the isochron regression calculations were performed, plot with a significant scatter greatly exceeding the analytical uncertainty (MSWD = 101). The data for the komatiitic basalts plot with an even greater scatter and were excluded from the *Isoplot* regression calculations. For the Regal komatiite system (d), one sample plots well off the isochron; the data for this sample were also excluded from the *Isoplot* regression calculations.

with γ^{187}Os(3171 Ma) values ranging from –33 to + 284, which is likely the result of late postmagmatic Re mobility.

Meisel et al. (2001a,b) reported Re-Os isotopic data for two komatiite samples (not analyzed in this study) plus two replicates; these have an average γ^{187}Os(3171 Ma) = –0.8 ± 1.1, which is identical, within the uncertainties, to the γ^{187}Os(3171 Ma) = –1.1 ± 1.4 obtained in this study.

Given the significant scatter of the komatiite samples around the regression line (MSWD = 101), and the fact that it defines an age that is ~120 Ma younger than the emplacement age of the lavas, it is likely that their Re-Os isotopic systematics have also been somewhat disturbed by postmagmatic processes, although to a much lesser extent than that of the komatiitic basalts. Chromite separates, however, likely preserved the original Os isotopic signatures of their host lavas, as has been shown to be the case in previous studies (e.g., Gangopadhyay et al., 2006). Therefore, the Os isotopic composition of the Ruth Well komatiites and basalts is best represented by the two chromite separates analyzed in this study. *Isoplot* regression yields a two-point Model 1 solution "isochron" with an age of 3172 ± 360 Ma corresponding to a γ^{187}Os(3171 Ma) = –0.4 ± 0.4.

The Re-Os isotopic data for the six samples of the Regal komatiites, plus five replicates, yield an *Isoplot* Model 3 solution (MSWD = 5.4) isochron with an age of 3144 ± 52 Ma and a γ^{187}Os(3144 Ma) = +0.7 ± 0.1 (Fig. 7d). This age is in agreement with the Sm-Nd and Lu-Hf isochron ages obtained in this study. Recalculating the initial γ^{187}Os for each sample using the emplacement age of 3176 Ma yields a more accurate average γ^{187}Os(3176 Ma) = +0.9 ± 0.3 (2SD).

The Os, Ir, and Ru abundances (referred to as the iridium-group PGE, or IPGE, following Barnes et al., 1985) plot with a significant scatter in the MgO variation diagrams (Fig. 8). The komatiitic basalts have low concentrations of the IPGE, with the Os abundances ranging between 0.07–0.40, 0.07–0.30, and 0.07–0.15 ppb in the Coonterunah, Kelly, and Ruth Well lavas, respectively, and exhibit little correlation with the age or the MgO content of the lavas. In the komatiites, the Os concentrations range between 0.85–3.3 ppb (Coonterunah), 1.2–2.3 ppb (Kelly), 1.6–2.2 ppb (Ruth Well), and 1.3–6.2 ppb (Regal). The IPGE abundances show a broad increase with increasing the MgO contents in the Coonterunah, Kelly, and Regal lavas, whereas in the Ruth Well lavas, there is a neg-

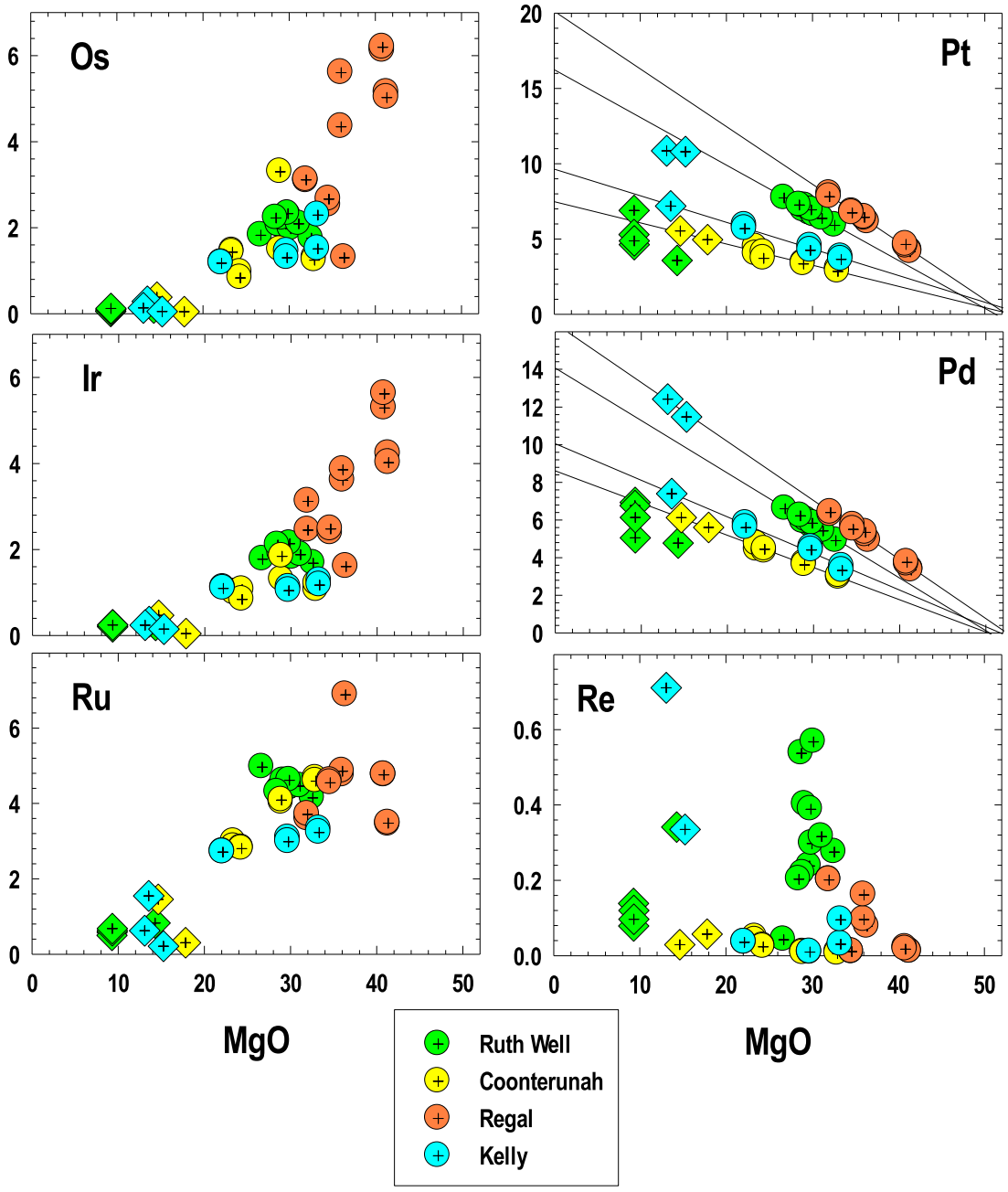

Fig. 8. Abundances of the HSE in the four Pilbara komatiite-basalt systems (ppb) obtained in this study plotted against MgO contents (wt.%).

ative correlation between MgO and the IPGE abundances. These types of variations indicate a combined control of olivine and Os-Ir-Ru-rich alloy (e.g., Barnes and Fiorentini, 2008) during lava differentiation in the Coonterunah, Kelly, and Regal lavas, and olivine control only in the Ruth Well lavas.

The Pt and Pd abundances (referred to as the platinum-group PGE, or PPGE, after Barnes et al., 1985) in the komatiites follow well-constrained linear trends with negative slopes that coincide with olivine control lines (Fig. 8). These data indicate (1) immobile behavior of the PPGE during seafloor alteration and metamorphism of the four komatiite systems, (2) that olivine was the only major fractionating phase that controlled the behavior of Pt and Pd during differentiation of the lavas, and (3) that all four komatiite systems were sulfide-undersaturated upon emplacement. Finally, the Re abundances plot with a large scatter in Fig. 8 and do not show any significant correlation with the MgO content, likely due to the Re mobility after the lava emplacements noted earlier. Based on the Re-Os

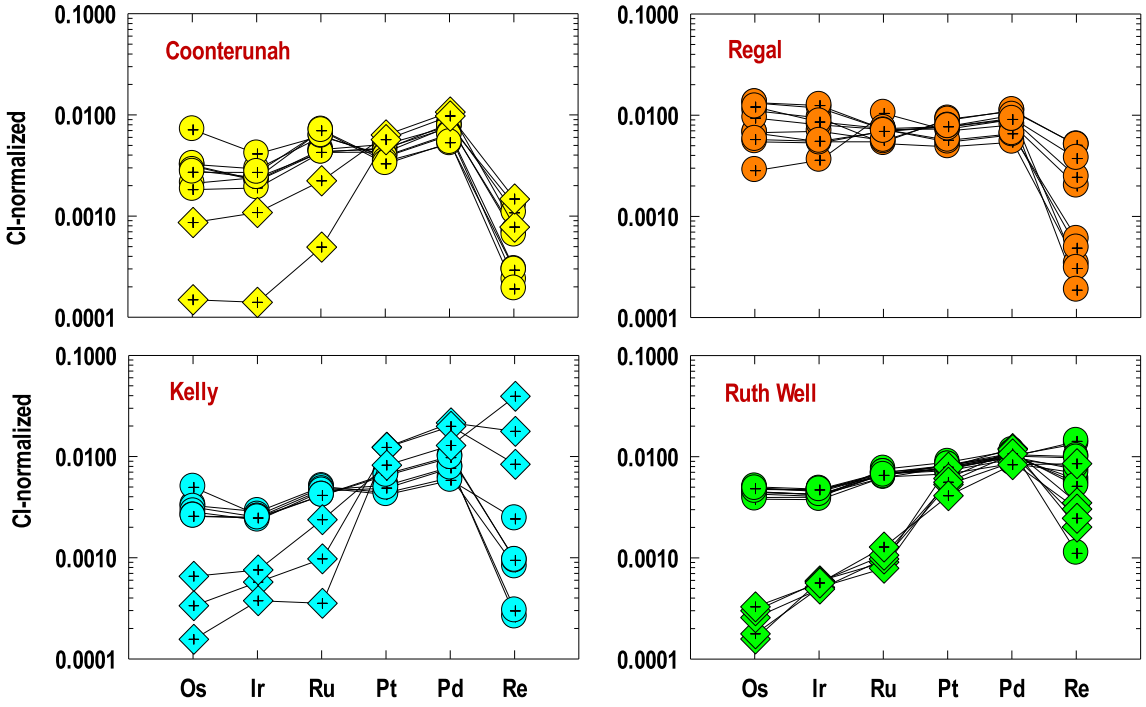

Fig. 9. CI chondrite-normalized HSE abundances in whole-rock samples from the four Pilbara komatiite-basalt systems analyzed in this study. Normalizing values are from Horan et al. (2003).

isotopic data, this Re mobilization likely took place either shortly after lava emplacement, in the case of Kelly and Regal systems, or was delayed for several hundred Ma, in the case of the Coonterunah and Ruth Well komatiite systems.

The Pt and Pd abundance data for the two samples of the Coonterunah komatiitic basalts plot on the same olivine control lines with the komatiites, indicating that their HSE abundances are likely related by simple olivine fractionation. Out of the three Kelly komatiitic basalt samples analyzed, only sample 180221 plots on the same olivine control line with the Kelly komatiites, also indicating that their HSE abundances are related by olivine fractionation, whereas the other two samples (179881 and 179882) plot well above the respective olivine control lines. This may be due to their derivation from a different parental liquid or to small amounts of base sulfide liquid accumulation. Finally, all Ruth Well komatiitic basalt samples plot well below the Ruth Well komatiitic liquid lines of descent, likely also indicating a different magmatic history for the HSE compared to the komatiites.

In the CI-normalized HSE abundance plots (Fig. 9), the komatiites display moderately fractionated HSE patterns, with modest enrichments to slight depletions in PPGE relative to IPGE (Pd/Ir_N = 1.5–4.1, 2.2–4.0, 2.1–2.9, and 0.53–2.4 in the Coonterunah, Kelly, Ruth Well, and Regal komatiite systems, respectively). In contrast to the komatiites, the komatiitic basalts display strongly fractionated HSE patterns, with strong enrichments in PPGE relative to IPGE (Pd/Ir_N = 9.8–69, 17–53, and 15–23 in the Coonterunah, Kelly, and Ruth Well lavas, respectively).

Maier et al. (2009) reported Os, Ir, Ru, Pt, and Pd abundances for four komatiite samples (179751, 179755, 179756, and 179757), which were also analyzed in this study, albeit using different sample material, as previously noted. The concentrations obtained in the Maier et al. (2009) study are from 2% higher to 4% lower for Os and from 3% higher to 6% lower for Ir, whereas Ru, Pt, and Pd abundances are up to 18%, 22%, and 48% lower, respectively. In addition, their data plot with significant scatter on the MgO versus HSE diagrams, especially for Pt and Pd. The source of this discrepancy is not clear, but could be the result of variable, uncontrolled HSE losses during the unspiked digestion and chemical separation procedures in the Maier et al. (2009) study.

4.4. $^{182}W/^{184}W$ isotopic compositions

A total of twenty nine samples, including one replicate, have been analyzed for W isotopic composition; the data are listed in Table 6 and plotted in Fig. 10 as part per million (ppm) deviations of $^{182}W/^{184}W$ ($\mu^{182}W$) and $^{183}W/^{184}W$ ($\mu^{183}W$) from average values for these ratios measured in the *Alfa Aesar* W standard that is assumed to represents the W isotopic composition of the modern BSE (e.g., Kleine et al. (2004b)). All four komatiite-basalt systems exhibit resolvable positive ^{182}W anomalies of +11.4 ± 4.6, +8.2 ± 3.3, +8.3 ± 4.5, and +11.8 ± 4.8 ppm (2SD) for the Coonterunah, Kelly, Ruth Well, and Regal systems, respectively.

Archer et al. (2019) analyzed one komatiite and one andesite sample (plus a replicate) from Ruth Well and

Table 6
W isotopic compositions and W abundances of the Pilbara komatiites and basalts.

Sample No.	Lithology	$\mu^{182}W$ (6/3)	$\mu^{183}W$ (6/3)	W/Th
Coonterunah				
179751	Komatiite	+15.4 ± 2.8	+0.9 ± 2.2	1.06
179755	Komatiite	+9.8 ± 5.5	–0.9 ± 4.5	0.522
179756	Komatiite	+10.9 ± 3.7	+2.8 ± 3.0	1.24
179757	Komatiite	+12.5 ± 2.3	–0.1 ± 1.8	0.828
179752	Komatiitic basalt	+10.2 ± 3.7	+1.7 ± 2.9	0.193
179812	Komatiitic basalt	+9.3 ± 3.3	–3.5 ± 2.4	0.185
Average (±2SD)		**+11.4 ± 4.6**	**+0.1 ± 4.5**	
Kelly				
176773	Komatiite	+9.5 ± 2.1	+0.2 ± 1.5	1.17
179828	Komatiitic basalt	+9.5 ± 3.8	+0.8 ± 3.1	0.212
179884	Komatiitic basalt	+7.5 ± 3.5	–1.8 ± 2.6	0.325
180220	Komatiitic basalt	+6.2 ± 3.4	–0.3 ± 2.7	0.210
Average (±2SD)		**+8.2 ± 3.3**	**–0.3 ± 2.2**	
Ruth Well				
137638	Komatiite	+9.1 ± 3.7	+0.4 ± 2.5	1.33
138239	Komatiite	+9.4 ± 2.5	+0.4 ± 2.0	4.24
138308	Komatiite	+7.8 ± 3.5	–2.4 ± 2.6	3.09
140258	Komatiite	+8.0 ± 3.1	–0.8 ± 2.3	1.25
158691a	Komatiite	+11.9 ± 1.9	+1.0 ± 1.4	3.73
158692b	Komatiite	+7.9 ± 2.2	+1.6 ± 1.7	3.76
137307	Komatiitic basalt	+11.7 ± 3.4	+1.7 ± 2.6	0.259
137314	Komatiitic basalt	+5.2 ± 3.9	+1.6 ± 2.6	0.327
137636	Komatiitic basalt	+6.7 ± 3.5	+0.2 ± 2.6	0.539
137644	Komatiitic basalt	+5.1 ± 2.8	–1.3 ± 2.0	0.391
140259	Komatiitic basalt	+8.7 ± 2.2	0.0 ± 1.7	0.515
Average (±2SD)		**+8.3 ± 4.5**	**+0.2 ± 2.6**	
Regal				
176720	Komatiite	+11.7 ± 2.2	+1.4 ± 1.6	2.18
176721	Komatiite	+12.3 ± 5.0	–3.9 ± 3.6	5.37
Replicate	Komatiite	+15.8 ± 2.8	+2.0 ± 2.2	5.37
176722	Komatiite	+14.5 ± 2.7	+1.9 ± 2.0	5.02
176723	Komatiite	+9.4 ± 3.0	+0.5 ± 2.1	2.44
176724	Komatiite	+10.0 ± 3.2	+0.3 ± 2.3	3.50
176725	Komatiite	+11.8 ± 2.7	+0.4 ± 2.0	2.63
176736	Basalt	+9.1 ± 2.9	0.0 ± 2.3	0.645
Average (±2SD)		**+11.8 ± 4.8**	**+0.3 ± 3.8**	

Note. Uncertainties on the W isotopic compositions for individual samples are the 2SE in-run precision of the analyses. Replicate – replicate digestion and analysis of the same sample.

obtained an average $\mu^{182}W = +11.2 \pm 2.9$ (2SD). Tusch et al. (2021) presented W isotopic and abundance data for three basaltic samples from Coonterunah (average $\mu^{182}W = +8.4 \pm 6.0$, 2SD), two basaltic samples from Kelly (average $\mu^{182}W = +6.2 \pm 3.9$, 2SD), and two basaltic samples from Ruth Well (average $\mu^{182}W = +9.8 \pm 3.7$, 2SD). None of these samples were analyzed in our study. Overall, the new W isotopic data are in good agreement with the results reported in these prior studies (Fig. 10).

5. DISCUSSION

5.1. Effects of secondary alteration

All four Pilbara komatiite-basalt systems studied here have undergone seafloor alteration and regional metamorphism up to the upper greenschist to lower amphibolite facies conditions (Smithies et al., 2007). This has resulted in complete or near-complete obliteration of primary mineralogy. These processes could have also resulted in modification of the magmatic chemical and isotopic signatures in the Pilbara komatiites and basalts. It is, thus, important to address the issue of potential postmagmatic mobility of the petrogenetically significant components.

Postmagmatic element mobility was evaluated by examining the variations of concentrations of the elements of interest versus MgO abundances in order to determine whether the former followed the inferred liquid lines of descent, or olivine control lines (Fig. 3). The validity of this approach has been demonstrated by several pioneering studies (e.g., Arndt, 1986, 1994). As noted in the Results section, the concentrations of alkalis, CaO, U, W, and Re

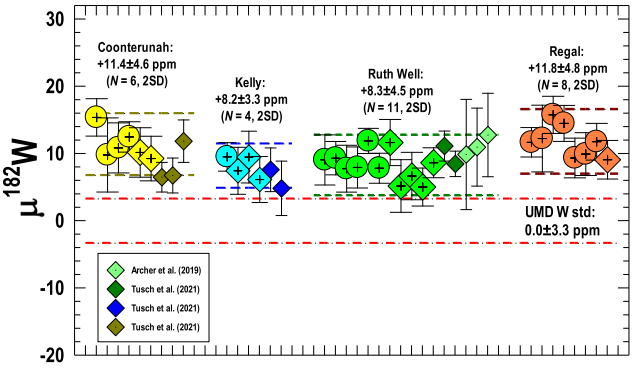

Fig. 10. Tungsten isotopic compositions of samples from the four Pilbara komatiite-basalt systems analyzed in this study. The data are reported in $\mu^{182}W$ units, i.e., part per million (ppm) deviations of the $^{182}W/^{184}W$ ratio of a given sample relative to the mean $^{182}W/^{184}W$ ratio measured for the Alfa Aesar W standard. Each symbol corresponds to a separately digested and analyzed sample. Data from Archer et al. (2019) and Tusch et al. (2021) are plotted for comparison.

do not show any meaningful correlations with MgO, and are, therefore, interpreted to have been modified by post-magmatic processes. All other major, minor, lithophile trace, and siderophile elements analyzed here generally follow olivine control lines and, thus, are concluded here to have been negligibly affected by seafloor alteration, metamorphism, and weathering.

5.2. Compositions of the emplaced komatiite magmas

Accurate determination of the composition of the emplaced komatiite magmas for the Pilbara komatiite systems is crucial for estimating the degree of melting and calculating the trace element, including HSE, contents in the respective mantle sources. As with other komatiite systems, in order to accomplish this task, several independent approaches have been utilized in the past, as outlined in Arndt (1986, 1994) and Nisbet et al. (1993). Here, we use the approaches that are most appropriate for the sample sets examined in this study. We then compare our results with those obtained in several other studies using independent approaches (e.g., Nebel et al., 2014; Sossi et al., 2016).

One approach uses the compositions of the upper chilled margins (flowtops) of komatiite lava flows as a proxy for the parental liquid composition. This approach is based on the observation that flowtops likely crystallized rapidly and, therefore, experienced little or no differentiation before complete solidification (Arndt, 1986, 1994). One of the issues with this approach is that, being in direct contact with seawater, flowtops may be strongly affected by seafloor alteration and fluid infiltration (Arndt, 1986; Lahaye and Arndt, 1996). Another issue is that, being the thinnest parts of lava flows, flowtops are less frequently preserved and/or are missed during sampling. Among the four Pilbara komatiite sample sets, only the Coonterunah and Ruth Well suites contain well-defined upper chilled margin samples, which have 23.3 wt.% MgO (179751) and 28.9 wt.% MgO (138239), respectively.

A second approach is based on the well-established relationship between the composition of the olivine and that of the liquid it crystallized from (Roeder and Emslie, 1970; Beattie et al., 1991). This approach, although widely used in melt inclusion research (e.g., Sobolev et al., 2016, 2019), and also where pristine magmatic olivine is well preserved (e.g., Arndt, 1986, Puchtel et al., 2009b), has its limitations due to generally poor preservation of olivine in komatiites. None of the four komatiite systems studied here contain magmatic olivine. Therefore, this approach cannot be directly applied in this study, but only as part of a third approach that requires calculation of the average MgO content of liquidus olivine in equilibrium with the emplaced lava by means of extrapolating the liquid lines of descent for the elements that are incompatible in olivine, towards their intercepts with the MgO axis. The average calculated MgO content of the olivine obtained this way is then used to calculate the MgO content of the emplaced lava using the second approach. Following this protocol, *Isoplot* regressions for 20 elements gave average MgO intercepts of 50.7 ± 0.6, 51.7 ± 0.7, and 52.0 ± 0.7 wt.% for the Coonterunah, Kelly, and Ruth Well-Regal systems, respectively. These olivine compositions can be shown to be in equilibrium with komatiite liquids containing 22.7 ± 0.6, 27.4 ± 1.0, and 28.9 ± 1.0 wt.% MgO and 11.0, 10.8, and 12.0 wt.% FeO, respectively. The results for the Coonterunah and Ruth Well-Regal systems from the third approach corroborate those obtained using the first approach.

Our results are also consistent with the estimates of Nebel et al. (2014) and Sossi et al. (2016) for the Coonterunah and Ruth Well-Regal systems of 23.0 and 29.0 wt.% MgO, respectively. Using the average MgO contents of 23.0 ± 0.3, 27.4 ± 1.0, and 29.0 ± 0.7 wt.% MgO for the Coonterunah, Kelly, and Ruth Well-Regal komatiite systems and projecting the trace element abundance data via *Isoplot* regression calculations to these values, the emplaced komatiite magma compositions for each of the four komatiite systems have been obtained and are reported in Table 7.

5.3. Lithophile trace element and isotope systematics of the Pilbara komatiites

In addition to secondary alteration, a major complicating factor in deciphering primary chemical features of komatiite lavas is contamination with upper crustal material *en route* to the surface and after emplacement. Owing

Table 7
Major and lithophile trace element abundances and Nd, Hf and W isotope compositions of the emplaced komatiite magmas, crustal contaminant endmember, and the calculated original komatiite magmas.

	1. Coont.	2. Kelly	3. RW	4. Regal	5. UCC	6. Orig. RW	7. Orig. Regal
TiO_2	0.340	0.283	0.358	0.346	0.640	0.355	0.343
Al_2O_3	8.07	6.23	3.95	4.08	15.4	3.81	3.95
Fe_2O_{3tot}	12.2	12.0	13.2	13.2	5.04	13.3	13.3
MgO	23.0	27.4	29.0	29.0	2.48	29.3	29.3
Zr	14.8	15.0	22.5	20.9	193	20.4	19.0
Y	5.75	6.13	7.49	7.37	21.0	7.33	7.22
Ga	6.09	6.08	5.75	5.42	17.5	5.61	5.29
Th	0.0811	0.0539	0.160	0.155	10.5	0.0341	0.0397
W[†]	0.0154	0.0102	0.0304	0.0295	1.90	0.00648	0.00754
U	0.0203	0.0135	0.0399	0.0387	2.70	0.00761	0.00910
Nb	0.798	0.490	0.588	0.604	12.0	0.440	0.487
La	0.878	0.546	1.11	1.11	31.0	0.743	0.780
Ce	2.60	1.62	2.73	2.63	63.0	2.00	1.961
Pr	0.411	0.273	0.447	0.412	7.10	0.366	0.338
Nd	2.13	1.49	2.42	2.19	27.0	2.12	1.91
Sm	0.685	0.530	0.895	0.827	4.70	0.849	0.784
Hf	0.493	0.414	0.627	0.556	5.30	0.570	0.504
Gd	0.926	0.747	1.20	1.15	4.00	1.17	1.12
Tb	0.164	0.138	0.213	0.208	0.700	0.207	0.203
Dy	1.13	0.966	1.39	1.40	3.90	1.36	1.37
Ho	0.243	0.213	0.276	0.273	0.830	0.2692	0.267
Er	0.752	0.648	0.788	0.783	2.30	0.769	0.766
Tm	0.115	0.0991	0.115	0.113	0.300	0.113	0.111
Yb	0.772	0.658	0.736	0.721	2.00	0.721	0.707
Lu	0.119	0.102	0.105	0.104	0.310	0.103	0.101
Al_2O_3/TiO_2	23.7	22.0	11.0	11.8	24.1	10.7	11.5
$(La/Sm)_N$	0.807	0.648	0.778	0.847	4.15	0.551	0.627
$(Gd/Yb)_N$	0.969	0.917	1.32	1.29	1.62	1.31	1.28
$(Nb/Th)_N$	1.30	1.20	0.485	0.514	0.150	1.70	1.61
Nb/Nb*	1.08	1.03	0.506	0.527	0.241	1.00	1.00
$\varepsilon^{143}Nd(T)$	+2.4 ± 0.2	+0.5 ± 0.2	+0.6 ± 0.2	+1.1 ± 0.2		+1.3 ± 0.4	+1.9 ± 0.3
$^{147}Sm/^{144}Nd$	0.214 ± 1	0.200 ± 1	0.200 ± 1	0.203 ± 1	0.105	0.204 ± 2	0.207 ± 2
$\varepsilon^{176}Hf(T)$	+4.4 ± 0.3	+1.7 ± 0.6	+1.7 ± 0.2	+4.1 ± 0.4		+2.4 ± 0.4	+4.6 ± 0.8
$^{176}Lu/^{177}Hf$	0.0395 ± 4	0.0355 ± 7	0.0353 ± 2	0.0378 ± 4	0.00814	0.0360 ± 5	0.0382 ± 8
$\mu^{182}W$	+11.4 ± 4.6	+8.2 ± 3.3	+8.3 ± 4.5	+11.8 ± 4.8	+8.9 ± 3.1[††]	+7.7 ± 5.0	+7.7 ± 5.0

1–4 – emplaced komatiite magma compositions for the Coonterunah, Kelly, Ruth Well, and Regal komatiite systems; 5 – the crustal contaminant endmember (UCC from Rudnick and Gao, 2014); 6, 7 – calculated original Ruth Well and Regal emplaced komatiite magma compositions corrected for CC. The initial $\varepsilon^{143}Nd$ and $\varepsilon^{176}Hf$ values calculated for T = 3530 Ma (Coonterunah), 3335 Ma (Kelly), 3171 Ma (Ruth Well), and 3176 Ma (Regal).

[†] W concentrations in the emplaced komatiite magmas were calculated using concentrations of fluid-immobile Th and the $W/Th_{BSE} = 0.19$ (McDonough and Sun, 1995).

[††] Average for 3.5 Ga granitic rocks from the Pilbara Craton (Tusch et al., 2021).

to their very high liquidus temperatures of up to 1600 °C and low viscosities (Huppert et al., 1984; Huppert and Sparks, 1985), during their passage through the continental crust, komatiitic liquids are highly susceptible to contamination by upper crustal rocks. Crustal rocks are strongly enriched in Th, U, and light REE, relatively depleted in Nb as a result of subduction zone processes (i.e., retention of Nb-rich rutile in the eclogitic residue: Rudnick et al., 2000; Rudnick and Gao, 2014) and, on BSE-normalized trace element diagrams, are characterized by pronounced negative Nb anomalies relative to the elements with similar incompatibility during mantle melting (Th and La), i.e., their $Nb/Nb^* \ll 1.0$ (where $Nb/Nb^* = Nb_N/\sqrt{(Th_N \times La_N)}$). By contrast, uncontaminated komatiitic magmas are expected to have Nb/Nb* = 1.0 (Jochum et al., 1991; Puchtel et al., 1998, 1999). Due to large differences in the highly incompatible lithophile trace element concentrations between the upper continental crust and komatiitic melts, crustal contamination usually results in sharp increases in the abundances of Th, U, and light REE, but much less so of Nb, in the hybrid melts, thus, imparting negative Nb anomalies to these hybrid magmas. As a result, Nb/Nb* is a tool which can be utilized as a measure of the degree of crustal contamination (e.g., Puchtel et al., 2016b, 2020). In addition, if the upper crustal rocks are much older than the komatiitic lavas, or were derived from sources compositionally different from

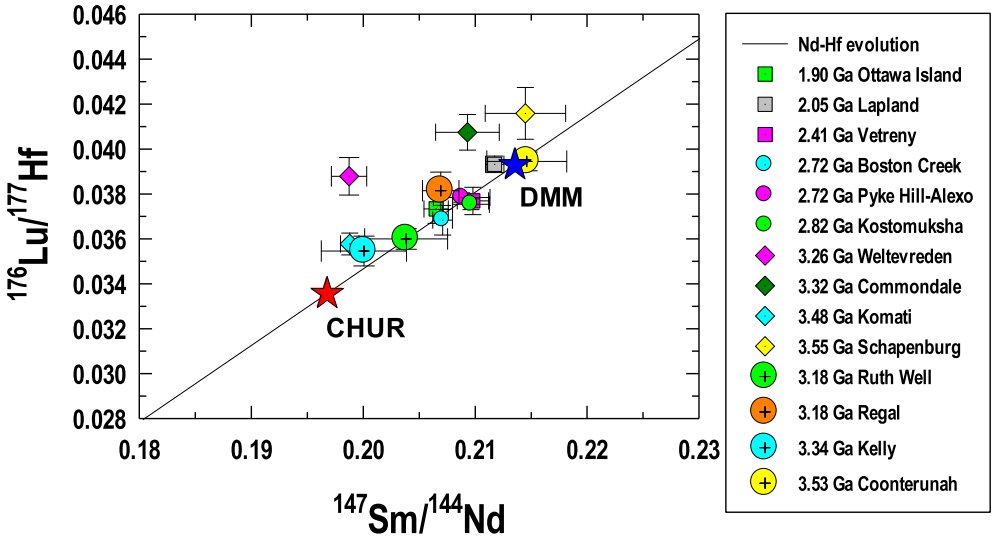

Fig. 11. Diagram illustrating the calculated time-integrated $^{147}Sm/^{144}Nd$ and $^{176}Lu/^{177}Hf$ for the mantle sources of the four Pilbara komatiite-basalt systems and for the Chondritic Uniform Reservoir (CHUR) and Depleted MORB Mantle (DMM). Also plotted for comparison are data for other well-studied komatiite and basalt systems. The sources of the data are as follows. Ottawa – Blichert-Toft and Arndt (1999); Lapland –Puchtel et al. (2020); Vetreny – Puchtel et al. (2016b); Alexo and Pyke Hill – Machado et al. (1986), Walker et al. (1988), Blichert-Toft and Arndt (1999); Boston Creek – Puchtel et al. (2018); Kostomuksha – Puchtel et al. (1998) and Blichert-Toft and Puchtel (2010); Komati and Weltevreden – Puchtel et al. (2013); Commondale – Wilson and Carlson (1989) and Hoffmann and Wilson (2017); Schapenburg – Puchtel et al. (2016a), Coonterunah, Kelly, Ruth Well, and Regal – this study. The CHUR and DMM parameters are from Jacobsen and Wasserburg (1980), Bouvier et al. (2008), and Blichert-Toft and Puchtel (2010). Note the coupled, or congruent, behavior between the two isotope systems in the sources of the Pilbara komatiites and basalts resulting in the data plotting on the terrestrial array. The Nd and Hf isotope data for the Ruth Well and Regal komatiite systems have been corrected to remove the effects of crustal contamination. See text for more details.

those of the komatiites, a suite of variably crustally contaminated lavas can be expected to produce mixing lines in the Sm-Nd isotope space that may yield erroneous ages and/or initial Nd isotopic compositions (e.g., Chauvel et al., 1985; Compston et al., 1986; Puchtel et al., 1997; Vezinet et al., 2021).

As discussed in the Results section, the Coonterunah and Kelly komatiites and komatiitic basalts have Nb/Nb* that are close to unity (Table 2). Moreover, these samples define whole-rock Sm-Nd and Lu-Hf isochrons for the respective units with the slopes that are consistent with the accepted emplacement ages of the respective volcanic sequences. Therefore, the Coonterunah and Kelly lavas are concluded to show no signs of crustal contamination.

Conversely, the Ruth Well and Regal komatiites and basalts are characterized by pronounced negative Nb anomalies (Table 2, Fig. 4c–d). It is, therefore, likely that the original Ruth Well and Regal komatiite magmas were contaminated via thermal erosion of upper crustal rocks of the Pilbara Craton. Archean upper continental crust (UCC) is considered to be the most likely contaminant of Archean mafic–ultramafic magmas due to its global distribution, low temperature of fusion and composition that best matches compositions of crustally contaminated komatiites and basalts worldwide, which usually contain old inherited zircon with granitic provenance (e.g., Claoue-Long et al., 1984; Cattell et al., 1984; Chauvel et al., 1985; Huppert and Sparks, 1985; Compston et al., 1986; Arndt and Jenner, 1986; Jochum et al., 1991; Puchtel et al., 1997). In contrast to the UCC, lower continental crust is only mildly enriched in LREE and has a much smaller, if any, negative Nb anomaly (Rudnick and Fountain, 1995).

In order to estimate the degree of crustal contamination and to calculate the major- and lithophile trace element abundances of the original Ruth Well and Regal komatiite magmas, we performed un-mixing calculations assuming that they had Nb/Nb* = 1.0 (e.g., Jochum et al., 1991); the results of these calculations are presented in Table 7. For the lithophile trace element composition of the upper crustal contaminant endmember, we used the average compositions of the Archean UCC from Rudnick and Fountain (1995) and Rudnick and Gao (2003, 2014). For the composition of the hybrid magmas, we used the calculated compositions of the Ruth Well and Regal emplaced komatiite magmas (Table 7). Since W and U abundances do not show any correlation with the MgO content in these lavas, we used concentrations of immobile Th and $W/Th_{BSE} = 0.19$ and $Th/U_{BSE} = 4.0$, respectively, to calculate the W and U abundances in the respective emplaced komatiite magmas.

Un-mixing calculations indicate that, in order to produce the emplaced Ruth Well and Regal komatiite magmas with Nb/Nb* = 0.506 and 0.527, respectively, the original

komatiite magmas had to be mixed with 1.2% of the average Archean UCC composition (Nb/Nb* = 0.241: Rudnick and Gao, 2014).

To calculate the Nd and Hf isotopic compositions of the UCC endmember at the time of the Ruth Well and Regal komatiite magma emplacement, we assumed its derivation from a mantle source with a BSE-like Nd isotopic composition and Archean UCC-like Sm/Nd and Lu/Hf ratios at 3.50 Ga (the age of the majority of the TTG complexes in the area: e.g., Van Kranendonk et al., 2006; Smithies et al., 2007), and its evolution from this starting composition to the times of the respective komatiite magma emplacements (3171 and 3176 Ma). Using the calculated 1.2% degree of contamination and the Nd and Hf abundances and initial Nd and Hf isotopic compositions of the Archean UCC calculated at the time of the respective komatiite magma emplacements, the original komatiite magmas and, thus, their mantle sources, are estimated to have had initial ε^{143}Nd values of +1.3 ± 0.7 and +1.9 ± 0.3, and initial ε^{176}Hf values of +2.4 ± 0.2 and +4.5 ± 0.4, respectively (Table 7).

It should be noted that the uncertainties on the calculated Nd and Hf isotopic compositions of the primary Ruth Well and Regal komatiite magmas are relatively small. This is due to the internally consistent method that we utilized in this study, which relies on the close relationship between the Nb/Nb* ratio of the contaminant and its La/Sm ratio (Rudnick and Gao, 2003, 2014). This minimizes the effects of potential variations in the trace element composition of the contaminant on the calculated composition of the primary komatiites magmas. Other important factors are the relatively small (1.2%) degree of crustal contamination and the well-constrained age of the most likely crustal contaminant endmember in the region.

The Sm-Nd and Lu-Hf isotopic data, thus obtained, indicate that the mantle sources of the four Pilbara komatiite-basalt systems, while all characterized by variable long-term depletions in highly incompatible lithophile trace elements, were relatively heterogeneous with respect to the time-integrated Sm/Nd and Lu/Hf Nd ratios. To quantify the degrees of long-term depletions of each of the four komatiite sources, we calculated the minimum $^{147}Sm/^{144}Nd$ and $^{176}Lu/^{177}Hf$ ratios that would be required to bring the isotopic compositions of the respective komatiite sources to their initial $^{143}Nd/^{144}Nd$ and $^{176}Hf/^{177}Hf$ at the time of komatiite lava emplacements, assuming their formation during an early melting event at 4467 Ma, i.e., 100 Ma after the start of the Solar System, from a BSE-like mantle source. The results of these calculations are plotted in Fig. 11, together with the data for other Archean and early Proterozoic komatiite-basalt complexes worldwide.

Several important observations can be gleaned from these results. First, the Pilbara komatiite-basalt sources span the entire range of the time-integrated $^{147}Sm/^{144}Nd$ and $^{176}Lu/^{177}Hf$ ratios defined by the komatiite-basalt systems studied to-date, from the 3.48 Ga Komati and 3.26 Ga Weltevreden on the low end, to the 3.55 Ga Schapenburg on the high end of the range. Second, in contrast to other early Archean komatiite systems (e.g., Schapenburg, Komati, Commondale, and Weltevreden), their early Archean Pilbara counterparts plot on or near the Nd-Hf mantle array of Blichert-Toft and Puchtel (2010), thus, displaying coupled behavior. The Nd-Hf mantle array owes its origin to the coupled, or congruent, Nd-Hf isotope

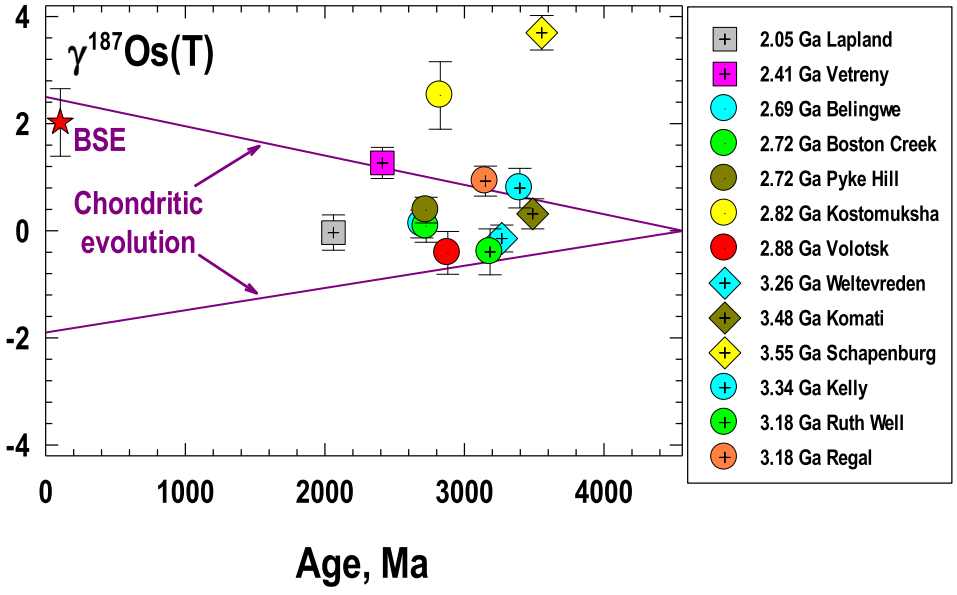

Fig. 12. Initial $^{187}Os/^{188}Os$ isotopic compositions, expressed in $\gamma^{187}Os$ terms, of the Archean komatiite systems plotted as a function of age. The sources of the data are as follows. Lapland – Puchtel et al. (2020); Vetreny Belt – Puchtel et al. (2016b); Belingwe – Puchtel et al. (2009b); Boston Creek – Puchtel et al. (2018); Pyke Hill – Puchtel et al. (2004a); Kostomuksha – Puchtel et al. (2005); Volotsk – Puchtel et al. (2007); Weltevreden and Komati – Puchtel et al. (2014); Schapenburg – Puchtel et al. (2009a), Puchtel et al. (2016a), Kelly, Ruth Well, and Regal – this study. Uncertainties are 2SD. The data for chondritic meteorites are compiled from Walker et al. (2002), Brandon et al. (2005), and Fischer-Gödde et al. (2010).

systematics of most terrestrial rocks that arises from similar partitioning behavior of the parent (^{147}Sm, ^{176}Lu) and daughter (^{143}Nd, ^{176}Hf) isotopes of the Sm-Nd and Lu-Hf systems during upper mantle differentiation and crust-forming processes (e.g., Patchett et al., 1981; Salters and White, 1998; Vervoort and Blichert-Toft, 1999; Vervoort et al., 1999, 2000). During mantle melting, both parent isotopes are less incompatible with the melt fraction than the daughter isotopes, which results in higher Sm/Nd and Lu/Hf ratios in the melting residue compared to the melt; over time, the residual mantle evolves to more radiogenic Nd and Hf isotopic compositions than the extracted crust. Both isotope systems are lithophile, refractory, insensitive to redox conditions and largely immobile during alteration and metamorphism. These properties make them useful for investigating the interplay between the formation and recycling of oceanic and continental crust in driving the geochemical evolution of the mantle.

On the other hand, the decoupling of the Nd and Hf isotope systematics (and, thus, deviation from the terrestrial Nd-Hf array) in the early Archean komatiite-basalt systems, such as Schapenburg, Weltevreden or Komati, has been interpreted to reflect the involvement of several processes. The most frequently cited are primordial magma ocean processes (i.e., fractionation of the high-pressure Ca-perovskite – bridgmanite mineral assemblage during magma ocean crystallization). These processes operated during the formation of lower mantle source regions that have been subsequently isolated for hundreds of millions of years (e.g., Caro et al., 2005; Rizo et al., 2011; Hoffmann et al., 2011; Puchtel et al., 2013, 2016a; Boyet et al., 2021).

Another process that can cause decoupling of the Nd-Hf systematics in komatiites and basalts is recycling of deep pelagic sediments into the mantle (e.g., Blichert-Toft et al., 2015). This is due to the fact that the Lu/Hf ratio is strongly fractionated relative to Sm/Nd in the Earth's sedimentary system (Patchett et al., 1984). This fractionation is caused by high resistance to chemical weathering of the mineral zircon. During weathering of continental crustal rocks, they break down into zircon-enriched sandy sediments with very low Lu/Hf and fine-grained zircon-depleted clay material with up to three times the chondritic Lu/Hf ratio. During sediment transport via turbidity currents, sandy sediments stay on or near the continent, while the pelagic material is carried onto the ocean floor, where it may eventually be subducted into the mantle.

The fact that none of the studied Pilbara komatiite systems significantly deviate from the terrestrial Nd-Hf mantle array provide strong evidence for a limited, if any, involvement of the early magma ocean or pelagic sediment subduction processes in the formation of their mantle source regions. This conclusion is also consistent with the ^{142}Nd/^{144}Nd isotope data for the 3.47–3.18 Ga Pilbara mafic–ultramafic rocks (Archer et al., 2019; Murphy et al., 2021) that indicate uniform $\mu^{142}Nd = 0$ values in all samples analyzed by these authors.

An important result of this study is the recognition of the fact that the Nd-Hf mantle array has been already established by the time the earliest rocks of the Pilbara Craton have formed, i.e., by 3.5 Ga. Although the modern Nd-Hf terrestrial array has long been recognized and described in the literature (e.g., Salters, 1996; Salters and White, 1998), its Archean counterpart is less well established (e.g., Vervoort et al., 1996, 1999, 2000; Vervoort and Blichert-Toft, 1999; Blichert-Toft and Puchtel, 2010). This study provides additional insight into the evolution of the early Archean mantle in terms of the Nd-Hf systematics.

Importantly, the early Archean mantle sources studied to-date have both the lowest and the highest ^{147}Sm/^{144}Nd and ^{176}Lu/^{177}Hf time-integrated ratios (Fig. 11), some of which (e.g., Kelly, Komati) are similar to those of CHUR, whereas some (e.g., Coonterunah, Schapenburg) are identical to those of the modern DMM reservoir. This provides strong evidence that as early as 3.5 Ga, which is the age of the oldest known komatiite occurrences, there existed reservoirs in the mantle with very diverse long-term Sm/Nd and Lu/Hf ratios, and some of these reservoirs were already as strongly depleted in more incompatible lithophile trace elements relative to less incompatible as the modern DMM. This in turn implies that a significant volume of mafic crust had already been extracted from the mantle, at least locally, as early as 3.5 Ga, and, perhaps, been converted into continental crust soon thereafter. Although the estimates vary significantly and are model-dependent, a number of studies have concluded that up to 70–75% of modern continental crustal volume already existed by 3.0 Ga (Sylvester et al., 1997; Campbell, 2003; Shirey et al., 2008; Jones et al., 2019; Kumari et al., 2019).

The only element for which the mixing calculations were unable to produce viable results was W. The W abundances in both the emplaced and primary, uncontaminated komatiite magmas, calculated using the obtained Th concentrations and $W/Th_{BSE} = 0.19$, are significantly lower than the measured W concentrations. This most likely indicates that W has been introduced into these komatiites during postmagmatic processes. This issue will be discussed in more detail in the section on the origin of W in the Pilbara komatiites and basalts.

5.4. HSE systematics of the Pilbara komatiite-basalt sources

In this section, the long-term Re/Os ratios and HSE abundances in the sources of the Pilbara komatiites and basalts, using the Os isotopic compositions and HSE abundances obtained for the komatiites, are estimated. The 1.2% crustal contamination is calculated to have had a negligible effect on the Os isotopic composition and HSE abundances in the Ruth Well and Regal komatiites, increasing their initial γ^{187}Os by <0.01 units and decreasing their HSE abundances by ≪1%, i.e., well within the uncertainties of the measurements, consistent with the previous studies (e.g., Puchtel et al., 2020).

Here, as in several previous studies (e.g., Puchtel et al., 2018, 2020), the absolute and relative (e.g., Re/Os) HSE abundances in the Pilbara komatiite sources have been calculated using the bootstrap method of Puchtel et al. (2004b) that combines the Os isotopic and HSE abundance data for a suite of komatiitic lavas derived from a common primary

magma, and related by fractional crystallization of olivine after lava emplacement.

In order to model the time-integrated evolution of Re/Os in the mantle sources of the Kelly, Ruth Well, and Regal komatiite systems, the initial $^{187}Os/^{188}Os$ ratios obtained for these systems (Table 7) have been used to calculate the minimum $^{187}Re/^{188}Os$ ratios required to evolve to these Os isotopic compositions by 3335, 3171, and 3176 Ma, respectively, and assuming formation of the respective mantle domains shortly after the start of the Solar System. Evolution of the Kelly, Ruth Well, and Regal sources from an early Solar System $^{187}Os/^{188}Os = 0.09517$ at 4567 Ma (Archer et al., 2014) to the initial $^{187}Os/^{188}Os$ ratios of 0.10490 ± 38, 0.10481 ± 45, and 0.10622 ± 14 at 3335, 3171, and 3176 Ma, respectively, requires $^{187}Re/^{188}Os$ ratios of 0.441 ± 18, 0.385 ± 18, and 0.442 ± 12, respectively. These time-integrated $^{187}Re/^{188}Os$ ratios for the three komatiite systems are within the range of chondritic meteorites, and their calculated initial $\gamma^{187}Os$ values are also within the range of most Archean and Proterozoic komatiite sources (Fig. 12).

In order to evaluate the HSE abundances in the sources of the Pilbara komatiites, the sulfide saturation status of their primary magmas, the most important parameter in determining whether komatiitic HSE abundances accurately reflect those in their mantle sources, needs to be established. Steenstra et al. (2020) presented a refined parameterization model for calculating the sulfur concentration at sulfide saturation (SCSS) as a function of pressure, temperature (P-T), and major and trace element abundances of silicate liquids. This model is applied here to determine the sulfide saturation status of the Pilbara komatiite magmas upon both separation from the melting residue and lava emplacement.

In order to calculate the P-T parameters of the komatiite magma generation for the four komatiite systems, the mantle melting parameterization models of McKenzie and Bickle (1988), Herzberg and Gazel (2009), and Herzberg et al. (2010) were used. The results of these calculations are presented in Table 8. The liquidus temperatures upon lava emplacement are estimated to be T_{liq} = 1509, 1557, and 1582 °C, and the depths of melting initiation D_{init} = 219, 337, and 444 km, which translate into the pressures of 7.1, 10.9, and 14.3 GPa for the Coonterunah, Kelly, and Ruth Well – Regal komatiite systems, respectively.

The ***maximum*** P-T parameters at which melting must have terminated for the four komatiite systems were then constrained using the parameterization models of Herzberg and Gazel (2009) and Herzberg et al. (2010) as follows (Table 8).

The Coonterunah and Kelly komatiites are Al-undepleted, which implies that their parental magmas must have formed in the spinel lherzolite stability field at depths <200 km and corresponding pressures of <6.5 GPa (Herzberg et al., 1988). This value is conservatively assumed here to be the maximum depth of the melting termination and komatiite magma separation from its source. The temperatures at which melting terminated for the Coonterunah and Kelly komatiite systems were then calculated to be 1770 and 1828 °C using the adiabatic P-T melting path equation from Herzberg and Gazel (2009).

The Ruth Well and Regal komatiites are Al-depleted, which implies that their parental magmas must have formed in the majorite garnet stability field, i.e., at depths >200 km and corresponding pressures of >6.5 GPa (Herzberg et al., 1988). This determines the minimum depth of their separation from the mantle source. The maximum depth of their separation from the source is determined by the depth of

Table 8
The calculated P-T and SCSS parameters, HSE and S abundances and Re-Os isotopic compositions of the original Coonterunah, Kelly, Ruth Well, and Regal komatiite magmas upon separation from the melting residue and upon emplacement, and their mantle sources.

	1. Coonterunah	2. Kelly	3. Ruth Well	4. Regal
$\gamma^{187}Os(T)$	N.D.[a]	+0.8 ± 0.4	–0.4 ± 0.4	+0.9 ± 0.3
$^{187}Re/^{188}Os$	N.D.[a]	0.441 ± 18	0.385 ± 18	0.442 ± 12
T_{liq} (°C)	1509	1557	1582	1582
D_{init} (km)	219	337	444	444
P_{init} (GPa)	7.1	10.9	14.3	14.3
Max D_{term} (km)	200	200	400	400
Max P_{term} (GPa)	6.5	6.5	12.9	12.9
Max T_{term} (°C)	1770	1828	1946	1946
Min $SCSS_{term}$ (ppm)	1077	1252	789	789
$SCSS_{emplacement}$ (ppm)	1871	2134	2710	2710
F (%)	44	55	60	60
Max S_{source} (ppm)	250	250	250	250
Max S_{magma} (ppm)	540	443	415	415
Pt_{magma}	4.30 ± 0.36	4.82 ± 0.29	7.08 ± 0.31	9.04 ± 0.43
Pd_{magma}	4.70 ± 0.19	4.77 ± 0.33	5.99 ± 0.25	7.36 ± 0.33
Pt_{source}	2.10 ± 0.18	2.85 ± 0.17	4.37 ± 0.19	5.59 ± 0.27
Pd_{source}	2.19 ± 0.09	2.73 ± 0.19	3.68 ± 0.15	4.53 ± 0.20
$Pt + Pd_{source}$	4.29 ± 0.26	5.58 ± 0.36	8.06 ± 0.34	10.1 ± 0.5
$Pt + Pd_{source}$ (%BSE)	29 ± 6	38 ± 7	55 ± 4	70 ± 5

[a] Not Determined.

melting initiation of 444 km (14.3 GPa). We, thus, use 400 km (12.9 GPa) as a conservative estimate of the depth of separation of the primary Ruth Well and Regal komatiite magmas from the melting residue. The temperature at which melting terminated for the Ruth Well – Regal komatiite systems was then calculated to be 1946 °C also using the adiabatic P-T melting path equation from Herzberg and Gazel (2009). Further, using these P-T parameters, the compositions of the emplaced komatiite magmas (Table 7), and Eq. (4) from Steenstra et al. (2020), the SCSS of the Pilbara emplaced komatiite magmas upon separation from their respective melting residues and upon emplacement were calculated and reported in Table 8.

In order to evaluate the sulfide saturation status of the Pilbara emplaced komatiite magmas, the knowledge of their S contents is required. To estimate these, the S contents in their mantle sources and the degrees of melting must be estimated first.

The average S content of the BSE has been estimated to be 250 ± 50 ppm (McDonough and Sun, 1995), and that of the modern DMM has been estimated to be 195 ± 45 to 206 ± 25 ppm (Nielsen et al., 2014; Sun et al., 2020). The mantle sources of all Pilbara komatiites were variably depleted in highly incompatible lithophile trace elements, with the Coonterunah source as strongly melt-depleted as the modern DMM (Fig. 11). Since both the BSE and DMM sulfur content estimates overlap within the uncertainties, the maximum value of 250 ± 50 ppm as a conservative estimate of the maximum S content in all Pilbara komatiite sources is used here.

To estimate the degrees of partial melting that produced the original Pilbara komatiite magmas, a batch melting model and the abundances of the moderately incompatible lithophile trace elements (e.g., Nd, Sm, Hf) in these magmas and their mantle sources obtained via utilizing the projection technique of Puchtel et al. (2004b) and the partition coefficients for the major mantle phases from Green (1994) were used. Assuming that S was moderately incompatible during partial melting that likely produced the Pilbara komatiites, with the degree of incompatibility similar to that of Sm (e.g., McDonough and Sun, 1995), the primary Pilbara komatiite magmas are then calculated to have contained 540, 443, and 415 ppm S for the Coonterunah, Kelly, and Ruth Well – Regal komatiite systems, respectively (Table 8). These calculated S contents in the Pilbara komatiite magmas are, thus, by factors of 2–3× lower than the SCSS of the Pilbara komatiite magmas upon separation from the melting residue and by factors of 3–7× lower than the SCSS upon emplacement. These modeling results, thus, provide strong evidence for the sulfide-undersaturated nature of the Pilbara komatiite magmas. The minimal crustal contamination experienced by the Ruth Well and Regal komatiite magmas en route to the surface apparently has not resulted in their sulfide saturation, as evidenced by the Pt and Pd abundances in these lavas following olivine control lines (Fig. 8).

Given the sulfide undersaturated nature of the Pilbara komatiite magmas, the abundances of incompatible Pt and Pd in the emplaced komatiite magmas and their mantle sources were obtained by extrapolation of the liquid lines of descent for each element to the calculated MgO contents of the respective, emplaced komatiite magma compositions and the mantle MgO value of 38.0 wt.%, using *Isoplot* (Fig. 8). The concentrations of Pt and Pd in the emplaced Pilbara komatiite magmas and their mantle sources calculated in this manner are presented in Table 8.

As for the other HSE, due to the observed mobile behavior of Re after lava emplacement, as well as the lack of reliable correlations between MgO and Os, Ir, and Ru concentrations caused by the presence, along with olivine, of variable amounts of Os-Ir alloy and chromite on the liquidus in the Pilbara komatiite systems, the concentrations of these elements in the emplaced magmas or their sources cannot be estimated with any meaningful degree of accuracy.

The calculated total Pt and Pd abundances in the sources of the Pilbara komatiite systems are plotted as a function of their age in Fig. 13 and compared with data for other Archean and Proterozoic komatiite systems studied to date, and the BSE estimate of Becker et al. (2006). It should be noted that all the data presented in Fig. 13 have been produced using the same technique of Puchtel et al. (2004b) and, therefore, are internally consistent and comparable. The calculated total Pt and Pd abundances in the Pilbara komatiite sources range from 29 ± 6% in the Coonterunah komatiite system to 70 ± 5% in the Regal komatiite system, of those in the estimates for the modern BSE. The total calculated HSE abundances in the 3.53 Ga Coonterunah and 3.35 Ga Kelly komatiite systems are similar to those for the 3.55 Ga Schapenburg system of southern Africa, whereas the 3.18 Ga Ruth Well and Regal komatiite systems have the total calculated HSE abundances more similar to those in the 3.48 Ga Komati and 3.26 Ga Weltevreden komatiite systems, also of southern Africa. Overall, the entire dataset (Fig. 13), except for some apparent outliers (e.g., the Boston Creek and Vetreny systems), exhibits a broad trend of increasing HSE abundances in the komatiite mantle sources with decreasing age, generally consistent with the conclusions of Maier et al. (2009) and Fiorentini et al. (2011). In the following sections, the significance of this observation will be discussed in light of the available geochemical data.

5.5. The Nd-Hf-Os isotope paradox

There is an apparent disagreement between the radiogenic lithophile Sm-Nd and Lu-Hf isotopic systematics and the highly siderophile Re-Os isotopic systematics in komatiite mantle sources worldwide. The majority of the Archean and Proterozoic komatiite systems, such as those from the Abitibi (Canada) and Belingwe (South Africa) greenstone belts (Walker et al., 1988; Gangopadhyay and Walker, 2003; Puchtel et al., 2009b, 2018), the Sumozero-Kenozero and Vetreny (Fennoscandia) greenstone belts (Puchtel et al., 1999, 2007, 2016a,b), and the Central Lapland greenstone belt (Hanski et al., 2001; Gangopadhyay et al., 2006; Puchtel et al., 2020) are characterized by strong, long-term depletions in more incompatible lithophile trace elements relative to less incompatible elements, e.g., Nd

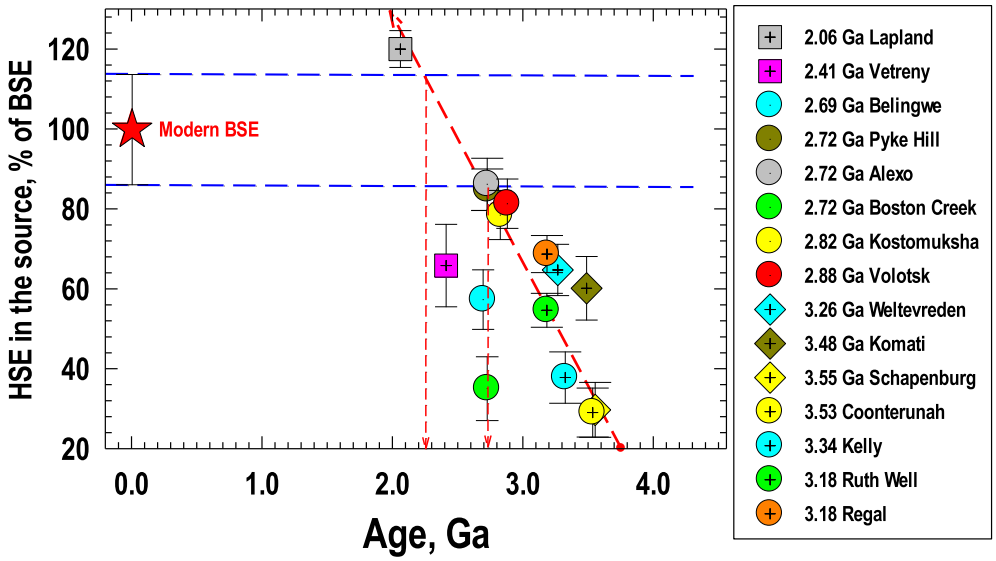

Fig. 13. Calculated total HSE abundances in the sources of Archean komatiite systems plotted as per cent of those in the estimates for modern BSE of Becker et al. (2006). The sources of the data are as follows. Lapland – Puchtel et al. (2020); Vetreny Belt – Puchtel et al. (2016b); Belingwe – Puchtel et al. (2009b); Pyke Hill and Alexo – Puchtel et al. (2004b); Boston Creek – Puchtel et al. (2018); Kostomuksha – Puchtel and Humayun (2005); Volotsk – Puchtel et al. (2007); Weltevreden and Komati – Puchtel et al. (2014); Schapenburg – Puchtel et al. (2009a), Puchtel et al. (2016a), Coonterunah, Kelly, Ruth Well, and Regal – this study. Uncertainties are 2SD. The data reveal a broad trend of increasing HSE concentrations in the komatiite mantle sources over the geological time. See text for additional details.

versus Sm and Hf versus Lu (Fig. 11), but have near chondritic time-integrated Re/Os (Fig. 12). These komatiite-basalt mantle sources must have experienced early melt depletion events that fractionated the Sm/Nd and Lu/Hf ratios to suprachondritic values high enough to bring the Nd and Hf isotopic compositions to the variably positive initial ε^{143}Nd and ε^{176}Hf values obtained in the above studies. Since Re is generally moderately incompatible during mantle melting (e.g., Mallmann and O'Neill, 2007), whereas Os is moderately to highly compatible (e.g., Gannoun et al., 2016), these melt extraction events should have also decreased the Re/Os ratios in the komatiite-basalt mantle sources. This would result in retardation of ^{187}Os ingrowth and evolution of the sources to variably negative initial γ^{187}Os values, which have not yet been observed in the global komatiite-basalt record.

This phenomenon has been termed the Nd-Hf-Os isotope paradox here. Puchtel et al. (2007, 2009b, 2020) offered a solution to this paradox by developing a model whereby the komatiite-basalt mantle sources experienced an early (100 Ma into the Solar System history), low-degree ($F < 1\%$) partial melting and melt extraction event that would have fractionated the Sm/Nd and Lu/Hf ratios in these sources, but had little effect on the Re/Os ratios due to a higher compatibility of Re compared to Nd and Hf during partial mantle melting. By applying this model to the Kelly, Ruth Well, and Regal komatiite systems and using the model parameters outlined most recently in Puchtel et al. (2020), we estimate the degrees of the early melting events necessary to reconcile the Nd-Hf-Os isotopic parameters of the Pilbara komatiite-basalts sources to be <1%, consistent with data for the other komatiite systems.

Because this phenomenon is apparently global in nature, it requires early formation and subsequent complete isolation of a globally distributed mafic crust enriched in incompatible lithophile trace elements. Calculations indicate that such crust, formed as a result of 0.5–1% batch melting of a BSE-like mantle, would contain 35–41 ppm Nd, 7.8–8.6 ppm Sm, 0.65–0.68 ppm Lu, and 5.7–6.4 ppm Hf, and would have ^{147}Sm/^{144}Nd = 0.127–0.134 and ^{176}Lu/^{177}Hf = 0.0148–0.0157 (compared to 0.1967 and 0.0336 in the BSE, respectively). Based on our estimates of the Sm and Nd concentrations in the early crust, the mass of this reservoir must have represented <2.5% of the mass of the BSE, which is consistent with this reservoir being the D″ layer (Boyet and Carlson, 2005). Alternatively, this earliest mafic crust could have served as the source of the oldest TTG complexes (Carlson et al., 2019), such as those from the Nuvvuagittuq Greenstone Belt (O'Neil et al., 2008, 2016).

The residence time of this early basaltic crust in the mantle is difficult to constrain. The available komatiite-basalt record would require its isolation through at least the late Archean, i.e., until the time when the ^{142}Nd anomalies were still present in the mantle (Debaille et al., 2013). However, there is no evidence that this crust was stored in the mantle until the present day, based on the generally chondritic ^{138}Ce, ^{142,143}Nd, and ^{176}Hf isotopic composition estimates for the modern BSE (Jackson and Carlson, 2012; Horan et al., 2018; Willig and Stracke, 2019; Willig et al., 2020; Hyung and Jacobsen, 2020).

5.6. Tungsten isotopic compositions of the Pilbara komatiite-basalt sources

Tungsten behavior during magmatic processes is mainly governed by the redox state of the magmatic system (Newsom et al., 1996). Under reducing conditions, typical of those that likely existed during the period of core

formation, W behaves as a moderately siderophile element, concentrating largely in the metallic core. Under relatively oxidizing conditions, such as those that are typical of the modern upper mantle, W behaves as a highly incompatible, lithophile trace element, concentrating in the silicate melt, with a degree of incompatibility similar to that of Th (Newsom et al., 1996, Arevalo and McDonough, 2008; König et al., 2011; Tusch et al., 2019).

The Archean mantle was recently shown to be only slightly (by ~1.3 ΔFMQ log units) less oxidized than the modern mantle (Nicklas et al., 2018). Therefore, it is expected that during mantle melting that produced the early Archean Pilbara komatiites, W behaved similarly to Th, and, therefore, on the diagrams in Fig. 4 should have had BSE-normalized abundances similar to those of Th. However, the W/Th ratios that quantify the deviation of measured W abundances from those that are expected on the basis of the magmatic behavior of W, are highly variable, and are generally higher than $W/Th_{BSE} = 0.19$, pointing to relative W enrichments in the majority of studied Pilbara komatiite and basalt samples. In addition, the lack of correlation between W concentrations and indices of magmatic differentiation, such as MgO content (Fig. 3), indicates W mobility after lava emplacement. The important issue to address, therefore, is the source of W in the Pilbara komatiites and basalts.

Because the Ruth Well and Regal komatiite-basalt systems were shown to have experienced 1.2% magmatic crustal contamination, and since upper crustal rocks have significantly higher W abundances, and possibly also different W isotopic compositions compared to these komatiites, crustal contamination may have significantly modified the W isotopic composition and W abundances of the parental melts to these komatiites.

To evaluate the potential effects of magmatic crustal contamination on the W isotopic composition and W abundances of the original Ruth Well and Regal komatiite magmas, we performed un-mixing calculations. It is assumed that the original komatiite magmas had W/Th = 0.19, which corresponds to their presumed original W abundances of ~6.0 ppb. The possible sources of upper crustal contamination in this part of the Pilbara Craton, for which W isotopic and abundance data are available, are the 3468 Ma North Shaw Tonalite, the 3460 Ma Homeward Bound Granite, and 3450 Ma North Pole Granite (Tusch et al., 2021). These granites have the average $\mu^{182}W = +8.9 \pm 3.1$ and W concentration of 530 ppb. The 1.2% contamination by this type of crustal material would increase the W concentration in the original komatiite magma to ~11 ppb, which is a factor of 25–50× lower than the W concentrations measured in the Ruth Well and Regal komatiites and basalts. In addition, because average Archean UCC has W/Th = 0.18 (Rudnick and Gao, 2014), similar to the BSE value of 0.19, magmatic crustal contamination also cannot explain the observed enrichments in W relative to Th (Table 7).

Since W is a highly fluid-mobile element (e.g., König et al., 2011; Touboul et al., 2014; Willbold et al., 2015; Liu et al., 2016), one possibility is that the excess W in the Ruth Well and Regal komatiites was derived from the Pilbara continental crustal rocks via fluid transfer. This could have occurred either during the passage of the komatiitic magmas through the crust *en route* to the surface, or after lava emplacement. A similar mechanism has been proposed by Liu et al. (2016) to account for the large W concentration anomalies in the Saglek mafic–ultramafic rocks. Liu et al. (2016) used the W enrichment factor to quantify the degree of W enrichments in the Saglek rock suite. Using their Eq. (1), we calculated the W enrichment factor for the Ruth Well and Regal lavas to be between 85% and 96% for the komatiites, and between 27% and 71% for the komatiitic basalts (Table 2).

The potential sources of such postmagmatic, fluid-induced W enrichments are the 3.47–3.45 Ga granites and tonalites of the Pilbara Craton. These granitic rocks are characterized by severe depletions in W, with an average W/Th ratio of 0.043, and, thus, must have lost ~80% of their W inventory. It is, therefore, possible that this lost W inventory was transferred to the Ruth Well and Regal komatiitic and basaltic rocks. In hydrothermally altered mafic–ultramafic rocks, 90% of all W resides mostly in serpentine, and, to a lesser extent, in chlorite and amphibole, which are all major hosts of W (Liu et al., 2016). These secondary minerals can accommodate much larger quantities of W compared to their precursor magmatic minerals (i.e., olivine and pyroxene). This is consistent with the altered nature of the Ruth Well and Regal komatiites and basalts, their large enrichments in W relative to Th, and the observed broad positive correlation between the MgO contents (e.g., reflecting the modal abundance of serpentine) and W concentrations (Fig. 3). We conclude, therefore, that the W abundances and W isotopic composition of the Ruth Well and Regal komatiites and komatiitic basalts are most likely dominated by that of the Pilbara Craton granitic rocks, which have an average $\mu^{182}W = +8.9 \pm 3.1$ (Tusch et al., 2021), identical, within the uncertainty, to the average $\mu^{182}W$ values for the Ruth Well and Regal komatiite-basalt systems ($\mu^{182}W = +8.3 \pm 4.5$ and $+11.8 \pm 4.8$, respectively).

Although the degree of W enrichment of the Ruth Well and Regal komatiites ranges between 85% and 96%, indicating that their W budgets were largely dominated by that of the fluid-derived W, the komatiitic basalts, with W/Th ratios ranging between 0.26 and 0.65, were much less affected. The $\mu^{182}W$ values in the komatiitic basalts vary between +5.1 and +11.7, with an average $\mu^{182}W = +7.7 \pm 5.0$. This value can be used as the upper limit for the W isotopic compositions of the Ruth Well and Regal komatiite-basalt sources.

As discussed above, the chemical compositions of the Coonterunah and Kelly komatiites and komatiitic basalts do not show any evidence of crustal contamination. Yet, the komatiites exhibit the same pattern of W enrichment relative to Th, albeit to a much smaller extent than the Ruth Well and Regal komatiites. In contrast to the Ruth Well and Regal komatiitic basalts, however, the Coonterunah komatiitic basalts have W/Th ratios that are identical to the BSE value, whereas the Kelly komatiitic basalts show both enrichments and depletions in W relative to Th, with the W/Th ratios ranging from 0.11 to 1.35 (Table 2).

Importantly, the measured W isotopic compositions of the Coonterunah and Kelly komatiites are identical, within the uncertainties, to those of the respective komatiitic basalts, among which only samples with the BSE-like W/Th ratios were analyzed for W isotopic composition.

We propose that the observed W enrichments in the Coonterunah and Kelly komatiites are the result of redistribution of W within the komatiite-basalt volcanic sequences at these localities. Several observations support this hypothesis. First, komatiites constitute <5% of the Pilbara volcanic sequences by volume, the rest being represented by basalts (Smithies et al., 2007). Basalts usually contain significantly higher abundances of highly incompatible trace elements, including W. Therefore, if W is mobilized and re-distributed within a komatiite-basalt volcanic sequence, it will be preferentially captured by komatiites during serpentinization of the primary mineral assemblage, as serpentine is a major trap for W (Liu et al., 2016). Second, the average W concentrations in the Coonterunah and Kelly komatiites are either similar to or significantly lower than those in the basalts at their respective localities, which would be expected if komatiites derived most of their W inventory from the spatially associated basalts. At the same time, W concentrations in the Kelly basalts vary by a factor of ~24×, which would be also expected if some of the basaltic W inventory has been lost to the komatiites. Provided this line of reasoning is correct, the measured W isotopic compositions of the Coonterunah and Kelly komatiites and komatiitic basalts are concluded to be representative of those in their mantle sources.

5.7. Reconciling siderophile element isotope and abundance systematics

Due to the contrasting behavior of Hf and W during the magmatic processes and the short half-life of ^{182}Hf (8.9 Ma), the ^{182}Hf-^{182}W isotopic system is a valuable, multi-faceted geochemical tool (e.g., Jacobsen and Harper, 1996; Kleine et al., 2002; Jacobsen and Yu, 2015). For example, in combination with the lithophile and Os isotope systematics and HSE abundances, the ^{182}Hf-^{182}W isotopic system can be used to decipher the effects of early planetary formation and differentiation, late accretion, and core-mantle interaction (e.g., Touboul et al., 2012; Puchtel et al., 2018, 2020; Archer et al., 2019; Rizo et al., 2019; Tusch et al., 2021).

Early metal-silicate fractionation in a primordial magma ocean would leave the silicate domain with high Hf/W due to preferential partitioning of W into the metal, whereas crystal-liquid fractionation would lead to high Hf/W in cumulates and low Hf/W in the residual liquid due to the more incompatible behavior of W relative to Hf (e.g., Touboul et al., 2012). If any of these fractionation processes occurred within the first ~60 Ma of Solar System history, both positive and negative ^{182}W anomalies would be created and would be accompanied by positive and negative ^{142}Nd anomalies (e.g., Puchtel et al., 2016a; Boyet et al., 2021). Addition of core metal that has high W concentrations and a μ^{182}W of ~−220 to a mantle domain having the W isotopic composition of the BSE would lead to creation of negative ^{182}W anomalies in that mantle domain and, thus, can be considered for core-mantle interaction (Rizo et al., 2019; Mundl-Petermeier et al., 2020). Addition of late accreted materials with bulk chondritic compositions, which have ~20 times higher W abundances and 190 ± 10 ppm less radiogenic ^{182}W/^{184}W than the BSE (Kleine et al., 2002, 2004a; Schoenberg et al., 2002; Yin et al., 2002), would lead to a decrease in ^{182}W/^{184}W of the mantle compared to the pre-late accretionary mantle (Willbold et al, 2011; Kruijer et al., 2015; Touboul et al., 2015). A mantle with a deficit of late accretionary components would be ^{182}W-enriched and HSE-depleted compared to mantle to which a full complement of late accretionary components was added. In this section, the cause of the positive ^{182}W anomalies observed in the Pilbara komatiites and basalts in the context of the above models is explored.

Apparently, these positive anomalies cannot be the result of core-mantle interaction, as this process would have resulted in the decrease in ^{182}W/^{184}W in the mantle sources of the Pilbara komatiites below the BSE value, as well as in the increase in the HSE abundances over the BSE levels, which is the opposite to what is observed.

Silicate-silicate fractionation in a primordial magma ocean could have created cumulate-rich mantle domains with high Hf/W (and Sm/Nd) ratios that, over time, would be expected to develop positive ^{182}W and complementary positive ^{142}Nd anomalies (Brown et al., 2014). However, the latter are not observed in any Pilbara komatiitic and basaltic rocks (Archer et al., 2019; Murphy et al., 2021). Moreover, whereas early magma ocean processes have been proposed to result in decoupling of the ^{143}Nd-^{176}Hf isotope systematics (e.g., Caro et al., 2005; Rizo et al., 2011; Puchtel et al., 2013, 2016a; Boyet et al., 2021) data for all the studied Pilbara komatiite-basalt systems plot on the terrestrial Nd-Hf array (Fig. 11), providing no evidence for involvement of early magma ocean processes in the generation of their mantle sources.

Metal-silicate fractionation and removal of metal in a primordial magma ocean is capable of fractionating Hf/W without significantly affecting Sm/Nd, at the same time depleting the mantle sources in the HSE below the BSE levels. However, the collateral effect of this process would also be fractionation of Re/Os (e.g., Touboul et al., 2012), which again is not observed in the Pilbara komatiite-basalt mantle sources. Except for the Coonterunah komatiite system, for which no viable initial γ^{187}Os data could be obtained, the other three Pilbara komatiite systems have evolved with Re/Os ratios that are within the chondritic range (Fig. 12).

By process of elimination, late accretion is concluded to be the most viable mechanism for creating the observed positive ^{182}W anomalies in the Pilbara komatiite-basalt sources. This is also the scenario most commonly appealed to given the ubiquotous presence of positive ^{182}W anomalies in the Hadean and early Archean rock record and their gradual disapperance in the late Archean (e.g., Willbold et al., 2011, 2015; Touboul et al., 2014; Puchtel et al., 2018; Archer et al., 2019, Reimink et al., 2020; Tusch et al., 2021).

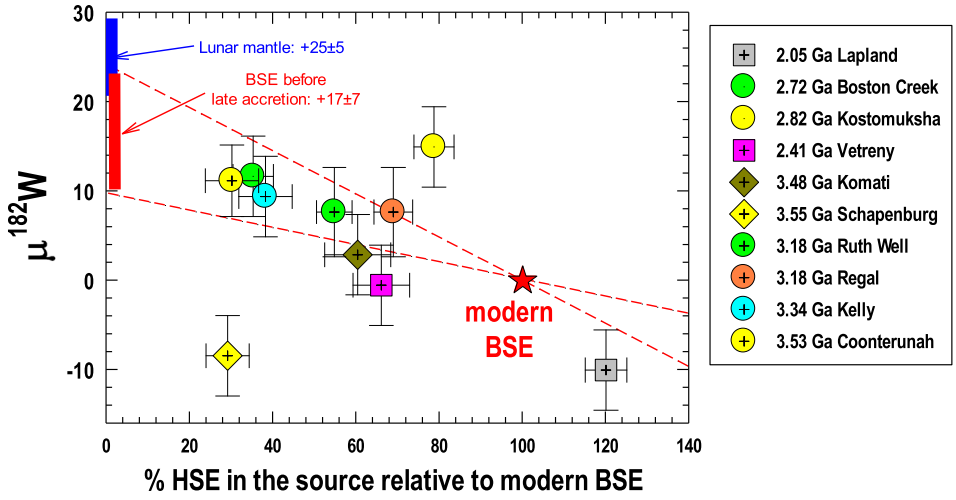

Fig. 14. $\mu^{182}W$ versus total calculated HSE abundances in the sources of Archean komatiite systems studied to date relative to those in the estimates for the present-day BSE of Becker et al. (2006). This proportion corresponds to the fraction of the total HSE budget of the BSE added during late accretion assuming an HSE-free BSE prior to late accretion. The $\mu^{182}W$ of the BSE prior to late accretion is constrained *via* *Isoplot* regression analysis of the $\mu^{182}W$ and HSE compositions of all komatiite-basalt systems, except for Kostomuksha and Schapenburg, and the present-day BSE to be $+17 \pm 7$. The $\mu^{182}W$ for the lunar mantle of $+25 \pm 5$ ppm (Kruijer et al., 2015; Touboul et al., 2015) is identical to the estimate for the pre-late accretionary BSE, providing further support to the notion that the Moon and Earth formed from material with identical ^{182}W compositions (Kleine and Walker, 2017). The W isotopic data and estimates of the HSE contents for the komatiite systems are from Puchtel and Humayun (2005), Touboul et al. (2012), Puchtel et al. (2014, 2016a,b, 2018, 2020), and this study.

In the context of the so-called grainy late accretion (Bottke et al., 2010; Marchi et al., 2018), whereby late accreted materials mostly consisted of several large (up to 3000 km in diameter: Ryder, 2002; Strom et al., 2005) differentiated planetesimals, which are not expected to be quickly homogenized within the mantle (Marchi et al., 2020), domains in the mantle would be created that would initially have both excesses and deficits of late accreted materials compared to the average amount required to account for the HSE budget of the BSE (e.g., Willbold et al., 2011, 2015). Grainy late accretion is expected to create inverse correlations between the magnitude of ^{182}W anomalies and HSE abundances in the mantle.

The $\mu^{182}W$ values obtained for the Pilbara komatiite-basalt systems versus the calculated total HSE abundances in their mantle sources, as percentages of those estimated for the modern BSE (Becker et al., 2006), are plotted in Fig. 14. The HSE percentages correspond to the fraction of the total late accreted component added to the BSE, assuming that the mantle was completely stripped of HSE by the time core formation ceased.

Using the new data for the four Pilbara komatiite systems, along with those for the other komatiite systems for which late accretion has been argued to be the main cause for the observed ^{182}W – source HSE abundance relationships (Fig. 14), and assuming that the ^{182}W excesses/deficit are due entirely to a deficit/overabundance of late accreted materials in their mantle sources, we calculated the W isotopic composition of the pre-late accretionary BSE. For that purpose, we used *Isoplot* regression analysis and the estimated uncertainties on the W isotopic compositions and HSE abundances of the sources of the komatiite systems. Modeling indicates that the pre-late accretionary BSE had $\mu^{182}W = +17 \pm 7$ (Fig. 14), which is identical to the ^{182}W excess in the pre-late accretionary BSE of $+18 \pm 9$ ppm estimated by Kleine and Walker (2017) using an independent approach. This estimate for the W isotopic composition of the pre-late accretionary BSE is also identical, within the uncertainties, to the estimates for the ^{182}W composition of the pre-late accretionary Moon of $+25 \pm 5$ ppm (Kruijer et al., 2015; Touboul et al., 2015; Kruijer and Kleine, 2017).

This new result provides further support to the hypothesis that the Earth and Moon formed from the material with identical W isotopic composition (Kleine and Walker, 2017), in concert with the earlier observations of the similarity of, e.g., O, Si, and Ti isotopic compositions between the Earth and Moon (e.g., Dauphas et al., 2014), as well as additional evidence that the Moon likely formed mainly from the terrestrial material, rather than from the material of the impactor.

5.8. Implications for the mantle stirring rates for the HSE

The term "late veneer", defined as accretion of 0.5–0.8% (Walker, 2009) of Earth's mass of meteoritic component after cessation of core formation, was introduced by Ringwood (1966) and elaborated upon by Chou (1978) and Chou et al. (1983) to explain the excess of the HSE abundances in the terrestrial mantle compared to what would be expected after core formation on the basis of the low pressure and temperature metal-silicate partitioning experiment data available at the time (e.g., Kimura et al., 1974). In earlier studies, it was assumed that this meteoritic component was added to the Earth in the form of relatively fine particulate (thus, the term "veneer", or a thin layer covering or completely enclosing an object). It has also been proposed that a slow vertical homogenization of this thin

layer of late accreted dusty materials has been responsible for the apparent temporal trend of increasing HSE abundances with time in Archean komatiites (e.g., Maier et al., 2009; Fiorentini et al., 2011). However, studies by Bottke et al. (2002, 2007) have concluded that it was highly unlikely that late accretion in the form of a rain of small meteoritic particles could have achieved an Earth/Moon late accretionary mass influx ratio of 1200 required on the basis of the HSE abundance and Re-Os isotopic studies of terrestrial (Meisel et al., 2001a,b; Becker et al., 2006; Fischer-Gödde et al., 2011) and lunar (Walker et al., 2004, 2014; Day et al., 2007; Day and Walker, 2015) samples.

With these results in mind, Bottke et al. (2010) proposed that late accretion to the Earth and Moon occurred not proportionally to their respective masses, but according to the different gravitational cross-section areas of the two bodies, via addition of a few large projectiles with mean diameters of 2500–3000 km and 250–300 km, respectively. In case of the Earth, projectiles of this size would be differentiated and consist of HSE-rich cores and HSE-stripped silicate mantles. Upon impact, depending on the size of the projectiles, the cores would either quickly emulsify within a resulting terrestrial magma ocean or merge with the Earth's core, whereas the silicate domains would be slowly homogenized within the Earth's mantle (Rubie et al., 2003; Dahl and Stevenson, 2010). As a result, mantle domains with low HSE abundances and positive ^{182}W anomalies on the one hand, and high HSE abundances and negative ^{182}W anomalies, on the other hand, would be generated.

Because the lunar highland crust, which was formed between 4.34 and 4.37 Ga (Borg et al., 2014), is essentially intact and is only modestly contaminated by meteoritic material (e.g., Day et al., 2010), late accretion must have been largely complete prior to ~4.4 Ga, i.e., within ~160 Ma into the Solar System history. We used the estimated HSE abundances in the sources of the Archean and Proterozoic komatiite systems plotted in Fig. 13 as a function of their ages and *Isoplot* regression analysis to calculate the average period in time by which the late accreted materials have been completely homogenized within the mantle. The regression calculations yield 2.5 ± 0.2 Ga (Fig. 13). This period in time coincides with the timing of the onset of modern-style plate tectonics on Earth, as argued by several researchers (Brown, 2007; Brown and Johnson, 2018), and with the complete disappearance of positive ^{182}W anomalies in the mantle (Carlson et al., 2019; Reimink et al., 2020, Tusch et al., 2021). These data require that survival times of the late accreted planetesimals within the mantle, before complete homogenization, were on average 1.9 ± 0.2 Ga, thus, constraining the average stirring rates of the terrestrial mantle in terms of the siderophile element abundances and isotope systematics in the Hadean and Archean.

6. CONCLUSIONS

The Sm-Nd and Lu-Hf isotope data for a comprehensive set of samples from the ~3.53 Ga Coonterunah, ~3.34 Ga Kelly, and ~3.18 Ga Ruth Well and Regal komatiite-basalt systems of the Pilbara Craton in Western Australia yield isochrons consistent with the accepted emplacement ages of the respective stratigraphic sequences. After correcting the Ruth Well and Regal data for crustal contamination, it was calculated that their mantle sources evolved with long-term model ^{147}Sm/^{144}Nd = 0.200–0.214 and ^{176}Lu/^{177}Hf = 0.0355–0.0395, spanning the entire range of time-integrated Sm/Nd and Lu/Hf ratios measured in the Archean and Proterozoic komatiite-basalt systems to-date. Unlike with the early Archean komatiite-basalt sources from the Kaapvaal Craton in South Africa, the coupled ^{143}Nd-^{176}Hf isotope systematics observed in the early Archean Pilbara Craton lavas argue for only limited, if any, involvement of early magma ocean processes in the evolution of their mantle sources. Early episodes of variable-degree partial mantle melting and melt extraction, following late accretion, would account for the observed large variations in the time-integrated Sm/Nd and Lu/Hf ratios in these early Archean mantle domains, some of which were already as melt-depleted at ~3.5 Ga as modern DMM. None of these domains were similar in composition to the projections for the modern BSE.

In contrast to the broad variations in the Nd-Hf systematics, the calculated initial γ^{187}Os values vary within a narrow range from +0.9 to −0.4 indicating that the early Archean Pilbara mantle sources evolved with near-chondritic time-integrated Re/Os. The apparent discrepancy between the depletions in highly incompatible lithophile trace elements and near-chondritic Re/Os that is observed globally and is termed the Nd-Hf-Os paradox here, is reconciled via a model whereby early low-degree (<1%) melting events fractionated Sm from Nd and Lu from Hf, but had little effect on the Re/Os ratio due to higher Re compatibility compared to Nd and Hf during mantle melting. This in turn would imply early formation and long-term isolation of a mafic crust highly enriched in incompatible lithophile trace elements.

The calculated total HSE abundances in the komatiite mantle sources range from ~30% in the Coonterunah to ~70% in the Regal system, of those in the estimates for the present-day BSE. All four Pilbara komatiite-basalt systems exhibit positive ^{182}W anomalies ranging between +11.4 and +7.7. The combined ^{182}W – source HSE abundance data for the Pilbara komatiite-basalt systems are inversely correlated and are most consistent with grainy late accretion of large differentiated planetesimals that would be expected to have created significant coupled long-lived HSE abundance and W isotope heterogeneities in the pre-late-accretion mantle.

Regression of the combined global ^{182}W – source HSE abundance data allowed us to obtain an estimate of the W isotopic composition of the pre-late accretion BSE of +17 ± 7 ppm. This estimate is similar to that of the Moon of +25 ± 5 ppm and, thus, provides further support to the notion regarding the common W isotopic composition in the Earth-Moon system and origin of the Moon mostly from the terrestrial material.

Regression analysis of the available high-precision HSE abundance data for komatiite mantle sources worldwide provide an estimate for the time of complete homogeniza-

tion of late accreted materials within the mantle at 2.5 ± 0.2 Ga, coincident with the commonly accepted timing of the onset of the modern style plate tectonics on Earth and the disappearance of positive ^{182}W anomalies in the mantle. Our calculations indicate an average survival times of late accreted planetesimals in the Earth's mantle of 1.9 ± 0.2 Ga, which place constraints on the average stirring rates of the terrestrial mantle for the HSE in the Hadean and Archean.

Declaration of Competing Interest

The authors declare that they have no known competing financial interests or personal relationships that could have appeared to influence the work reported in this paper.

ACKNOWLEDGEMENTS

This study was supported by NSF Petrology and Geochemistry Grant EAR 1754186 to ISP. M.H. thanks Carnegie Institution for Science for support for this work. We are grateful to the Geological Survey of Western Australia and Sedgwick Museum of Earth Sciences at the University of Cambridge, UK, for providing the collection of samples for this study. We would like to extend our thanks to Matthias Willbold, Guillaume Caro, and Marco Fiorentini for the thorough and constructive reviews that helped improve the original version of this manuscript, and to Andreas Stracke for comments and efficient editorial handling.

APPENDIX A. SUPPLEMENTARY MATERIAL

Supplementary data to this article can be found online at https://doi.org/10.1016/j.gca.2021.11.030.

REFERENCES

Albarède F., Blichert-Toft J., Vervoort J. D., Gleason J. D. and Rosing M. (2000) Hf-Nd isotope evidence for a transient dynamic regime in the early terrestrial mantle. *Nature* **404** (6777), 488–490.

Archer G. J., Ash R. D., Bullock E. S. and Walker R. J. (2014) Highly siderophile elements and ^{187}Re-^{187}Os isotopic systematics of the Allende meteorite: Evidence for primary nebular processes and late-stage alteration. *Geochim. Cosmochim. Acta* **131**, 402–414.

Archer G. J., Mundl A., Walker R. J., Worsham E. A. and Bermingham K. R. (2017) High-precision analysis of $^{182}W/^{184}W$ and $^{183}W/^{184}W$ by negative thermal ionization mass spectrometry: Per-integration oxide corrections using measured $^{18}O/^{16}O$. *Int. J. Mass Spectrom.* **414**, 80–86.

Archer G. J., Brennecka G. A., Gleißner P., Stracke A., Becker H. and Kleine T. (2019) Lack of late-accreted material as the origin of ^{182}W excesses in the Archean mantle: Evidence from the Pilbara Craton, Western Australia. *Earth Planet. Sci. Lett.* **528** 115841.

Arevalo R. and McDonough W. F. (2008) Tungsten geochemistry and implications for understanding the Earth's interior. *Earth Planet. Sci. Lett.* **272**(3–4), 656–665.

Armstrong R. L. (1981) Radiogenic isotopes: the case for crustal recycling on a near-steady-state no-continental-growth. *Philos. Trans. R. Soc. Lond.* **A301**, 443–472.

Arndt N. T. (1986) Differentiation of komatiite flows. *J. Petrol.* **27** (2), 279–301.

Arndt N. T. (1994) Archean Komatiites. In *Archean Crustal Evolution* (ed. K. C. Condie). Elsevier, Amsterdam, pp. 11–44.

Arndt N. T., Bruzak G. and Reischmann T. (2001) The oldest continental and oceanic plateaus: Geochemistry of basalts and komatiites of the Pilbara Craton, Australia. *Geol. Soc. Am. Spec. Pap.* **352**, 359–387.

Arndt N. T. and Jenner G. A. (1986) Crustally contaminated komatiites and basalts from Kambalda, Western Australia. *Chem. Geol.* **56**(3–4), 229–255.

Arndt N. T. and Nisbet E. G. (1982) What is a komatiite? In *Komatiites* (eds. N. T. Arndt and E. G. Nisbet). George Allen and Unwin, London, pp. 19–28.

Barley M. E. and Bickle M. J. (1982). In *Komatiites in the Pilbara Block, Western Australia*. Komatiites, George Allen and Unwin, London, pp. 105–116.

Barnes S. J. and Fiorentini M. L. (2008) Iridium, ruthenium and rhodium in komatiites: Evidence for iridium alloy saturation. *Chem. Geol.* **257**(1–2), 44–58.

Barnes S.-J., Naldrett A. J. and Gorton M. P. (1985) The origin of the fractionation of platinum-group elements in terrestrial magmas. *Chem. Geol.* **53**(3–4), 303–323.

Beattie P., Ford C. and Russell D. (1991) Partition coefficients for olivine-melt and orthopyroxene-melt systems. *Contrib. Mineraol. Petrol.* **109**(2), 212–224.

Becker H., Horan M. F., Walker R. J., Gao S., Lorand J.-P. and Rudnick R. L. (2006) Highly siderophile element composition of the Earth's primitive upper mantle: Constraints from new data on peridotite massifs and xenoliths. *Geochim. Cosmochim. Acta* **70**(17), 4528–4550.

Bennett V. C., Esat T. M. and Norman M. D. (1996) Two mantle-plume components in Hawaiian picrites inferred from correlated Os-Pb isotopes. *Nature* **381**(6579), 221–224.

Birck J. L., Roy-Barman M. and Capman F. (1997) Re-Os isotopic measurements at the femtomole level in natural samples. *Geostandards Newsletter* **20**(1), 19–27.

Blichert-Toft J. and Arndt N. T. (1999) Hf isotope compositions of komatiites. *Earth Planet. Sci. Lett.* **171**(3), 439–451.

Blichert-Toft J., Arndt N. T., Wilson A. and Coetzee G. (2015) Hf and Nd isotope systematics of early Archean komatiites from surface sampling and ICDP drilling in the Barberton Greenstone Belt, South Africa. *Am. Mineral.* **100**(11–12), 2396–2411.

Blichert-Toft J., Chauvel C. and Albaréde F. (1997) Separation of Hf and Lu for high-precision isotope analysis of rock samples by magnetic sector multiple collector ICP-MS. *Contrib. Miner. Petrol.* **127**(3), 248–260.

Blichert-Toft J. and Puchtel I. S. (2010) Depleted mantle sources through time: Evidence from Lu-Hf and Sm-Nd isotope systematics of Archean komatiites. *Earth Planet. Sci. Lett.* **297**(3–4), 598–606.

Borg L. E., Gaffney A. M. and Shearer C. K. (2014) A review of lunar chronology revealing a preponderance of 4.34–4.37 Ga ages. *Meteorit. Planet. Sci.* **50**(4), 715–732.

Bottke W. F., Levison H. F., Nesvorny D. and Dones L. (2007) Can planetesimals left over from terrestrial planet formation produce the lunar Late Heavy Bombardment? *Icarus* **190**(1), 203–223.

Bottke W. F., Morbidelli A., Jedicke R., Petit J.-M., Levison H. F., Michel P. and Metcalfe T. S. (2002) Debiased Orbital and Absolute Magnitude Distribution of the Near-Earth Objects. *Icarus* **156**(2), 399–433.

Bottke W. F., Walker R. J., Day J. M. D., Nesvorny D. and Elkins-Tanton L. (2010) Stochastic Late Accretion to Earth, the Moon, and Mars. *Science* **330**(6010), 1527–1530.

Bouvier A., Vervoort J. D. and Patchett P. J. (2008) The Lu-Hf and Sm-Nd isotopic composition of CHUR: Constraints from unequilibrated chondrites and implications for the bulk composition of terrestrial planets. *Earth Planet. Sci. Lett.* **273**(1–2), 48–57.

Bowring S. A. and Housh T. (1995) The Earth's early evolution. *Science* **269**(5230), 1535–1540.

Boyet M. and Carlson R. W. (2005) ^{142}Nd evidence for early (> 4.53 Ga) global differentiation of the silicate Earth. *Science* **309** (5734), 576–581.

Boyet M., Garçon M., Arndt N. T., Carlson R. W. and Konc Z. (2021) Residual liquid from deep magma ocean crystallization in the source of komatiites from the ICDP drill core in the Barberton Greenstone Belt. *Geochim. Cosmochim. Acta* **304**, 141–159.

Brandon A. D., Humayun M., Puchtel I. S. and Zolensky M. (2005) Re-Os isotopic systematics and platinum group element composition of the Tagish Lake carbonaceous chondrite. *Geochim. Cosmochim. Acta* **69**(6), 1619–1631.

Brown M. (2007) Metamorphism, Plate Tectonics, and the Supercontinent Cycle. *Earth Sci. Front.* **14**(1), 1–18.

Brown S. M., Elkins-Tanton L. T. and Walker R. J. (2014) Effects of magma ocean crystallization and overturn on the development of ^{142}Nd and ^{182}W isotopic heterogeneities in the primordial mantle. *Earth Planet. Sci. Lett.* **408**, 319–330.

Brown M. and Johnson T. (2018) Secular change in metamorphism and the onset of global plate tectonics. *Am. Mineral.* **103**(2), 181–196.

Buick R., Brauhart C. W., Morant P., Thornett J. R., Maniw J. G., Archibald N. J., Doepel M. G., Fletcher I. R., Pickard A. L., Smith J. B., Barley M. E., McNaughton N. J. and Groves D. I. (2002) Geochronology and stratigraphic relationships of the Sulphur Springs Group and Strelley Granite: a temporally distinct igneous province in the Archaean Pilbara Craton, Australia. *Precambr. Res.* **114**, 87–120.

Campbell I. H. (2003) Constraints on continental growth models from Nb/U ratios in the 3.5 Ga Barberton and other Archaean basalt-komatiite suites. *Am. J. Sci.* **303**(4), 319–351.

Carlson R. W., Boyet M., O'Neil J., Rizo H. and Walker R. J. (2015) Early Differentiation and Its Long-Term Consequences for Earth Evolution. In *The Early Earth*. John Wiley & Sons Inc, Hoboken, New Jersey, pp. 143–172.

Carlson R. W., Garçon M., O'Neil J., Reimink J. and Rizo H. (2019) The nature of Earth's first crust. *Chem. Geol.* **530** 119321.

Caro G. (2011) Early Silicate Earth Differentiation. *Annu. Rev. Earth Planet. Sci.* **39**(1), 31–58.

Caro G., Bourdon B., Wood B. J. and Corgne A. (2005) Trace-element fractionation in Hadean mantle generated by melt segregation from a magma ocean. *Nature* **436**(7048), 246–249.

Cattell A., Krough T. E. and Arndt N. T. (1984) Conflicting Sm-Nd whole rock and U-Pb zircon ages for Archean lavas from Newton Township, Abitibi belt, Ontario. *Earth Planet. Sci. Lett.* **70**(2), 280–290.

Chase C. G. and Patchett P. J. (1988) Stored mafic/ultramafic crust and early Archaean mantle differentiation. *Earth Planet. Sci. Lett.* **91**(1–2), 66–72.

Chauvel C., Dupre B. and Jenner G. A. (1985) The Sm-Nd age of Kambalda volcanics is 500 Ma too old! *Earth Planet. Sci. Lett.* **74**(4), 315–324.

Chou C.-L. (1978) Fractionation of siderophile elements in the earth's upper mantle. In *Proceedings of the 9th Lunar and Planetary Science Conference*, pp. 219–230.

Chou C.-L., Shaw D. M. and Crocket J. H. (1983) Siderophile trace elements in the Earth's oceanic crust and upper mantle. *J. Geophys. Res.* **88**(S2), A507–A518.

Claoue-Long J. C., Thirlwall M. F. and Nesbitt R. W. (1984) Revised Sm-Nd systematics of Kambalda greenstones, Western Australia. *Nature* **307**(5953), 697–701.

Cohen A. S. and Waters F. G. (1996) Separation of osmium from geological materials by solvent extraction for analysis by thermal ionisation mass spectrometry. *Anal. Chim. Acta* **332** (2–3), 269–275.

Compston W., Williams I. S., Campbell I. H. and Gresham J. J. (1986) Zircon xenocrysts from the Kambalda volcanics: age constraints and direct evidence for older continental crust below the Kambalda-Norseman greenstones. *Earth Planet. Sci. Lett.* **76**(3–4), 299–311.

Creaser R. A., Papanastassiou D. A. and Wasserburg G. J. (1991) Negative Thermal Ion Mass-Spectrometry of Osmium, Rhenium, and Iridium. *Geochim. Cosmochim. Acta* **55**(1), 397–401.

Dahl T. W. and Stevenson D. J. (2010) Turbulent mixing of metal and silicate during planet accretion – And interpretation of the Hf-W chronometer. *Earth Planet. Sci. Lett.* **295**(1–2), 177–186.

Dale C. W., Gannoun A., Burton K. W., Argles T. W. and Parkinson I. J. (2007) Rhenium-osmium isotope and elemental behaviour during subduction of oceanic crust and the implications for mantle recycling. *Earth Planet. Sci. Lett.* **253**(1–2), 211–225.

Dale C. W., Kruijer T. S. and Burton K. W. (2017) Highly siderophile element and ^{182}W evidence for a partial late veneer in the source of 3.8 Ga rocks from Isua, Greenland. *Earth Planet. Sci. Lett.* **458**, 394–404.

Dauphas N., Burkhardt C., Warren P. H. and Fang-Zhen T. (2014) Geochemical arguments for an Earth-like Moon-forming impactor. *Philos. Trans. R. Soc. A: Math. Phys. Eng. Sci.* **372** (2024), 20130244.

Day J. M. D., Pearson D. G. and Taylor L. A. (2007) Highly siderophile element constraints on accretion and differentiation of the Earth-Moon system. *Science* **315**(5809), 217–219.

Day J. M. D., Walker R. J., James O. B. and Puchtel I. S. (2010) Osmium isotope and highly siderophile element systematics of the lunar crust. *Earth Planet. Sci. Lett.* **289**(3–4), 595–605.

Day J. M. D. and Walker R. J. (2015) Highly siderophile element depletion in the Moon. *Earth Planet. Sci. Lett.* **423**, 114–124.

Debaille V., O'Neill C., Brandon A. D., Haenecour P., Yin Q.-Z., Mattielli N. and Treiman A. H. (2013) Stagnant-lid tectonics in early Earth revealed by ^{142}Nd variations in late Archean rocks. *Earth Planet. Sci. Lett.* **373**, 83–92.

DePaolo D. J. (1980) Crustal growth and mantle evolution: inferences from models of element transport and Nd and Sr isotopes. *Geochim. Cosmochim. Acta* **44**(8), 1185–1196.

Drake M. J. (2000) Accretion and primary differentiation of the Earth: A personal journey. *Geochim. Cosmochim. Acta* **64**(14), 2363–2370.

Fiorentini M. L., Barnes S. J., Maier W. D., Burnham O. M. and Heggie G. (2011) Global Variability in the Platinum-group Element Contents of Komatiites. *J. Petrol.* **52**(1), 83–112.

Fischer-Gödde M., Becker H. and Wombacher F. (2010) Rhodium, gold and other highly siderophile element abundances in chondritic meteorites. *Geochim. Cosmochim. Acta* **74**(1), 356–379.

Fischer-Gödde M., Becker H. and Wombacher F. (2011) Rhodium, gold and other highly siderophile elements in orogenic peridotites and peridotite xenoliths. *Chem. Geol.* **280**(3–4), 365–383.

Frost D. J., Mann U., Asahara Y. and Rubie D. C. (2008) The redox state of the mantle during and just after core formation. *Philos. Trans. R. Soc.* **366**(1883), 4315–4337.

Galer S. J. G. and Goldstein S. L. (1991) Early mantle differentiation and its thermal consequences. *Geochim. Cosmochim. Acta* **55**(1–2), 227–239.

Galer S. J. G., Goldstein S. L. and O'Nions R. K. (1989) Limits on chemical and convective isolation in the Earth's interior. *Chem. Geol.* **75**(4), 257–290.

Gangopadhyay A. and Walker R. J. (2003) Re-Os systematics of the ca. 2.7 Ga komatiites from Alexo, Ontario, Canada. *Chem. Geol.* **196**(1-4), 147–162.

Gangopadhyay A., Walker R. J., Hanski E. and Solheid P. (2006) Origin of Paleoproterozoic Komatiites at Jeesiörova, Kittilä Greenstone Complex, Finnish Lapland. *J. Petrol.* **47**(4), 773–789.

Gannoun A., Burton K. W., Day J. M. D., Harvey J., Schiano P. and Parkinson I. J. (2016) Highly Siderophile Element and Os Isotope Systematics of Volcanic Rocks at Divergent and Convergent Plate Boundaries and in Intraplate Settings. *Rev. Mineral. Geochem.* **81**, 651–724.

Goldstein S. L. and Galer S. J. G. (1992) On the trail of early mantle differentiation: $^{142}Nd/^{144}Nd$ ratios of early Archean rocks. *Eos* **73**(30), 323.

Green T. H. (1994) Experimental studies of trace-element partitioning applicable to igneous petrogenesis – Sedona 16 years later. *Chem. Geol.* **117**(1–4), 1–36.

Green M. G., Sylvester P. J. and Buick R. (2000) Growth and recycling of early Archaean continental crust: geochemical evidence from the Coonterunah and Warrawoona Groups, Pilbara Craton, Australia. *Tectonophysics* **322**(1–2), 69–88.

Hanski E., Huhma H., Rastas P. and Kamenetsky V. S. (2001) The Paleoproterozoic komatiite-picrite association of Finnish Lapland. *J. Petrol.* **42**(5), 855–876.

Huppert H. E., Sparks R. S. J., Turner J. S. and Arndt N. T. (1984) Emplacement and cooling of komatiite lavas. *Nature* **309**(5963), 19–22.

Huppert H. E. and Sparks R. S. J. (1985) Cooling and contamination of mafic and ultramafic magmas during ascent through continental crust. *Earth Planet. Sci. Lett.* **74**(4), 371–386.

Hart S. R. and Brooks S. (1977) The geochemistry and evolution of Early Precambrian mantle. *Contrib. Miner. Petrol.* **61**(2), 109–128.

Hart S. R. and Zindler A. (1986) In search of a bulk-earth composition. *Chem. Geol.* **57**(3–4), 247–267.

Hasenstab E., Tusch J., Schnabel C., Marien C. S., Van Kranendonk M. J., Smithies H., Howard H., Maier W. D. and Münker C. (2021) Evolution of the early to late Archean mantle from Hf-Nd-Ce isotope systematics in basalts and komatiites from the Pilbara Craton. *Earth Planet. Sci. Lett.* **553** 116627.

Herzberg C. T., Feigenson M., Scuba C. and Ohtani E. (1988) Majorite fractionation recorded in the geochemistry of peridotites from South Africa. *Nature* **332**(6166), 823–826.

Herzberg C., Condie K. and Korenaga J. (2010) Thermal history of the Earth and its petrological expression. *Earth Planet. Sci. Lett.* **292**(1–2), 79–88.

Herzberg C. and Gazel E. (2009) Petrological evidence for secular cooling in mantle plumes. *Nature* **458**(7238), 619–622.

Hickman A. and Van Kranendonk M. V. (2012) Early Earth Evolution: Evidence from the 3.5-1.8 Ga Geological History of the Pilbara Region of Western Australia. *Episodes* **35**(1), 283–297.

Hoffmann J. E., Münker C., Polat A., Rosing M. T. and Schulz T. (2011) The origin of decoupled Hf-Nd isotope compositions in Eoarchean rocks from southern West Greenland. *Geochim. Cosmochim. Acta* **75**(21), 6610–6628.

Hoffmann J. E. and Wilson A. H. (2017) The origin of highly radiogenic Hf isotope compositions in 3.33 Ga Commondale komatiite lavas (South Africa). *Chem. Geol.* **455**, 6–21.

Hofmann A. W. (1984) Geochemical mantle models. *Terra Cognita* **4**, 157–165.

Hofmann A. W. (1988) Chemical differentiation of the Earth: The relationship between mantle, continental crust and oceanic crust. *Earth Planet. Sci. Lett.* **90**(3), 297–314.

Hofmann A. W. and White W. M. (1982) Mantle plumes from ancient oceanic crust. *Earth Planet. Sci. Lett.* **57**(2), 421–436.

Horan M. F., Walker R. J., Morgan J. W., Grossman J. N. and Rubin A. E. (2003) Highly siderophile elements in chondrites. *Chem. Geol.* **196**(1–4), 5–20.

Horan M. F., Carlson R. W., Walker R. J., Jackson M., Garçon M. and Norman M. (2018) Tracking Hadean processes in modern basalts with 142-Neodymium. *Earth Planet. Sci. Lett.* **484**, 184–191.

Hyung E. and Jacobsen S. B. (2020) The $^{142}Nd/^{144}Nd$ variations in mantle-derived rocks provide constraints on the stirring rate of the mantle from the Hadean to the present. *Proc. Natl. Acad. Sci.* **117**(26), 14738–14744.

Jackson M. G. and Carlson R. W. (2012) Homogeneous superchondritic $^{142}Nd/^{144}Nd$ in the mid-ocean ridge basalt and ocean island basalt mantle. *Geochem. Geophys. Geosyst.* **13**(6), Q06011.

Jacobsen S. B. (1988) Isotopic and chemical constraints on mantle-crust evolution. *Geochim. Cosmochim. Acta* **52**(6), 1341–1350.

Jacobsen S. B. and Wasserburg G. J. (1980) Sm-Nd isotopic evolution of chondrites. *Earth Planet. Sci. Lett.* **50**(1), 139–155.

Jacobsen S. B. and Harper C. L. (1996) Accretion and Early Differentiation History of the Earth Based on Extinct Radionuclides. In *Earth Processes: Reading the Isotopic Code*, pp. 47–74.

Jacobsen S. B. and Yu G. (2015) Extinct isotope heterogeneities in the mantles of Earth and Mars: Implications for mantle stirring rates. *Meteorit. Planet. Sci.* **50**(4), 555–567.

Jones R. E., van Keken P. E., Hauri E. H., Tucker J. M., Vervoort J. and Ballentine C. J. (2019) Origins of the terrestrial Hf-Nd mantle array: Evidence from a combined geodynamical-geochemical approach. *Earth Planet. Sci. Lett.* **518**, 26–39.

Jochum K. P., Arndt N. T. and Hofmann A. W. (1991) Nb-Th-La in komatiites and basalts: constraints on komatiite petrogenesis and mantle evolution. *Earth Planet. Sci. Lett.* **107**(2), 272–289.

Kimura K., Lewis R. S. and Anders S. (1974) Distribution of gold and rhenium between nickel-iron and silicate melts; implications for abundance of siderophile elements on the Earth and Moon. *Geochim. Cosmochim. Acta* **38**(5), 683–701.

Kleine T., Mezger K., Münker C., Palme H. and Bischoff A. (2004a) ^{182}Hf-^{182}W isotope systematics of chondrites, eucrites, and martian meteorites: Chronology of core formation and early mantle differentiation in Vesta and Mars. *Geochim. Cosmochim. Acta* **68**(13), 2935–2946.

Kleine T., Mezger K., Palme H. and Münker C. (2004b) The W isotope evolution of the bulk silicate Earth: constraints on the timing and mechanisms of core formation and accretion. *Earth Planet. Sci. Lett.* **228**(1–2), 109–123.

Kleine T., Münker C., Mezger K. and Palme H. (2002) Rapid accretion and early core formation on asteroids and the terrestrial planets from Hf-W chronometry. *Nature* **418**(6901), 952–955.

Kleine T. and Walker R. J. (2017) Tungsten Isotopes in Planets. *Annu. Rev. Earth Planet. Sci.* **45**(1), 389–417.

König S., Münker C., Hohl S., Paulick H., Barth A. R., Lagos M., Pfander J. and Büchl A. (2011) The Earth's tungsten budget during mantle melting and crust formation. *Geochim. Cosmochim. Acta* **75**(8), 2119–2136.

Kruijer T. S. and Kleine T. (2017) Tungsten isotopes and the origin of the Moon.. *Earth Planet. Sci. Lett.* **475**(Supplement C), 15–24.

Kruijer T. S., Kleine T., Fischer-Gödde M. and Sprung P. (2015) Lunar tungsten isotopic evidence for the late veneer. *Nature* **520**(7548), 534–537.

Kumari S., Paul D. and Stracke A. (2019) Constraints on Archean crust formation from open system models of Earth evolution. *Chem. Geol.* **530** 119307.

Lahaye Y. and Arndt N. T. (1996) Alteration of a komatiite flow from Alexo, Ontario. *J. Petrol.* **37**(6), 1261–1284.

Liu J., Touboul M., Ishikawa A., Walker R. J. and Pearson D. G. (2016) Widespread tungsten isotope anomalies and W mobility in crustal and mantle rocks of the Eoarchean Saglek Block, northern Labrador, Canada: Implications for early Earth processes and W recycling. *Earth Planet. Sci. Lett.* **448**, 13–23.

Ludwig K. R. (2003) *ISOPLOT 3.00. A Geochronological Toolkit for Microsoft Excel*. Berkeley Geochronology Center Spec. Publ. No. 4, 70 pp.

Machado N., Brooks C. and Hart S. R. (1986) Determination of initial $^{87}Sr/^{86}Sr$ and $^{143}Nd/^{144}Nd$ in primary minerals from mafic and ultramafic rocks: experimental procedure and implications for the isotopic characteristics of the Archaean mantle under the Abitibi greenstone belt, Canada. *Geochim. Cosmochim. Acta* **50**(10), 2335–2348.

Maier W. D., Barnes S. J., Campbell I. H., Fiorentini M. L., Peltonen P., Barnes S. J. and Smithies R. H. (2009) Progressive mixing of meteoritic veneer into the early Earth's deep mantle. *Nature* **460**(7255), 620–623.

Mallmann G., O'Neill H. S. and C. (2007) The effect of oxygen fugacity on the partitioning of Re between crystals and silicate melt during mantle melting. *Geochim. Cosmochim. Acta* **71**(11), 2837–2857.

Marchi S., Canup R. M. and Walker R. J. (2018) Heterogeneous delivery of silicate and metal to the Earth by large planetesimals. *Nat. Geosci.* **11**, 77–81.

Marchi S., Walker R. J. and Canup R. M. (2020) A compositionally heterogeneous martian mantle due to late accretion. *Sci. Adv.* **6**(7), eaay2338.

McDonough W. F. and Sun S. S. (1995) The composition of the Earth. *Chem. Geol.* **120**(3–4), 223–253.

McKenzie D. and Bickle M. J. (1988) The volume and composition of melt generated by extension of the lithosphere. *J. Petrol.* **29** (3), 625–679.

Meisel T., Moser J. and Wegscheider W. (2001a) Recognizing heterogenous distribution of platinum group elements (PGE) in geological materials by means of the Re-Os isotope system. *Fresenius J. Anal. Chem.* **370**(5), 566–572.

Meisel T., Walker R. J., Irving A. J. and Lorand J.-P. (2001b) Osmium isotopic compositions of mantle xenoliths: A global perspective. *Geochim. Cosmochim. Acta* **65**(8), 1311–1323.

Mertzman S. A. (2000) K-Ar results from the southern Oregon - northern California Cascade range. *Oregon Geol.* **62**(4), 99–122.

Mundl-Petermeier A., Walker R. J., Fischer R. A., Lekic V., Jackson M. G. and Kurz M. D. (2020) Anomalous $\mu^{182}W$ signatures in high $^{3}He/^{4}He$ ocean island basalts – fingerprints of Earth's core? *Geochim. Cosmochim. Acta* **271**, 194–211.

Murphy D., Rizo H., O'Neil J., Hepple R., Wiemer D., Kemp A. and Vervoort J. (2021) Combined Sm-Nd, Lu-Hf, and ^{142}Nd study of Paleoarchean basalts from the East Pilbara Terrane, Western Australia. *Chem. Geol.* **578** 120301.

Nagai Y. and Yokoyama T. (2014) Chemical Separation of Mo and W from Terrestrial and Extraterrestrial Samples via Anion Exchange Chromatography. *Anal. Chem.* **86**(10), 4856–4863.

Nebel O., Campbell I. H., Sossi P. A. and Van Kranendonk M. J. (2014) Hafnium and iron isotopes in early Archean komatiites record a plume-driven convection cycle in the Hadean Earth. *Earth Planet. Sci. Lett.* **397**, 111–120.

Nesbitt R. W., Sun S. S. and Purvis A. C. (1979) Komatiites: geochemistry and genesis. *Can. Mineral.* **17**(2), 165–186.

Newsom H. E., Sims K. W. W., Noll P. D., Jaeger W. L., Maehr S. A. and Beserra T. B. (1996) The depletion of tungsten in the bulk silicate Earth: Constraints on core formation. *Earth Planet. Sci. Lett.* **60**(5), 1155–1169.

Nicklas R. W., Puchtel I. S. and Ash R. D. (2016) High-precision determination of the oxidation state of komatiite lavas using vanadium liquid-mineral partitioning. *Chem. Geol.* **433**, 36–45.

Nicklas R. W., Puchtel I. S. and Ash R. D. (2018) The Redox Evolution of the Archean Mantle: Evidence from Komatiites. *Geochim. Cosmochim. Acta* **222**, 447–466.

Nielsen S. G., Shimizu N., Lee C. T. A. and Behn M. D. (2014) Chalcophile behavior of thallium during MORB melting and implications for the sulfur content of the mantle. *Geochem. Geophys. Geosyst.* **15**(12), 4905–4919.

Nisbet E. G. and Chinner G. A. (1981) Controls of the eruption of mafic and ultramafic lavas, Ruth Well nickel-copper prospect. *West Pilbara. Economic Geology* **76**(6), 1729–1735.

Nisbet E. G., Cheadle M. J., Arndt N. T. and Bickle M. J. (1993) Constraining the potential temperature of the Archaean mantle: a review of the evidence from komatiites. *Lithos* **30**, 291–307.

O'Neil J., Carlson R. W., Francis D. and Stevenson R. K. (2008) Neodymium-142 evidence for Hadean mafic crust. *Science* **321** (5897), 1828–1831.

O'Neil J., Rizo H., Boyet M., Carlson R. W. and Rosing M. T. (2016) Geochemistry and Nd isotopic characteristics of Earth's Hadean mantle and primitive crust. *Earth Planet. Sci. Lett.* **442**, 194–205.

Patchett P. J., Kauvo O., Hedge C. E. and Tatsumoto M. (1981) Evolution of continental crust and mantle heterogeneity: evidence from Hf isotopes. *Contrib. Miner. Petrol.* **78**(3), 279–297.

Patchett P. J., White W. M., Feldmann H., Kielinczuk S. and Hofmann A. W. (1984) Hafnium/rare earth element fractionation in the sedimentary system and crustal recycling into the Earth's mantle. *Earth Planet. Sci. Lett.* **69**(2), 365–378.

Puchtel I. S., Haase K. M., Hofmann A. W., Chauvel C., Kulikov V. S., Garbe-Schönberg C.-D. and Nemchin A. A. (1997) Petrology and geochemistry of crustally contaminated komatiitic basalts from the Vetreny Belt, southeastern Baltic Shield: Evidence for an early Proterozoic mantle plume beneath rifted Archean continental lithosphere. *Geochim. Cosmochim. Acta* **61** (6), 1205–1222.

Puchtel I. S., Hofmann A. W., Mezger K., Jochum K. P., Shchipansky A. A. and Samsonov A. V. (1998) Oceanic plateau model for continental crustal growth in the Archaean: A case study from the Kostomuksha greenstone belt, NW Baltic Shield. *Earth Planet. Sci. Lett.* **155**(1–2), 57–74.

Puchtel I. S., Hofmann A. W., Amelin Y. V., Garbe-Schönberg C.-D., Samsonov A. V. and Shchipansky A. A. (1999) Combined mantle plume - island arc model for the formation of the 2.9 Ga Sumozero-Kenozero greenstone belt, SE Baltic Shield: Isotope and trace element constraints. *Geochim. Cosmochim. Acta* **63** (21), 3579–3595.

Puchtel I. S., Brandon A. D. and Humayun M. (2004a) Precise Pt-Re-Os isotope systematics of the mantle from 2.7-Ga komatiites. *Earth Planet. Sci. Lett.* **224**(1–2), 157–174.

Puchtel I. S., Humayun M., Campbell A., Sproule R. and Lesher C. M. (2004b) Platinum group element geochemistry of komatiites from the Alexo and Pyke Hill areas, Ontario, Canada. *Geochim. Cosmochim. Acta* **68**(6), 1361–1383.

Puchtel I. S. and Humayun M. (2005) Highly siderophile element geochemistry of ^{187}Os-enriched 2.8-Ga Kostomuksha komatiites, Baltic Shield. *Geochim. Cosmochim. Acta* **69**(6), 1607–1618.

Puchtel I. S., Brandon A. D., Humayun M. and Walker R. J. (2005) Evidence for the early differentiation of the core from Pt-Re-Os isotope systematics of 2.8-Ga komatiites. *Earth Planet. Sci. Lett.* **237**(1–2), 118–134.

Puchtel I. S., Humayun M. and Walker R. J. (2007) Os-Pb-Nd isotope and highly siderophile and lithophile trace element systematics of komatiitic rocks from the Volotsk suite, SE Baltic Shield. *Precambrian Res.* **158**(1–2), 119–137.

Puchtel I. S., Walker R. J., Anhaeusser C. R. and Gruau G. (2009a) Re-Os isotope systematics and HSE abundances of the 3.5 Ga Schapenburg komatiites, South Africa: Hydrous melting or prolonged survival of primordial heterogeneities in the mantle? *Chem. Geol.* **262**(3–4), 355–369.

Puchtel I. S., Walker R. J., Brandon A. D. and Nisbet E. G. (2009b) Pt-Re-Os and Sm-Nd isotope and HSE and REE systematics of the 2.7 Ga Belingwe and Abitibi komatiites. *Geochim. Cosmochim. Acta* **73**(20), 6367–6389.

Puchtel I. S., Blichert-Toft J., Touboul M., Walker R. J., Byerly G., Nisbet E. G. and Anhaeusser C. R. (2013) Insights into early Earth from Barberton komatiites: Evidence from lithophile isotope and trace element systematics. *Geochim. Cosmochim. Acta* **108**, 63–90.

Puchtel I. S., Walker R. J., Touboul M., Nisbet E. G. and Byerly G. R. (2014) Insights into Early Earth from the Pt-Re-Os isotope and Highly Siderophile Element abundance systematics of Barberton komatiites. *Geochim. Cosmochim. Acta* **125**, 394–413.

Puchtel I. S., Blichert-Toft J., Touboul M., Horan M. F. and Walker R. J. (2016a) The coupled ^{182}W–^{142}Nd record of early terrestrial mantle differentiation. *Geochem. Geophys. Geosyst.* **17**(6), 2168–2193.

Puchtel I. S., Touboul M., Blichert-Toft J., Walker R. J., Brandon A. D., Nicklas R. W., Kulikov V. S. and Samsonov A. V. (2016b) Lithophile and siderophile element systematics of the mantle at the Archean-Proterozoic boundary: Evidence from 2.4 Ga komatiites. *Geochim. Cosmochim. Acta* **180**, 227–255.

Puchtel I. S., Blichert-Toft J., Touboul M. and Walker R. J. (2018) ^{182}W and HSE constraints from 2.7 Ga komatiites on the heterogeneous nature of the Archean mantle. *Geochim. Cosmochim. Acta* **228**, 1–26.

Puchtel I. S., Mundl-Petermeier A., Horan M., Hanski E. J., Blichert-Toft J. and Walker R. J. (2020) Ultra-depleted 2.05 Ga komatiites of Finnish Lapland: Products of grainy late accretion or core-mantle interaction? *Chem. Geol.* **554** 119801.

Rehkämper M. and Halliday A. N. (1997) Development and application of new ion-exchange techniques for the separation of the platinum-group and other siderophile elements from geological samples. *Talanta* **44**(4), 663–672.

Reimink J. R., Mundl-Petermeier A., Carlson R. W., Shirey S. B., Walker R. J. and Pearson D. G. (2020) Tungsten isotope composition of Archean crustal reservoirs and implications for terrestrial μ^{182}W evolution. *Geochem. Geophys. Geosyst.* **21**(7), e2020GC009155.

Ringwood A. E. (1966) The chemical composition and origin of the Earth. In *Advances in Earth Sciences* (ed. P. M. Hurley). The MIT Press, Cambridge, MA, USA, pp. 287–356.

Rizo H., Boyet M., Blichert-Toft J. and Rosing M. (2011) Combined Nd and Hf isotope evidence for deep-seated source of Isua lavas. *Earth Planet. Sci. Lett.* **312**(3–4), 267–279.

Rizo H., Andrault D., Bennett N. R., Humayun M., Brandon A. D., Vlastelic I., Moine B., Poirier A., Bouhifd M. A. and Murphy D. T. (2019) ^{182}W evidence for core-mantle interaction in the source of mantle plumes. *Geochem. Perspect. Lett.* **11**, 6–11.

Rizo H., Walker R. J., Carlson R. W., Touboul M., Horan M. F., Puchtel I. S., Boyet M. and Rosing M. T. (2016) Early Earth differentiation investigated through ^{142}Nd, ^{182}W, and highly siderophile element abundances in samples from Isua, Greenland. *Geochim. Cosmochim. Acta* **175**, 319–336.

Roeder P. L. and Emslie R. F. (1970) Olivine-liquid equilibrium. *Contrib. Miner. Petrol.* **29**(4), 275–282.

Rubie D. C., Melosh H. J., Reid J. E., Liebske C. and Righter K. (2003) Mechanisms of metal-silicate equilibration in the terrestrial magma ocean. *Earth Planet. Sci. Lett.* **205**(3–4), 239–255.

Rudnick R. L., Barth M., Horn I. and McDonough W. F. (2000) Rutile-bearing refractory eclogites: missing link between continents and depleted mantle. *Science* **287**(5451), 278–281.

Rudnick R. L. and Fountain D. M. (1995) Nature and composition of the continental crust: a lower crustal perspective. *Rev. Geophys.* **33**(3), 267–309.

Rudnick R. L. and Gao S. (2003) *Composition of the Continental Crust*. Treatise on Geochemistry, Elsevier, Amsterdam, pp. 1–64.

Rudnick R. L. and Gao S. (2014) *Composition of the Continental Crust*. Treatise on Geochemistry, Elsevier, Amsterdam, pp. 1–51.

Ryder G. (2002) Mass flux in the ancient Earth-Moon system and benign implications for the origin of life on Earth. *J. Geophys. Res.* **107**(E4), 6.1-6.13.

Salters V. J. M. (1996) The generation of mid-ocean ridge basalts from the Hf and Nd isotope perspective. *Earth Planet. Sci. Lett.* **141**(1–4), 109–123.

Salters V. J. M. and White W. M. (1998) Hf isotope constraints on mantle evolution. *Chem. Geol.* **145**(3–4), 447–460.

Scherer E., Münker C. and Mezger K. (2001) Calibration of the lutetium-hafnium clock. *Science* **293**(5530), 683–687.

Schoenberg R., Kamber B. S., Collerson K. D. and Eugster O. (2002) New W-isotope evidence for rapid terrestrial accretion and very early core formation. *Geochim. Cosmochim. Acta* **66**(17), 3151–3160.

Shirey S. B. and Hanson G. N. (1986) Mantle heterogeneity and crustal recycling in Archean granite-greenstone belts: Evidence from Nd isotopes and trace elements in the Rainy Lake area, Superior Province, Ontario, Canada. *Geochim. Cosmochim. Acta* **50**(12), 2631–2651.

Shirey S. B., Kamber B. S., Whitehouse M. J., Mueller P. A. and Basu A. R. (2008) A review of the isotopic and trace element evidence for mantle and crustal processes in the Hadean and Archean: Implications for the onset of plate tectonic subduction. In *When Did Plate Tectonics Begin on Planet Earth?* (eds. K. C. Condie and V. Pease). Geological Society of America Special Paper 440, pp. 1–29.

Smithies R. H., Champion D. C., Van Kranendonk M. J. and Hickman A. H. (2007) *Geochemistry of volcanic rocks of the northern Pilbara Craton, Western Australia*. Geological Survey of Western Australia, Perth, Report 104, 47 pp.

Sobolev A. V., Asafov E. V., Gurenko A. A., Arndt N. T., Batanova V. G., Portnyagin M. V., Garbe-Schönberg D. and Krasheninnikov S. P. (2016) Komatiites reveal a hydrous Archaean deep-mantle reservoir. *Nature* **531**(7596), 628–632.

Sobolev A. V., Asafov E. V., Gurenko A. A., Arndt N. T., Batanova V. G., Portnyagin M. V., Garbe-Schönberg D., Wilson A. H. and Byerly G. R. (2019) Deep hydrous mantle reservoir provides evidence for crustal recycling before 3.3 billion years ago. *Nature* **571**(7766), 555–559.

Söderlund U., Patchett J. P., Vervoort J. D. and Isachsen C. E. (2004) The ^{176}Lu decay constant determined by Lu-Hf and U-Pb isotope systematics of Precambrian mafic intrusions. *Earth Planet. Sci. Lett.* **219**(3–4), 311–324.

Sossi P. A., Eggins S. M., Nesbitt R. W., Nebel O., Hergt J. M., Campbell I. H., O'Neill H. St. C., Van Kranendonk M. and Davies D. R. (2016) Petrogenesis and Geochemistry of Archean Komatiites. *J. Petrol.* **57**(1), 147–184.

Steenstra E. S., Berndt J., Klemme S., Rohrbach A., Bullock E. S. and van Westrenen W. (2020) An experimental assessment of

the potential of sulfide saturation of the source regions of eucrites and angrites: Implications for asteroidal models of core formation, late accretion and volatile element depletions. *Geochim. Cosmochim. Acta* **269**, 39–62.

Strom R. G., Malhotra R., Ito T., Yoshida F. and Kring D. A. (2005) The origin of planetary impactors in the inner Solar system. *Science* **309**(5742), 1847–1850.

Sun Z., Xiong X., Wang J., Liu X., Li L., Ruan M., Zhang L. and Takahashi E. (2020) Sulfur abundance and heterogeneity in the MORB mantle estimated by copper partitioning and sulfur solubility modelling. *Earth Planet. Sci. Lett.* **538** 116169.

Sylvester P. J., Campbell I. H. and Bowyer D. A. (1997) Nb/U evidence for early formation of the continental crust. *Science* **275**(5299), 521–523.

Tappe S., Budde G., Stracke A., Wilson A. and Kleine T. (2020) The tungsten-182 record of kimberlites above the African superplume: Exploring links to the core-mantle boundary. *Earth Planet. Sci. Lett.* **547** 116473.

Touboul M., Puchtel I. S. and Walker R. J. (2012) ^{182}W Evidence for Long-Term Preservation of Early Mantle Differentiation Products. *Science* **335**, 1065–1069.

Touboul M., Liu J., O'Neil J., Puchtel I. S. and Walker R. J. (2014) New Insights into the Hadean Mantle Revealed by ^{182}W and Highly Siderophile Element Abundances of Supracrustal Rocks from the Nuvvuagittuq Greenstone Belt, Quebec, Canada. *Chem. Geol.* **383**, 63–75.

Touboul M., Puchtel I. S. and Walker R. J. (2015) Tungsten isotopic evidence for disproportional late accretion to the Earth and Moon. *Nature* **520**(7548), 530–533.

Tusch J., Sprung P., van de Löcht J., Hoffmann J. E., Boyd A. J., Rosing M. T. and Münker C. (2019) Uniform ^{182}W isotope compositions in Eoarchean rocks from the Isua region, SW Greenland: The role of early silicate differentiation and missing late veneer. *Geochim. Cosmochim. Acta* **257**, 284–310.

Tusch J., Münker C., Hasenstab E., Jansen M., Marien C. S., Kurzweil F., Van Kranendonk M. J., Smithies H., Maier W. and Garbe-Schönberg D. (2021) Convective isolation of Hadean mantle reservoirs through Archean time. *Proc. Natl. Acad. Sci.* **118**(2) e2012626118.

Van Kranendonk M. J., Hickman A. H., Smithies R. H., Williams I. R., Bagas L. and Farrell T. R. (2006) *Revised lithostratigraphy of Archean supracrustal and intrusive rocks in the northern Pilbara Craton, Western Australia*. Western Australia Geological Survey, Record 2006/15, 57 pp.

Van Kranendonk M. J., Smithies R. H., Hickman A. H., Wingate M. T. D. and Bodorkos S. (2010) Evidence for Mesoarchean (~3.2 Ga) rifting of the Pilbara Craton: The missing link in an early Precambrian Wilson cycle. *Precambr. Res.* **177**(1–2), 145–161.

Vervoort J. D. and Blichert-Toft J. (1999) Evolution of the depleted mantle: Hf isotope evidence from juvenile rocks through time. *Geochim. Cosmochim. Acta* **63**(3–4), 533–566.

Vervoort J. D., Patchett P. J., Albarède F., Blichert-Toft J., Rudnick R. and Downes H. (2000) Hf-Nd isotopic evolution of the lower crust. *Earth Planet. Sci. Lett.* **181**(1–2), 115–129.

Vervoort J. D., Patchett P. J., Gehrels G. E. and Nutman A. P. (1996) Constraints on early Earth differentiation from hafnium and neodymium isotopes. *Nature* **379**(6566), 624–627.

Vervoort J. D., Patchett P. J., Blichert-Toft J. and Albarède F. (1999) Relationships between Lu-Hf and Sm-Nd isotopic systems in the global sedimentary system. *Earth Planet. Sci. Lett.* **168**(1–2), 79–99.

Vezinet A., Pearson D. G. and Thomassot E. (2021) Effects of contamination on whole-rock isochrons in ancient rocks: A numerical modelling approach. *Lithos* **386–387** 106040.

Walker R. J., Shirey S. B. and Stecher O. (1988) Comparative Re-Os, Sm-Nd and Rb-Sr isotope and trace element systematics for Archean komatiite flows from Munro Township, Abitibi belt, Ontario. *Earth Planet. Sci. Lett.* **87**(1–2), 1–12.

Walker R. J. (2009) Highly siderophile elements in the Earth, Moon and Mars: Update and implications for planetary accretion and differentiation. *Chem. Erde* **69**(2), 101–125.

Walker R. J. (2014) Siderophile element constraints on the origin of the Moon. *Philos. Trans. R. Soc. Lond.* **372**, 20130258.

Walker R. J., Horan M. F., Morgan J. W., Becker H., Grossman J. N. and Rubin A. E. (2002) Comparative ^{187}Re-^{187}Os systematics of chondrites: Implications regarding early solar system processes. *Geochim. Cosmochim. Acta* **66**(23), 4187–4201.

Walker R. J., Horan M. F., Shearer C. K. and Papike J. J. (2004) Low abundances of highly siderophile elements in the lunar mantle: Evidence for prolonged late accretion. *Earth Planet. Sci. Lett.* **224**(3–4), 399–413.

Wilde S. A., Valley J. W., Peck W. H. and Graham C. M. (2001) Evidence from detrital zircons for the existence of continental crust and oceans on the Earth 4.4 Gyr ago. *Nature* **409**(6817), 175–178.

Willbold M., Elliott T. and Moorbath S. (2011) The tungsten isotopic composition of the Earth's mantle before the terminal bombardment. *Nature* **477**(7363), 195–198.

Willbold M., Mojzsis S. J., Chen H. W. and Elliott T. (2015) Tungsten isotope composition of the Acasta Gneiss Complex. *Earth Planet. Sci. Lett.* **419**, 168–177.

Willig M. and Stracke A. (2019) Earth's chondritic light rare earth element composition: Evidence from the Ce-Nd isotope systematics of chondrites and oceanic basalts. *Earth Planet. Sci. Lett.* **509**, 55–65.

Willig M., Stracke A., Beier C. and Salters V. J. M. (2020) Constraints on mantle evolution from Ce-Nd-Hf isotope systematics. *Geochim. Cosmochim. Acta* **272**, 36–53.

Wilson A. H. and Carlson R. W. (1989) A Sm-Nd and Pb isotope study of Archaean greenstone belts in the southern Kaapvaal Craton, South Africa. *Earth Planet. Sci. Lett.* **96**(1–2), 89–105.

Yin Q., Jacobsen S. B., Yamashita K., Blichert-Toft J., Telouk P. and Albarede F. (2002) A short timescale for terrestrial planet formation from Hf-W chronometry of meteorites. *Nature* **418**(6901), 949–952.

Zindler A. and Hart S. R. (1986) Chemical Geodynamics. *Annu. Rev. Earth Planet. Sci.* **14**, 493–571.

Zindler A., Jagoutz E. and Goldstein S. L. (1982) Nd, Sr and Pb isotopic systematics in a three-component mantle: a new perspective. *Nature* **298**(5874), 519–523.

Associate editor: Andreas Stracke